

In Situ Transmission Electron Microscopy

Frances M. Ross

1 A Working Definition of *in situ* Transmission Electron Microscopy

Since the earliest days of transmission electron microscopy, microscopists have realized the potential of microscopy for studying dynamic processes. Images recorded sequentially can be used to track the changes caused by deliberate actions, such as heating or straining, or uncontrolled processes, such as beam damage. The class of experiments where a specimen is changed or acted on while it remains under observation (i.e., *in situ* in the polepiece) is referred to as *in situ* microscopy. In a sense every TEM observation is an *in situ* experiment, since every specimen is affected by the electron beam to some extent. But the *in situ* experimenter aims to modify the specimen in a deliberate way and learn something from the results.

In the best *in situ* experiments, a controlled change is made to a specimen's environment, and this is correlated with the resulting change in its structure, measured using any of the imaging, analytical, or diffraction techniques available, or its electronic or mechanical properties, which can also be measured *in situ*. Preferably both the "input," in other words the change in sample environment, and the "output," or consequent change in structure or properties, are recorded simultaneously and quantitatively. Given sufficient care with artifacts, a quantitative understanding of a fundamental physical process can be obtained.

There are numerous advantages to performing experiments *in situ*. A single *in situ* experiment gives a continuous view of a process, so may take the place of multiple post-mortem measurements. A single heating experiment, for example, can provide information that would otherwise have to be extracted by examination of many samples which had been annealed to different temperatures or for different times. Because an *in situ* experiment is continuously recorded, it is easier to catch a transient phase or observe a nucleation event. *In situ* experiments can yield specific and detailed kinetic information, measuring

for example the motion of individual dislocations under known stress, or the growth rates of individual nanocrystals. Properties can be determined for well-characterized nanostructures, such as the conductivity of single nanotubes or the melting point of precipitates. Finally, growth experiments in particular provide a window into the behavior of materials under real processing conditions, since significant changes can occur if we remove a material from the growth chamber and perform analysis post-mortem.

Although *in situ* experiments provide unique information, it is at a cost of increased experimental complexity. Careful design of the specimen is necessary to minimize thin foil effects. Tests must be carried out to understand beam effects, and calibration of the applied stimulus is critical.

Given the complexity of some *in situ* experiments, what is remarkable and inspirational is the variety of materials and properties that have been studied *in situ*. In the vast majority of experiments, the "input" to the specimen ranges from simple beam heating to controlled sample heating, cooling, or straining; application of a voltage or a magnetic field; or even modification with a scanning probe tip. A specially designed sample holder may be used which could include a heater, electrical contacts, a tip, or a mechanical straining stage. Such experiments can be carried out in most microscopes, apart from those with the tiniest polepiece gaps, although a side entry design is most convenient for experiments involving feedthroughs. A second, less common class of experiments is based on changing the sample's environment by, for example, exposing it to a reactive gas or depositing another material onto it. For such studies, two experimental strategies are possible. Firstly, one can use a conventional microscope, but achieve environmental control in a modified sample holder in which the sample and reactive environment are enclosed in a region between two electron-transparent membranes. Alternatively, the microscope itself may be modified, for example by adding gas feedthroughs to the specimen area. The sample can then be exposed to the desired environment in a standard holder. For certain experiments involving reactive surfaces, a clean environment is important and the entire microscope must then be designed for ultra high vacuum (UHV). A UHV specimen region allows clean surfaces to be prepared (for example by heating) and then modified controllably in the polepiece. True UHV systems are relatively rare as they represent a large investment. They often include side chambers attached to the microscope in which other preparation or deposition treatments can be carried out *ex situ*.

In terms of collecting the "output" data, some *in situ* experiments require atomic resolution, while others use lower resolution strain or defect imaging, diffraction analysis, and occasionally elemental mapping. Data may be collected onto videotape or hard drive or as a series of still images, and in some cases high speed image acquisition may be necessary. Commonly, other measurements, such as sample temperature, gas pressure, electrical conductivity or applied force, are collected simultaneously and may be written onto the video tape or stored electronically with the images.

The following sections will describe some of the accomplishments of *in situ* microscopy in improving our understanding of the bulk properties and surface physics of materials. *In situ* microscopy has a rich history, but here we will focus on more recent experiments, mainly within the last decade, with the hope that this emphasis will capture the ongoing excitement of this quickly developing field. Along the way we will discuss experimental requirements for *in situ* experiments and the recognition and elimination of artifacts. We hope to show how widely *in situ* microscopy has enhanced our understanding of phenomena associated with phase transformations, crystal growth, electrical and mechanical properties, magnetism and ferroelectricity, implantation and beam effects, and even processes which take place in the liquid phase. Improvements such as the larger polepiece gap made possible by aberration correction, more sophisticated data analysis techniques, and enhanced abilities to fabricate specimens of controlled geometry, promise to extend the possibilities of *in situ* techniques even further.

2 Phase Transformations

The largest body of work accomplished using *in situ* TEM techniques has been in the area of phase transformations: melting, crystallization, transformations between crystal structures, and the formation of new phases by solid state diffusion. An understanding of such transformations is scientifically interesting and technologically essential in, for example, the processing of alloys or the development of new materials having extreme hardness or superplastic, magnetic or shape memory properties. *In situ* TEM has provided detailed information on the mechanism, kinetics, and structures produced during many phase transformations, both in the bulk and in nanoscale volumes. Microscopy is well suited for such studies because its high resolution allows atomic motions to be visualized, and diffraction can identify the phases present under changing conditions. Small precipitates or nuclei can be characterized and their evolution followed, and complex or incommensurate structures can be analyzed.

The requirements for these studies are usually simple, consisting of time-resolved imaging and a heating stage, although some experiments involve cooling, straining, or deposition. Images are commonly recorded at video rate (30 images per second) and the temperature can often be chosen to give a convenient reaction velocity. Heat is applied using the electron beam, or, more controllably, by heating a furnace or a resistive wire close to the sample. Alternatively, a heating current may be passed through the sample or the sample may be stuck onto a resistively heated wire. For qualitative results, such as determining reaction mechanisms, structural changes are observed during heating and cooling. For quantitative measurements the sample temperature must be measured accurately. This is a challenge since the temperature measured at the furnace by a thermocouple, say, may not be the same as the temperature at the region under observation. However, with some effort, careful calibrations have been achieved.

We first discuss transformations in bulk materials, then examine transformations in small volumes of material. These small volumes may be free-standing nanostructures or nanoparticles encapsulated in a matrix. A recurring theme will be the finding that small volumes do not transform under the same conditions as larger volumes, which is extremely important for the development of complex materials.

2.1 Crystallization, Melting and Grain Growth in Bulk Materials

2.1.1 Amorphization and Crystallization

The crystallization of amorphous materials is an interesting and important process which is uniquely suited to TEM analysis. Early, elegantly simple experiments involved the recrystallization of silicon, deposited as an amorphous thin film and then heated in cross section in a high resolution TEM. These experiments (Parker et al., 1986; Sinclair et al., 1987) showed the power of high resolution imaging at high temperature. The nucleation of crystallites was visualized, allowing estimation of the critical nucleus size, and the irregular progress of the reaction front was demonstrated, even though macroscopically the kinetics were consistent with a more continuous ledge mechanism. This pioneering work provided an atomic scale view of a bulk phase transformation, showing the start-stop motion we now expect for atomic scale processes. Using multilayer specimens to extend this approach to metal-mediated crystallization of Si, Ge, or C clearly demonstrated the mechanism for these reactions as well (Figure 6–1, Konno and Sinclair, 1992, 1995a, b, c; Sinclair et al., 2002). Si crystallization has now been so well studied, both *in situ* and *ex situ*, that it has actually been used as a calibration tool to measure the temperature in thin specimens (Hull and Bean, 1994; Stach et al., 1998a). An accurately calibrated temperature is essential in obtaining quantitative information, such as activation energy, for reactions carried out *in situ*. More recent crystallization studies have used plan view rather than cross sectional geometry, allowing many individual grains to be imaged. For example, the nucleation and growth rates of individual NiTi crystals during heating were found to be in agreement with the Johnson-Mehl-Avrami-Kolmogorov model (Lee et al., 2005), allowing grain size distributions to be predicted in this shape-memory alloy.

An interesting industrial application of this type of experiment, relevant to new types of information storage, is shown in Figure 6–2. Phase change materials such as GeSb and GeSbTe can store bits of information as amorphous areas embedded in crystalline regions. A high laser power is used to write amorphous spots, a medium power erases by recrystallizing, and a low power (or other measurement) reads the bits. *In situ* observations of crystallization have been made in films deposited on SiN membranes (Kooi et al., 2004; Kooi and De Hosson, 2004), free-standing films (Petford-Long et al., 1995) and actual compact disc materials (Kaiser et al., 2004). Beam heating shows nucleation and growth kinetics (Figure 6–2B), while more controlled experiments using a heating stage measure activation energies (Figure 6–2A). SbO_x, another potential phase change material, has been examined *in*

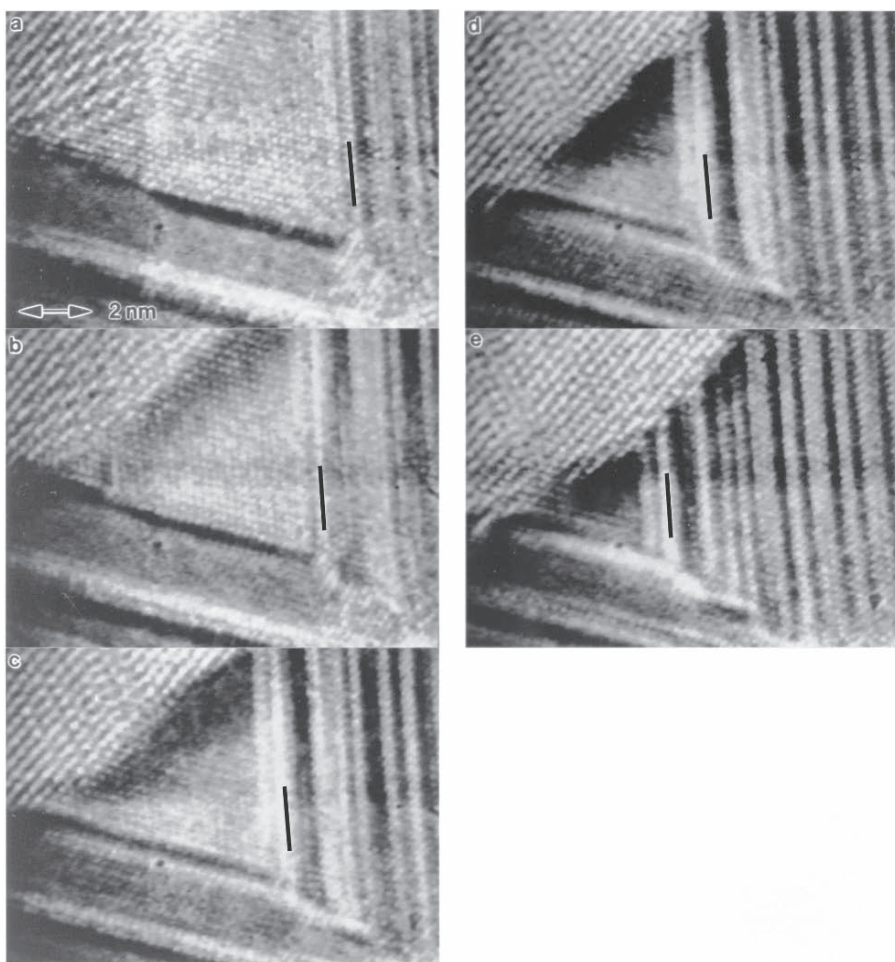


Figure 6-1. Metal-induced crystallization. *In situ* high-resolution images recorded during the Ag-mediated crystallization of Ge at 250°C. The time between frames is 8 s. The Ag is the faulted region in the center and the crystalline Ge is in the upper left. The Ag crystal appears to migrate toward the amorphous Ge region but the faults remain fixed (one fault is indicated by a line). The inference is that Ge is supplied by diffusion through the Ag lattice, and the net motion of the Ag is caused by counterdiffusion of Ag atoms. The lack of any amorphous entectic is dearly demonstrated. (From Konno and Sinclair, 1995a, with kind permission of Taylor and Francis Ltd.)

situ for different stoichiometries x , again determining activation energy (Missana et al., 1999). Although stress effects may change the kinetics in electron transparent foils, these experiments are useful in allowing transformation parameters to be measured and structural changes examined.

The reverse process of solid state amorphization is hard to measure using other experimental techniques. *In situ* heating of systems such as Ti-Si, Zr-Si, Pt-GaAs (Sinclair, 1994), and Al-Pt (Blanpain et al., 1990) allow nucleation locations to be determined and diffusion processes to be characterized. Amorphization can also be induced by the electron beam, as will be discussed in Section 8.

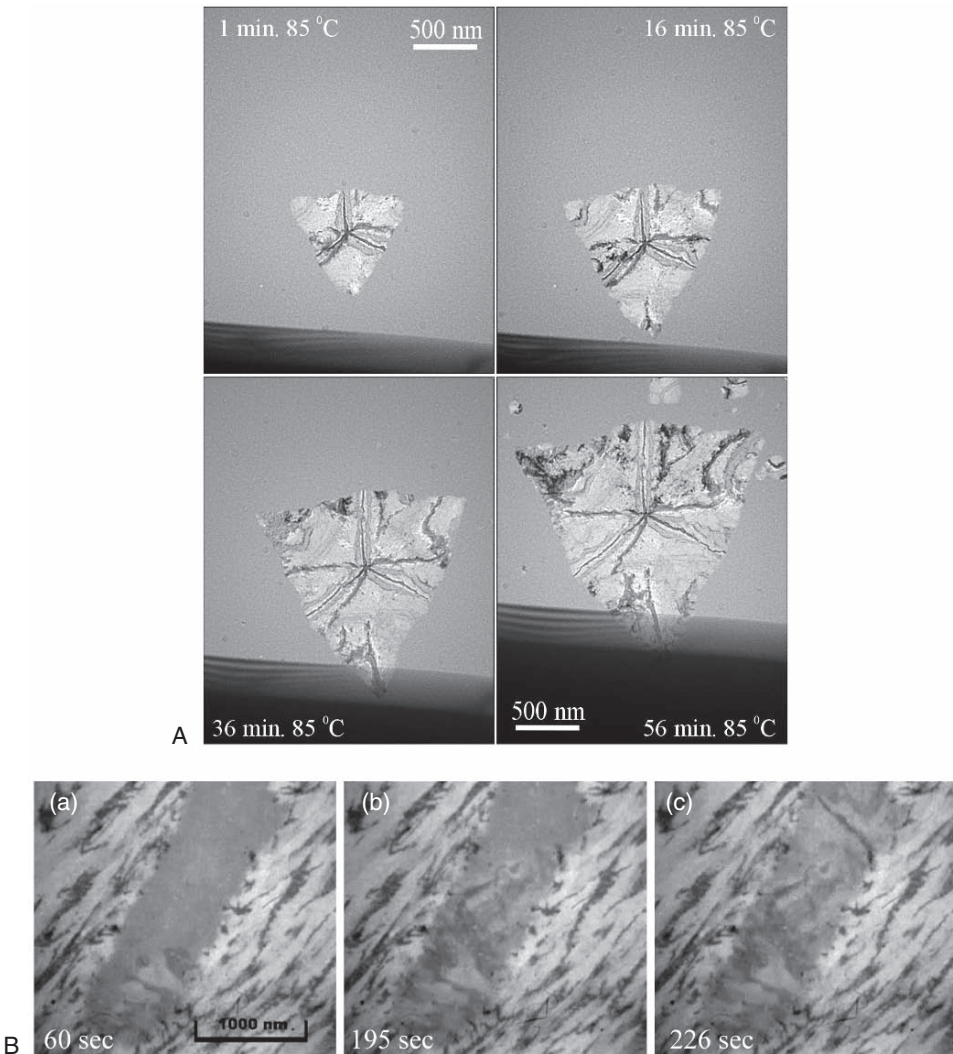


Figure 6–2. The amorphous to crystalline transformation in phase change materials. (A) Bright-field images recorded during crystallization of a 40-nm $\text{Sb}_{3.6}\text{Te}$ film at 85°C. The film was deposited on an SiN membrane. Note that the growing crystal was prenucleated by heating for 5 min at 95°C. (Reprinted with permission from Kooi and de Hosson, © 2004. American Institute of Physics) (B) Bright-field images displaying stepwise electron irradiation-induced crystallization of an amorphous data mark in 14-nm-thick $\text{Ga}_{15}\text{Sb}_{85}$ after irradiation for the times indicated at a current density of 1.5nA mm^{-2} . The specimen was made from a conventional CD-RW/DVD1RW disk consisting of a $\text{ZnS:SiO}_2/\text{GaSb}/\text{ZnS:SiO}_2/\text{SiN}/\text{Ag}/\text{SiN}$ layered stack on a polycarbonate substrate, with all layers removed except for the GaSb and surrounding dielectric layers. The phase-change layer was crystallized using a broad laser beam then amorphous data marks were “written” using a home-built recorder. (Reprinted with permission from Kaiser et al., © 2004. American Institute of Physics)

2.1.2 The Solid-to-Liquid Transformation and the Structure of the Solid-Liquid Interface

Melting and freezing can be observed *in situ* by diffraction or imaging. Perhaps the ultimate example is the “nanothermometer” shown in Figure 6–3, fabricated by enclosing Ga in a large diameter carbon

nanotube (Gao and Bando, 2002; Z. Liu et al., 2004). This structure was used to measure the expansion coefficient of liquid Ga and observe different structures on freezing. Several other transformations involving liquids have also been studied *in situ*. It may at first appear surprising that liquids can be examined at all. However, liquids with low vapor pressure, such as Ga, In, Si, or Al, may be treated in the same way as solids, provided they do not move around too much, while liquids with high vapor pressure can be observed if they are naturally encapsulated, for example as inclusions, or are cooled. High vapor pressure liquids which are not in the form of inclusions require special techniques which will be described in Section 7. Liquids which are not encapsulated and are too mobile may be studied by coating the thin foil with a polymer to maintain shape (Kato et al., 2000; Senda et al., 2004). Such studies show that melting points in thin films differ from bulk (Senda et al., 2004).

TEM studies have provided information about the structure of the solid-liquid interface and the transformation between solid and liquid. In spite of extensive theoretical work on solid-liquid interface structure and the transient ordering in liquids just before solidification, such phenomena have proven difficult to study experimentally using other techniques. Even with TEM, relatively few systems have been examined. The nature of the solid to liquid transition in Xe films has been determined using diffraction in an environmental cooling cell (Zerrouk et al., 1994). Imaging studies have shown the persistence of order into liquids, for example at the (211) interface in PdSi (Howe, 1996) and at the interfaces of liquid Xe inclusions in Al (Donnelly et al., 2002). A combination of energy filtered imaging and diffraction contrast has been used to examine the interface between Al-Si eutectic and solid Al-Si alloy, to determine that the interface is quite abrupt and that changes in crystallinity correlate with composition (Storaska et al., 2004). Finally, the Si crystal-liquid interface has been imaged at high

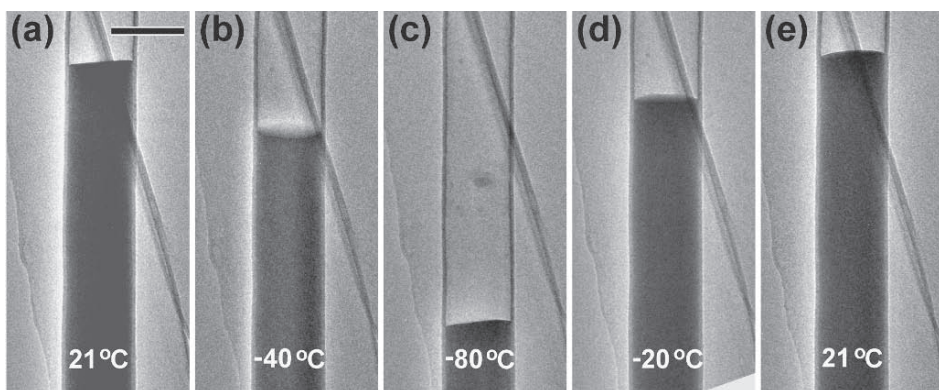


Figure 6–3. The Ga thermometer. Ga contraction and expansion inside a carbon nanotube upon cooling and heating. The background feature is part of the carbon support film. Scale bar = 100 nm. (a) At room temperature, 21°C. (b) At -40°C. (c) At -80°C, when solidification occurred. (d) The crystallized Ga was melted at -20°C. (e) Reheated to room temperature, 21°C. (Reprinted with permission from Z. Liu et al., © 2004 by the American Physical Society)

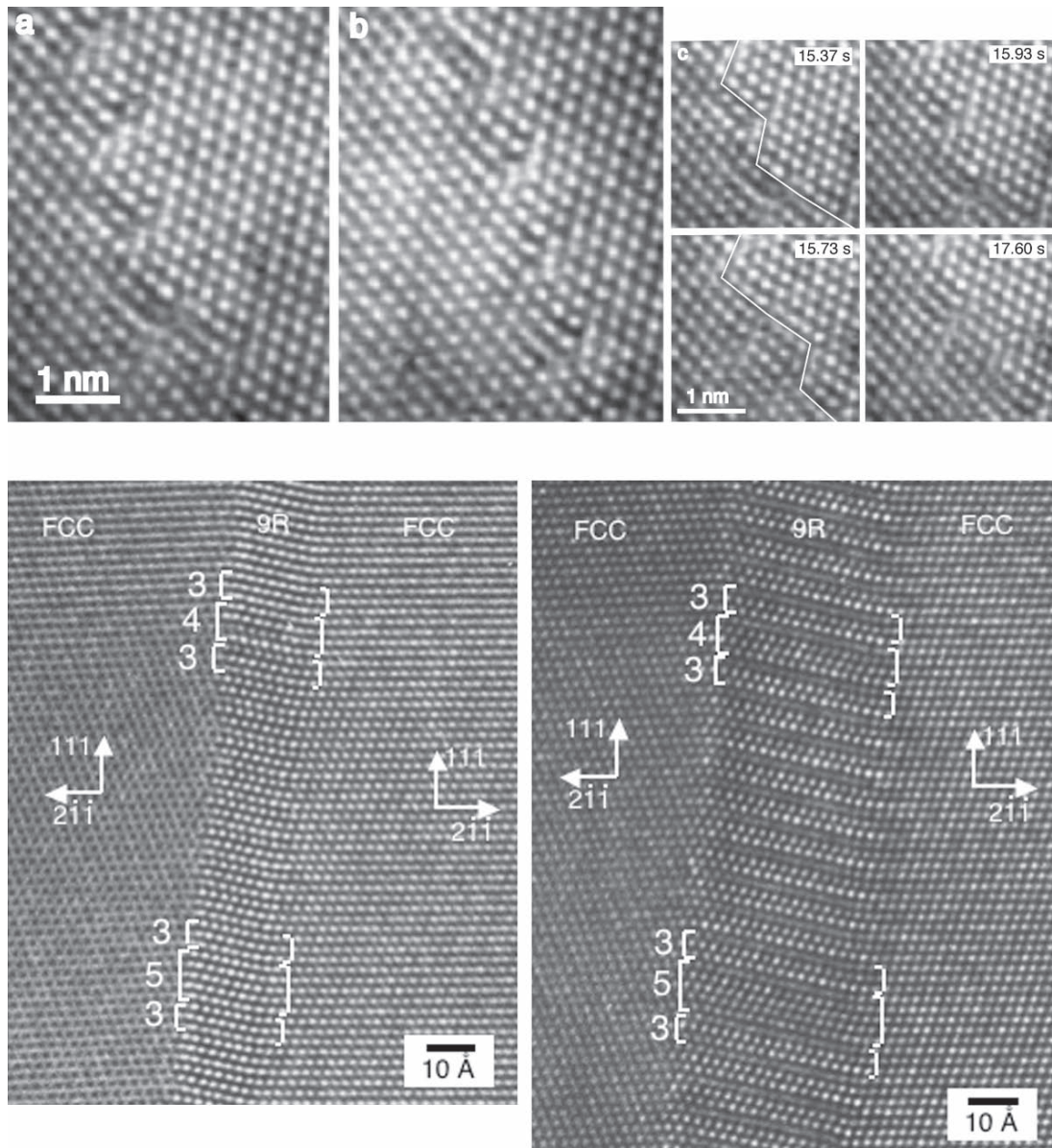


Figure 6-4. Grain boundary dynamics. (A) High-resolution electron microscopy images of a $[110]\theta = 14^\circ$ tilt grain boundary in Au at 893K. Individual frames are shown from a video sequence recorded near optimum defocus. (a) GB at $t = 15.37\text{ s}$. (b) GB has moved to the right at $t = 15.93\text{ s}$ and is near the $(6, -6, 1)$ symmetric orientation. (c) Detail of (a) depicted at various times in the four panels. A small region composed of eight atomic columns switches orientation between the two grains. Note the stacking disorder and misfit localization at the dislocation cores. Reprinted with permission from Merkle et al., © 2002b by the American Physical Society. (B) High-resolution image of the Cu $\Sigma = 3$ interface imaged along $[01-1]$. The grain boundary is dissociated into a narrow slab of 9R stacked material (fcc stacking but with an intrinsic stacking fault inserted every three planes). The two images were recorded 5 min apart after 400 kV electron beam irradiation and the 9R stacked region has expanded due to changes in the internal stress state induced by the beam. Stacking defects in the 9R structure can be related to the presence of secondary grain boundary dislocations at the interface. (From Medlin et al., 1998, with permission from Elsevier.)

temperature (Nishizawa et al., 2002) to determine the planarity of different index interfaces.

As well as static configurations at the solid-liquid interface, interface dynamics during solidification have been examined in several bulk materials. Arai et al. (2000, 2003) observed Si growth in the Al-Si system, while Sasaki and Saka (1996), Kamino et al. (1997a) and Saka et al. (1999) imaged surface melting in Al and Al_2O_3 , observing ledge motion during solidification. Other studies have involved nanoparticles and inclusions and will be discussed below.

2.1.3 Grain Growth and Grain Boundary Motion

Grain boundaries in polycrystalline materials can move on annealing or mechanical deformation. Just as we have seen for crystallization studies, *in situ* observation of grain boundary dynamics can supply information on the growth mechanism, and even measure the effects of impurities and gas atmosphere. Grain boundary motion during heating has been observed for metals such as Cu, Au, and Al (Keller et al., 1997; Dannenberg et al., 2000; Kaouache et al., 2003). For nanocrystalline Ag thin films, the measurement of kinetic parameters demonstrated that grain growth is dominated by surface diffusion mass transport (Dannenberg et al., 2000). Grain boundary motion during mechanical stressing will be discussed in Sections 5.1 and 5.3.

More complex grain boundary dynamics can also be studied. An interesting example is the penetration of liquid Ga along grain boundaries in Al, relevant to the important embrittlement process (Hugo and Hoagland, 1998, 1999). The structure and strain field during penetration, the kinetics in different grain orientations, and the effects of dislocations were observed.

While dark field imaging works well for grain boundary dynamics in polycrystalline films or at low symmetry boundaries, high resolution heating experiments are very useful for understanding high symmetry boundaries. High resolution experiments on bicrystals having engineered boundaries with high symmetry, particularly in Au and Cu (Medlin et al., 1998; Merkle and Thompson, 2001; Merkle et al., 2002a, b), enable very detailed measurements at the atomic level and the determination of grain boundary migration mechanisms. *In situ* experiments show that collective mechanisms operate during migration, and that unusual structures may form and grow at boundaries (Figure 6–5). Dislocations may also be emitted, and the details of their structure and relationship with the boundaries can be measured (Lucadamo and Medlin, 2002).

2.2 Structural Phase Transitions

As well as the phenomena of melting, solidification and grain boundary motion, *in situ* techniques have been applied to understand transformations between different crystal structures and solid state reactions involving diffusion. These experiments have mostly relied on *in situ* sample heating, although transformations have also been initiated by straining, electron beam heating, electric and magnetic fields, and a gas environment. High resolution imaging and analysis, diffraction, or

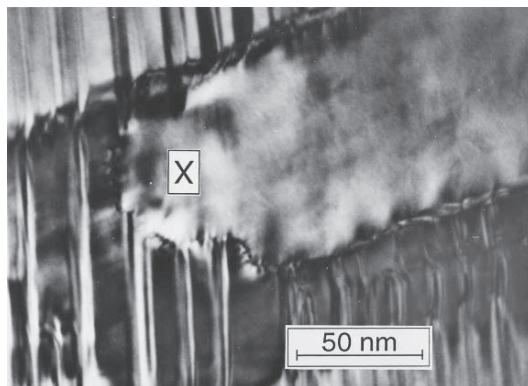


Figure 6–5. Phase stability in NiAl. When a martensitic Ni-rich $\text{Ni}_x\text{Al}_{1-x}$ sample, with $x > 63\text{at.\%}$, is annealed at moderate temperatures (550°C) it transforms into Ni_5Al_3 . On further heating to 780°C , the Ni_5Al_3 phase itself decomposes, forming B2 grains in a twinned L1_2 matrix. This image is part of a sequence obtained during heating that shows a smaller B2 grain growing by forming a small extension (marked as X) into the L1_2 matrix, consuming some twins, then rapidly expanding laterally. The Ni_5Al_3 phase is undesirable as it degrades the shape memory properties by inhibiting the transformation back to austenite, and its formation and stability are therefore important. (From Schryvers and Ma, 1995 with permission from Elsevier.)

low resolution weak beam or bright field imaging provide information that is complementary to that obtained from other *in situ* techniques, such as x-ray diffraction, which average over larger volumes.

Subtle changes in symmetry can be detected using the sensitive combination of diffraction and high resolution imaging. These combined techniques show the transformations between orthogonal, tetragonal, and cubic phases in oxides such as SrRuO_3 (Jiang and Pan, 2000). They also work well for transformations involving charge ordering and incommensurate phases, which will be discussed in Sections 4.1 and 4.3. Ordering can be investigated directly in the STEM, using its capabilities for elemental analysis of individual atomic columns. For example, Klie and Browning (2001) heated LaSrFeO_3 in the STEM, using the column environment, which is low in oxygen, to reduce the material. EELS showed that the resulting change in symmetry was due to ordering of oxygen vacancies.

When planning to study these sorts of phase transformations, it is important to consider the same experimental artifacts that we have already mentioned for melting and solidification. The results described below illustrate both the advantages and some pitfalls of *in situ* TEM.

We first consider transformations in intermetallic alloys such as shape memory alloys, which provide an excellent opportunity for *in situ* microscopy to display its strength. For example, for TiNi, the orientation relation between the different phases can be determined, and the dynamics of the emergence of martensite plates during straining can be observed *in situ* (Gao et al., 1996; Ma and Komvopoulos, 2005). *In situ* heating of NiAl alloys (Schryvers and Ma, 1995, Schryvers et al., 1998) showed how the texture and defect structure in the high tem-

perature phase are derived from the lower temperature phase, and illustrated the processes occurring during phase decomposition with low resolution imaging and diffraction (Figure 6–5). Higher resolution imaging showed details of the formation of the gamma phase in TiAl which would have been difficult to ascertain otherwise, for example, the ledge motion of interfaces (Howe et al., 2004). Other materials examined include the shape memory alloys CuAlMn (Dutkiewicz et al., 1995), TiNiHf (Han et al., 1997), and FeMnSi (Jiang et al., 1997). Crystallographic relationships, the interaction of dislocations with the transformation front, and the morphology of phases produced on heating or straining were studied. The presence and significance of incommensurate reflections in related materials have been examined using imaging plates and an in-column filter (Tamiya et al., 1998; Cai et al., 1999; Murakami and Shindo, 2001; Li et al., 2003). Cooling stages allow an even larger range of transformations to be accessed (Tanner et al., 1990).

However, thin foil effects are important in these transformations. Kuninori et al. (1996) showed that the foil thickness influences transformation temperatures—indeed, transformations do not occur at all at some thicknesses—and Ma and Komvopoulos (2005) showed that thickness can affect the sequence of phases. Electron irradiation effects are also important, for example in inducing some transformations in NiMnTi (Schryvers et al., 1996), and in changing the formation kinetics of the omega phase in beta phase Ti-Mo alloys on cooling (Matsumoto et al., 1999), a transformation which is important in understanding the anomalous electrical conductivity of these alloys.

Both beam and thin foil effects, of course, must be considered in any *in situ* transformation. Beam effects should always be evaluated by examining unirradiated areas after the transformation. Thin foil effects can be minimized in some cases by depositing the material of interest onto an electron transparent membrane. This reduces buckling and provides a more uniform temperature than a conventional specimen of varying thickness, advantageous for quantitative studies. An example is the transformation between beta and alpha phases of tungsten, for which the change in stress state is important in lithographic mask applications. Deposition of a uniform W film on a silicon nitride membrane (Ross et al., 1994a) allowed the transformation dynamics to be measured and the presence of voids to be related to the initial grain structure. Membrane specimens have been used successfully for many types of material, for example, by Morkved et al. (1998), Dannenberg et al. (2000), Kooi and de Hosson (2004), Grant et al. (2004), and Lee et al. (2005).

2.2.1 A Solid-State Diffusion Reaction: Silicide Formation

Reactions which occur at a planar interface between two materials have provided fruitful subjects for *in situ* experiments. *In situ* observations may allow determination of the diffusing species, the nature of nucleation sites, the sequence of phases, and the relationship between the crystal structures of the initial and final phases. However, the complexity of these reactions, compared to the crystallization and

melting reactions described previously, means that we have to be particularly careful to avoid artifacts. For example, if the sample dimensions are comparable to or less than the diffusion lengths of the moving species, then surface diffusion may affect the kinetics. Surface nucleation sites may be significant, and beam effects and stress relaxation in thin regions of the foil must be recognized. In spite of these issues, a successful body of work has been carried out on these transformations. We illustrate this by discussing silicide formation, a popular "test system" of great relevance to the microelectronics industry that has been examined using a range of *in situ* TEM techniques.

In situ silicidation was initially studied in cross section by heating a metal film such as Ti, Zr, or Cr that had previously been deposited on Si (H. Tanaka et al., 1995, 1996, 1998; Sidorov et al., 1998a; Figure 6–6A). Plan view experiments later provided the opportunity to examine silicidation on patterned substrates to study, for example, nucleation-limited transformations in small areas (Teodorescu et al., 2001; Ghica et al., 2001; Gignac et al., 1997; Figure 6–6B). These *in situ* experiments were very helpful in showing the sequence of phases, some of which are short-lived or hard to see otherwise; as mentioned previously, a single *in situ* experiment can replace a whole series of *ex situ* preparations (Wang and Chen, 1992). It is interesting to consider the sample geometry, however, as it illustrates some limitations of the *in situ* studies. In a cross sectional experiment, quantitative results are only obtained if surface diffusion pathways are suppressed (perhaps by coating the sample) and nucleation sites on the milled surface are minimized. It can only be assumed that the *in situ* experiment is an accurate representation of the bulk situation if both the activation energy of the reaction, and the final structure produced, are comparable with bulk experiments (Sinclair et al., 1988). In plan view, surface effects are not as significant, but thin film buckling must be considered.

Specialized *in situ* deposition techniques offer an interesting alternative way of looking at silicide formation. Rather than depositing a metal on the Si (or Ge) substrate *ex situ*, the substrate can be cleaned *in situ* in a UHV TEM and the metal then deposited *in situ*. The metal may be deposited onto a cool substrate which is then heated (Gibson et al., 1987; Ross, 2000) or it may be deposited at high temperature, where silicide phases form at once as islands (Ross et al., 1999a; H.P. Sun et al., 2005; Nath et al., 2005). To study the structure of such 3D islands in more detail, a combined UHV system allowing sequential TEM and STM imaging has been used to determine surface reconstruction as well as the sequence of phases (Tanaka et al., 2004). *In situ* deposition has also been used to study more complex silicide reactions, such as oxide and nitride mediated epitaxy (Kleinschmit et al., 1999; Chong et al., 2003). The experimental complexities of carrying out deposition *in situ* will be discussed in more detail in Section 3. But the advantages are clear in terms of avoiding contamination or oxidation (or evaluating their effects; see Figure 6–6C), discovering changes in the phase sequence as a function of film thickness, and looking at kinetic effects during deposition, such as coarsening.

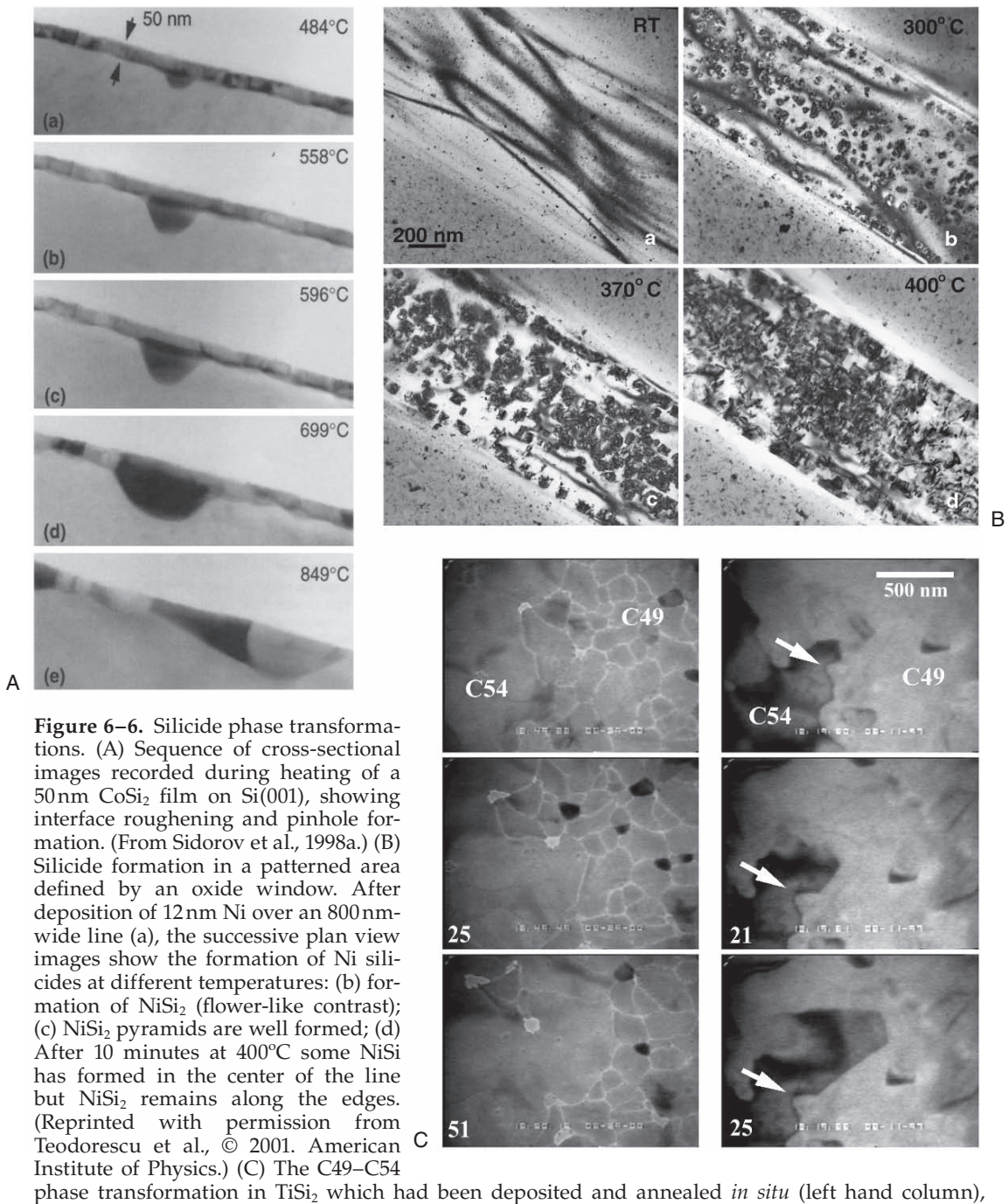


Figure 6–6. Silicide phase transformations. (A) Sequence of cross-sectional images recorded during heating of a 50 nm CoSi_2 film on $\text{Si}(001)$, showing interface roughening and pinhole formation. (From Sidorov et al., 1998a.) (B) Silicide formation in a patterned area defined by an oxide window. After deposition of 12 nm Ni over an 800 nm-wide line (a), the successive plan view images show the formation of Ni silicides at different temperatures: (b) formation of NiSi_2 (flower-like contrast); (c) NiSi_2 pyramids are well formed; (d) After 10 minutes at 400°C some NiSi has formed in the center of the line but NiSi_2 remains along the edges. (Reprinted with permission from Teodorescu et al., © 2001. American Institute of Physics.) (C) The C49–C54

phase transformation in TiSi_2 which had been deposited and annealed *in situ* (left hand column), compared to *ex situ* deposited TiSi_2 , where Auger spectroscopy showed the presence of oxygen (right hand column). Times are shown in seconds and the arrow marks a fixed point on the specimen. The phase transition occurs smoothly in the clean film while it is strongly pinned at grain boundaries in oxidized films. (Reprinted with permission from Ross, ©2000 AAAS.)

2.3 Phase Transformations in Nanostructured Materials

So far we have discussed phase transformations in bulk materials or thin films, where *in situ* microscopy allows us to see changes in structure, how phases nucleate, and how growth fronts propagate. But TEM is particularly good at imaging nanostructures; in other words, resolving the shape, structure, and composition of small regions of a specimen. Thus, the techniques applied to study transformations in bulk materials can naturally be extended to transformations in small volumes, either embedded in a matrix or free standing. The stability of phases and the mechanisms of transformations in small volumes have been determined for several cases, confirming the important general conclusion that small particles show different phase diagrams compared to larger volumes of the same material. This is especially important given the many applications of nanostructured materials, for example, in high strength metal alloys, and individual, free-standing nanoparticles, for example, as catalysts or components in advanced electronic devices.

2.3.1 Size-Dependent Transformations in Embedded Nanostructures

By focusing on an individual inclusion or precipitate, *in situ* microscopy provides precise information about phase transformations and stability in nanoscale volumes. Excellent quantitative work in several systems shows the potential of the technique for future studies on a wider range of materials.

Pb in Al is a model system, since the lack of solubility of Pb in Al means that Pb spontaneously forms small cuboctahedral inclusions with a cube-on-cube orientation relation. Heating experiments allow strain, melting, and diffusion phenomena to be studied. A fascinating range of size-dependent properties has been seen (Figure 6–7). Melting of the Pb particles is size-dependent with huge supercooling possible, and there is a hysteresis on solidification due to the difficulty of nucleating ledges (Gabrisch et al., 2000). The decay of strain during solidification and melting provides information on the diffusion of point defects (Zhang et al., 2004). In particles at grain boundaries, which have complex structures, the melting of each interface at a different temperature can be seen (Bhattacharya et al., 1999; Dahmen et al., 2004). Co-implantation of different materials into Al, such as Cd/Pb, Sn/Pb, or Tl/Pb, allows phenomena associated with phase separation, melting, and interface structure to be examined (Johnson et al., 2002) and binary phase diagrams determined as a function of size.

Phase transformations involving precipitate growth have provided equally interesting information. In cases where precipitates are pinned on dislocations, diffusion parameters can be measured from their coarsening (Legros et al., 2005) or motion (Johnson et al., 2004). The kinetics of ledge motion and kink nucleation on precipitates can be observed during high resolution heating experiments (Howe, 1998). For example, for precipitate plates in Al-Cu-Mg-Ag alloys, imaging parallel and perpendicular to the interface demonstrated that precipitates grow by the terrace-ledge-kink mechanism (Benson and Howe, 1997) and even

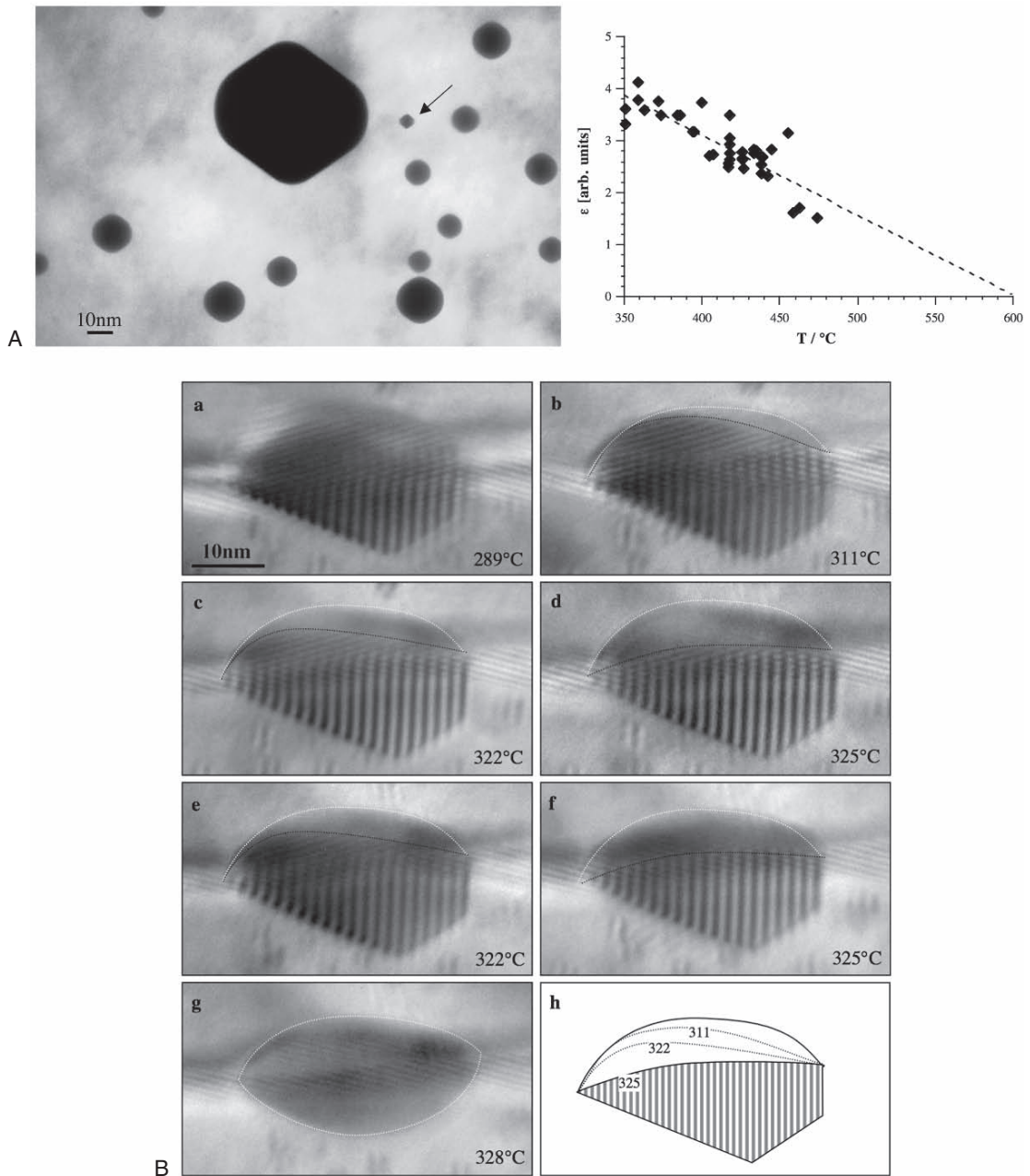


Figure 6-7. Nanoparticle melting phenomena. (A) Size-dependent melting of Pb inclusions in Al. The sample was produced by rapid solidification of an Al–0.5% Pb alloy and the image shows an array of particles at 423°C, which is 96°C above the bulk melting point. The rounding of most particles indicates their liquid state, while the smallest particles (arrow) are still faceted and solid. By measuring the dependence of inclusion shape on temperature and considering the inclusion shape change kinetics, the step energy as a function of temperature for steps on the inclusion surface can be calculated (lower graph). The least-squares fit indicates a roughening transition at about 600°C. (From Gabrisch et al., 2001 with permission from Elsevier.) (B) Reversible melting of 25-nm Pb inclusion at a grain boundary in Al (a–h). This particle has two different interfaces with two different grains and the two interfaces melt at different temperatures. The thin black line indicates the solid-liquid interface at different temperatures. (From Dahmen et al., 2004 with kind permission of Taylor and Francis Ltd.)

allowed the rate limiting steps and thermodynamic parameters of kink nucleation to be determined (Figure 6–8). Analytical techniques provide complementary information on the relationship between composition and structure at these growing interfaces, and the development of simulations for dynamic high-resolution imaging promises to make these studies even more quantitative (Howe et al., 1998). Other reactions, such as oxidation and reduction, can also be observed in precipitates (for example Isshiki et al., 1995; Kooi and De Hosson, 2001).

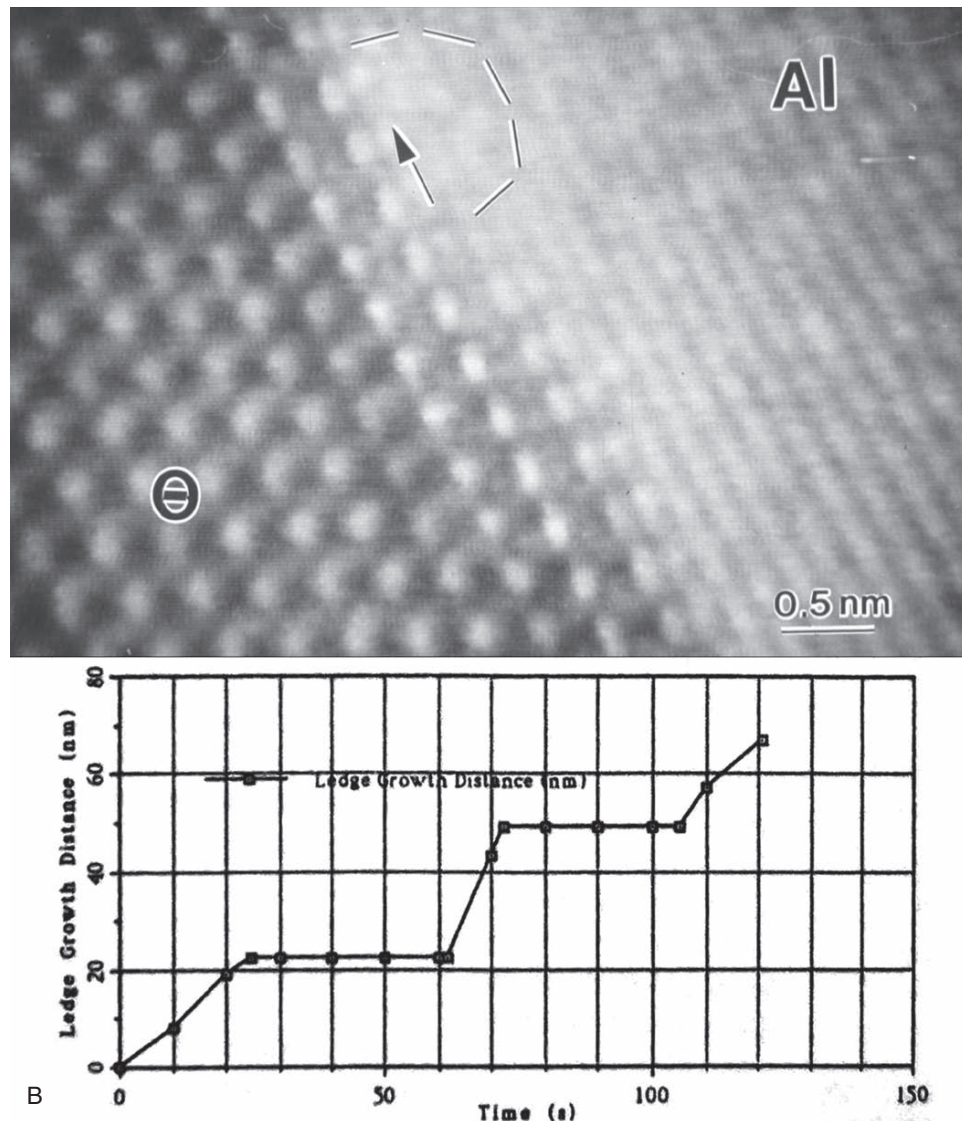


Figure 6–8. Precipitate growth mechanism. High-resolution image of a single ledge on a 111 $\bar{\theta}$ plate in an Al–Cu–Mg–Ag alloy during growth at about 220°C, and a graph showing the position of the ledge as a function of time demonstrating growth by irregular motion of ledges. The ledge height is two 111 matrix planes high (half a unit cell). The circled area appears blurred in videos due to enhanced atomic motion there. (From Howe et al., © 1998 Courtesy of Cambridge University Press.)

2.3.2 Phase Transformations and Sintering in Free-Standing Nanoparticles

Isolated nanoparticles are often used as catalysts, and this has generated interest in understanding the factors determining their shape, phase stability, and sintering. For precipitates, we have seen properties quite different from the bulk material. Similar results are found for free-standing nanostructures when studied *in situ*.

The earliest *in situ* studies of free-standing particles demonstrated the dynamic nature of the atomic arrangement (Smith et al., 1986; Iijima and Ichihashi, 1986), and the large fraction of atoms on or near the surface indeed leads to unusual behavior. TEM has shown that phase transformations in free-standing particles are different from those in bulk, for example in observations of size-dependent melting (Howe, 1997) and changes in phase stability (Chatterjee et al., 2004). In this context, binary systems such as Au-Sn, Pb-Sn, Bi-Sn, and In-Sn have been extensively studied. For this, a two-source evaporator is used to form mixed composition clusters *in situ* (Figure 6–9). The binary phase diagram is found to depend strongly on size, with changes in the eutectic temperature (Yasuda et al., 2001; Lee et al., 2002a). Melting behavior, phase separation, and mixing also depend on the composition and size (Yasuda et al., 2000, Lee and Mori, 2004a, b). These effects reflect a change in solubility or the relatively high cost of forming phase boundaries.

Unusual structures may occur in certain free-standing particles on melting. In Al-Si, a solid Al particle inside a molten Al-Si sphere can form, moving with fractional Brownian motion (Yokota et al., 2004). In GaSb, particles decompose into a crystalline Sb core surrounded by liquid Ga (Yasuda et al., 2004). Stress may also play an important role in particle reactions. Metals encapsulated within multiwalled carbon onions have changed melting points due to the pressure (Banhart et al., 2003; Schaper et al., 2005), and the metal can even migrate through the graphitic covering (Schaper et al., 2005). When there is a solid oxide layer covering a nanoparticle, stress relief can cause cracking (Storaska and Howe, 2004).

Sintering of free-standing particles is particularly important in materials processing and has been examined *in situ*. Ceramic particles such as SiN can be made to sinter in a conventional microscope provided that a very high temperature stage is used (Kamino et al., 1995). For metals, of course, the surface oxide strongly influences sintering. For example, the degree of sintering of Fe and Nb nanoparticles on membranes, prepared *ex situ* but observed at high resolution during annealing in high vacuum (Vystavel et al., 2003a, b), was found to depend on surface oxidation. To solve this problem, an integrated system may be used, where particles are created and imaged in the same high vacuum. Yeadon et al. (1997) connected a sputtering chamber to a UHV TEM to carry out successful studies of metal sintering. Sintering of Cu on Cu foils proceeded by neck growth and grain boundary motion, whereas Co particles on Cu and Ag foils “burrowed” beneath the surface to minimize surface energy (Zimmermann et al., 1999). Sintering of metal particles on oxide substrates in a controlled environment is of

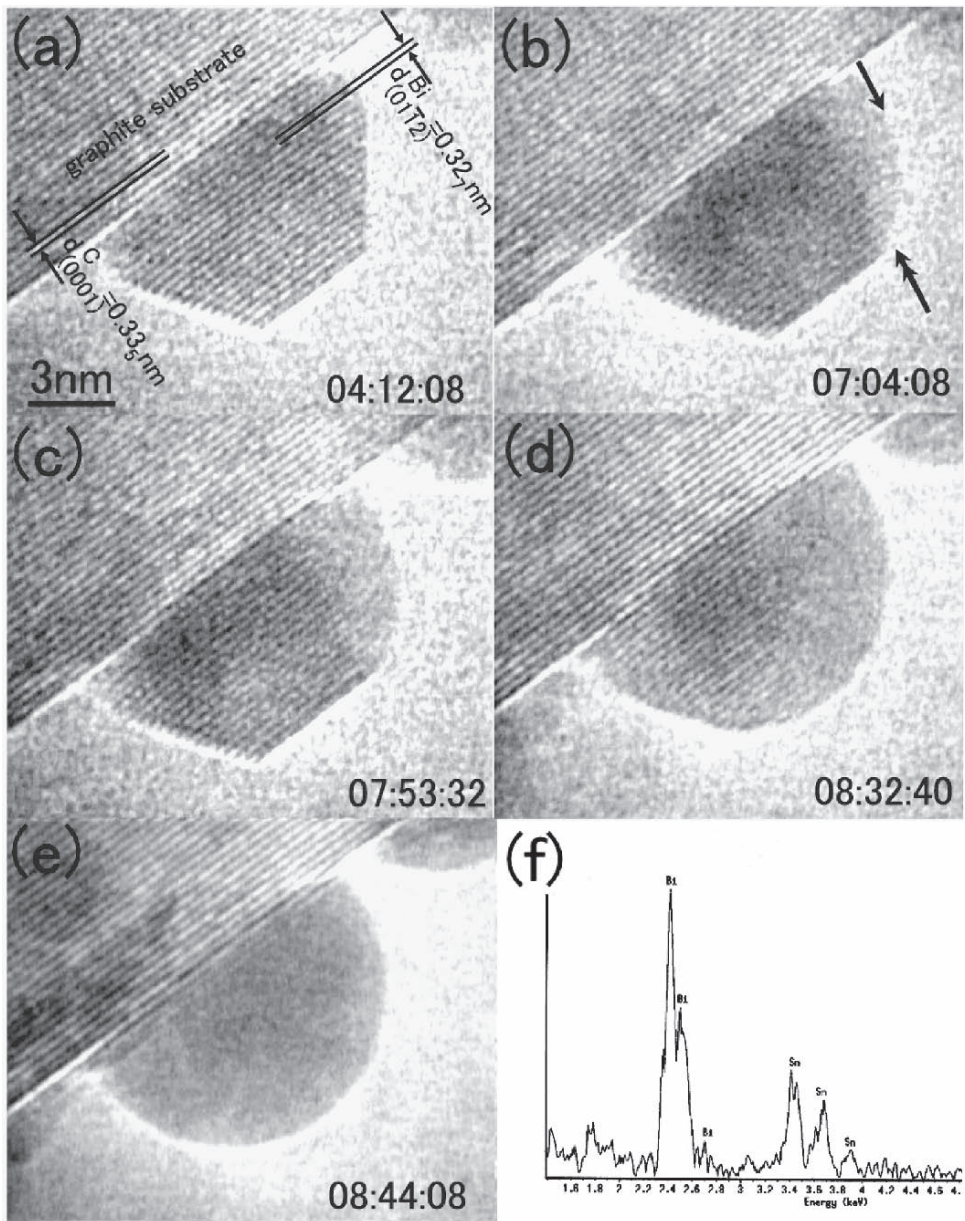


Figure 6-9. Intermixing in small particles. Sequence of images showing the alloying of Sn into Bi at 350K. (a) As-evaporated Bi particle; (b–e) the same particle during *in situ* Sn deposition. First a crystal-line–liquid interface forms [arrows in (b)] and this then propagates through the crystal until the whole particle becomes liquid. EDX shows a composition of 50% Sn at this point (f). Not shown is the asymmetric behavior of Sn particles during Bi deposition; these become liquid at once without forming a phase boundary, an abrupt crystalline to liquid transition that is not expected from the bulk phase diagram. (From Lee and Mori, 2004a with kind permission of Taylor and Francis Ltd.)

particular relevance to catalysis, and will be discussed in that context in Section 3.2.

2.4 Summary

In situ microscopy of phase transformations has touched on a wide range of materials and addressed important problems related to crystallization and melting, diffusion, structural transformations, and grain boundary dynamics. Bulk crystals, embedded nanostructures, and free-standing nanoparticles have been studied, yielding quantitative information on reaction mechanisms and on the relationship of structure to dynamics. From this survey of results, it is clear that the *in situ* techniques we have described could be applied to many currently unstudied systems. However, for proper interpretation of results, care must be taken with thin foil effects, such as strain, surface diffusion and surface nucleation, and with beam effects. High voltage microscopes have significant advantages in minimizing thin foil artifacts, though at the cost of increased beam damage. But even at intermediate voltage, careful accounting for these effects can lead to quantitative results relevant to materials development.

3 Surface Reactions and Crystal Growth

A unique application of *in situ* microscopy, building on some of the techniques we have discussed above, is the examination of surface reactions and crystal growth. Rather than looking at bulk transformations as in Section 2, here we are more concerned with changes to the specimen surface. These changes may be initiated by heating or by exposure to a reactive environment or deposition flux. It is possible to study atomic scale processes on surfaces, including step dynamics and surface phase formation, as well as the growth of thin films and nanostructures. As we might expect from the discussion in Section 2, these *in situ* surface studies allow transient structures to be seen and kinetics to be measured. We will show that such experiments indeed contribute to an understanding of both surface reactions and growth, in some cases leading to improved control of surface structure or crystal size and shape.

These studies usually take place in a controlled environment TEM. The column of a standard TEM contains a mildly reducing atmosphere of 10^{-6} to 10^{-7} mbar and may also be contaminated with hydrocarbons. By controlling the environment, the specimen can be exposed to, for example, clearly oxidizing or reducing conditions, a solvent rich atmosphere to prevent dehydration (see Section 7), or an environment that allows vapor phase growth. Many such experiments can be carried out by leaking gases into the specimen area of a conventional TEM. However, some specimens require a microscope capable of UHV base pressure to avoid any background contamination. Such microscopes can be complex and expensive, but they enable experiments which can not be realized otherwise, especially if adjacent chambers are available for sample preparation. Major advances in surface science have been

achieved using UHV microscopy, and the equipment and the science have recently been reviewed by Poppa (2004).

3.1 Measurement and Modification of Surface Structure

Step flow and the development and stability of surface structures such as reconstructions may be studied by controlled heating, beam irradiation, or environmental stimuli such as deposition or exposure to a reactive environment. It may appear surprising that TEM is appropriate for surface studies at all, since the issues of temperature nonuniformity and strain relaxation associated with the preparation of thin foils could be avoided completely by using techniques such as LEEM and UHV SEM. But TEM has a wide variety of imaging and analytical modes sensitive to different aspects of a surface, and can be highly quantitative in terms of image analysis. Scanning probe microscopy also provides sensitive imaging of surface structures but lacks the time resolution necessary for surface dynamics, requiring typically 30 seconds to acquire each frame.

In situ TEM initially gained attention as a surface science tool with the successful determination of the Si (111) 7×7 reconstruction (Takayanagi et al., 1985), an accomplishment which STM and LEED had not been able to achieve at that time. A clean Si surface was prepared by heating in a UHV TEM and diffraction patterns were obtained and analyzed. Since then, many other static and dynamic surface structures have been determined after *in situ* preparation.

Surface structures may be prepared in the UHV microscope column by heating or deposition onto a thin foil (e.g., Kamino et al., 1997a; Oshima et al., 2000; Liu et al., 2001), or may be prepared in an adjacent chamber connected to the microscope by UHV (Marks et al., 1998). Every possible mode of the TEM has been used to analyze these surface structures. In plan view, diffraction techniques have solved reconstructions of metals on Si (Collazo-Davila et al., 1998; Oshima et al., 2000). Reflection electron microscopy (REM) has been used extensively to examine surface step dynamics due to electromigration, and the effect of metal adsorption on surface structure (Aoki et al., 1998; Minoda and Yagi, 1999; Minoda et al., 1999; Latyshev et al., 2000; Figure 6-10A). REM has also provided useful information on polar surface structures in oxides (Gajdardziska-Josifovska et al., 2002) and decomposition of the InP surface on heating (Gajdardziska-Josifovska et al., 1997). Information from REM and plan view TEM is complementary to that obtained from *in situ* SEM (Homma and Finnie 2002). Profile imaging, in which a surface parallel to the beam is imaged at high resolution, shows directly the periodicity and corrugations associated with surface reconstructions. This was first recognized early on (Marks, 1983; Bovin et al., 1985; Mitome et al., 1990; Smith et al., 1993), and has recently helped to determine complex structures like Si (5 5 12) (Liu et al., 2001) as well as faceting, reconstructions and dynamics of Au-decorated Si surfaces (Kamino et al., 1997b; Figure 6-10B) and beam-induced changes in surface structure and stoichiometry (Ning et al., 1996).

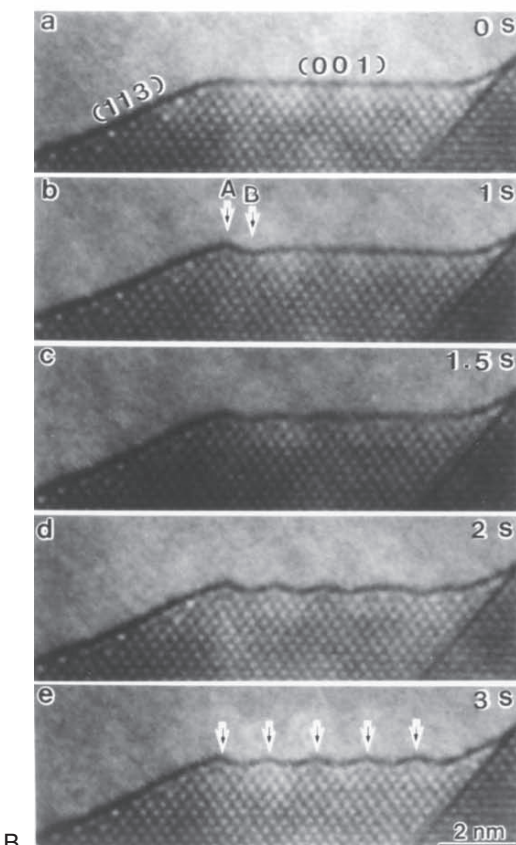
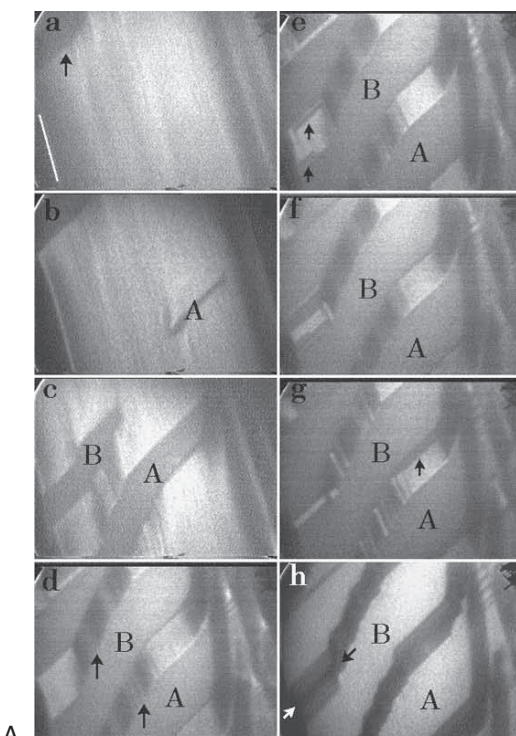


Figure 6–10. Deposition of Au on Si observed by different *in situ* imaging modes. (A) Step bunching on vicinal Si(001). A series of REM images obtained during the deposition of Au at 800°C onto a vicinal (4° miscut) Si(001) surface shows first the formation of (001) terraces in (a) and (b). Step bunching and formation of step bands are shown in (c) and (d); facet nucleation on the step bands is shown in (f) and (g). Finally there is a complete transformation of the entire vicinal surface into a hill-and-valley structure of (001) superterraces and (119) and (117) facets (h). (From Minoda et al., 1999 with kind permission of Taylor and Francis Ltd.) (B) The Au-induced reconstruction of a flat Si(001) surface on heating. The sample was prepared by depositing Au onto a rough, oxidized Si particle. The irregular sample geometry means that the temperature is not accurately known. However, on heating, the Au first agglomerated; further heating caused the oxide layer to disappear and the Au to spread over the surface (dark line along the sample edge), causing localized faceting into (001) and other terraces. The (001) facets then reconstruct over the timeframe shown, starting from the terrace boundary (arrows A and B). (Reprinted with permission from Kamino et al., © 1997 by the American Physical Society.)

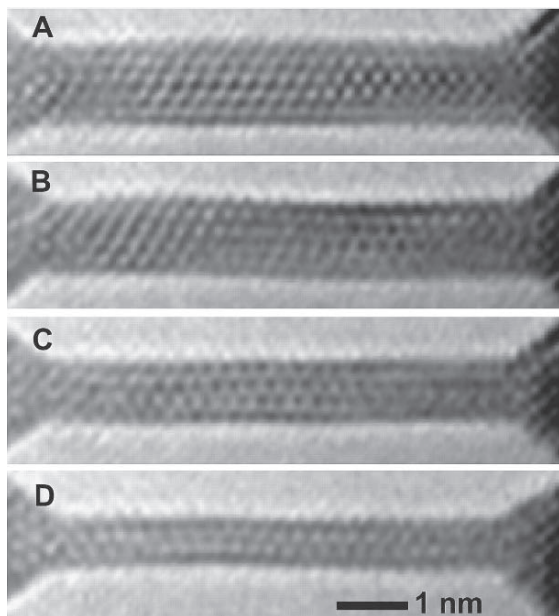


Figure 6-11. Nanostructures formed by surface mobility. Images of stable Au nanowires observed during the electron beam thinning of a specimen. The diameters of the wires are (A–D) 1.3, 1.1, 0.8, and 0.6 nm, respectively. The wire images are wavy, especially the thinnest, and can be modeled with helical structures. (Reprinted with permission from Kondo and Takayanagi, © 2000, AAAS.)

Surface diffusion under beam irradiation is evident during profile imaging. This has been used to advantage to study narrow wires *in situ*. Two adjacent holes are formed in a thin foil and the neck between them observed as it thins and breaks due to inbuilt stresses. Such experiments show a variety of interesting non-bulklike structures in Au (Figure 6-11), such as single chains (Koizumi et al., 2001) and helical multishell wires (Kondo and Takayanagi, 2000; Oshima et al., 2003a), with some of the structures related to shear (Oshima et al., 2003b). Beam-induced atom migration reduces the dimensions one layer at a time (Oshima et al., 2002). Unusual wire structures also form in Pt (Oshima et al., 2002). The surface diffusion of single atoms, for example W on MgO, can be imaged in TEM (N. Tanaka et al., 1998).

Controlled environment and UHV TEM thus has an excellent track record for creating and observing surface reconstructions and observing step motion and surface diffusion. We now focus on some specific applications where the ability to characterize and modify surfaces *in situ* has led to particularly interesting and significant advances.

3.2 Catalysis

Controlled environment TEM has enabled pioneering studies of the structural details of reactions during heterogeneous catalysis (Gai, 2002a; Sharma, 2001, 2005). High resolution imaging can be carried out at high temperature and under a controlled gas environment, up to several millibar of, say, H₂, CO, or O₂. Catalyst surface structure has been related to reactivity, intermediate phases have been determined, and changes in catalyst structure have been visualized during activation and poisoning. Several controlled environment TEMs are in opera-

tion in industrial laboratories, and we suspect that the many important results remain proprietary!

Most studies have focused on catalysts consisting of metal particles on an oxide substrate (Figure 6–12). Gai et al. (1990) first examined shape changes in Cu particles in oxidizing and reducing environments, and observed the stability of Pt and Ru particles on TiO₂ (Gai 1998; Gai et al., 2000). Hansen et al. examined the effect of Ba promoters on surface structures in Ru particles (2001), and used the shapes of Cu particles to determine relative surface energies under oxidizing and reducing conditions (2002; Figure 6–12B). Regeneration processes are important in such catalysts, and here too *in situ* studies have proven useful. For example, during regeneration of Pd/Al₂O₃ catalyst, sintering also takes place. The sintering behavior of “used” Pd particles, studied using analytical TEM as well as controlled environment heating, is affected by hydrocarbons which build up during use of the catalyst (R.-J. Liu et al., 2004; Figure 6–12A).

A wide variety of other materials and reactions have also been investigated under a controlled environment. Gai and Kourtakis (1995) observed a glide shear rearrangement in vanadium pyrophosphate during reduction, and developed a model for the surface activity of this material, which is important in butane catalysis. Sharma et al. (2004a) examined structural changes during reduction of CeO₂ catalyst, and interestingly used *in situ* energy loss spectroscopy to determine oxidation states as a function of temperature. Even the growth of polymeric reaction products *in situ* has been observed (Crozier et al., 2001; Gai, 2002b). Other reactions include intercalation in some interesting layered structures (Diebolt et al., 1995; Sidorov et al., 1998b), the nitridation of zirconia (Sharma et al., 2001), and de- and rehydroxylation of the lamellar material Mg(OH)₂, which is important in CO₂ sequestration (McKelvy et al., 2001). The reaction of MgO with water vapor has also been observed *in situ* (Sharma et al., 2004b; Gajdardziska-Josifovka et al., 2005).

Finally, photocatalysis can be studied *in situ* if a UV light source is brought into the specimen area. High resolution *in situ* imaging of the decomposition of hydrocarbons deposited on a TiO₂ film (Yoshida et al., 2005) provides information on the mechanism of the process. These exciting results suggest that *in situ* studies will continue to have an important impact in the future development of catalysts and other functional materials.

3.3 Oxidation of Surfaces

Corrosion of metals has significant impact on industry, so it is important to gain a fundamental understanding of oxidation and reduction by comparing controlled observations with theoretical predictions. For copper, oxidation was found to proceed via nucleation, growth, and coalescence of oxide islands (Figure 6–13). This result allowed the development of oxidation theories beyond simple models that had assumed a continuous oxide film (Yang et al., 1998, 2002; Zhou and Yang, 2002, 2003). Other than Cu and its alloys (Wang and Yang, 2005),

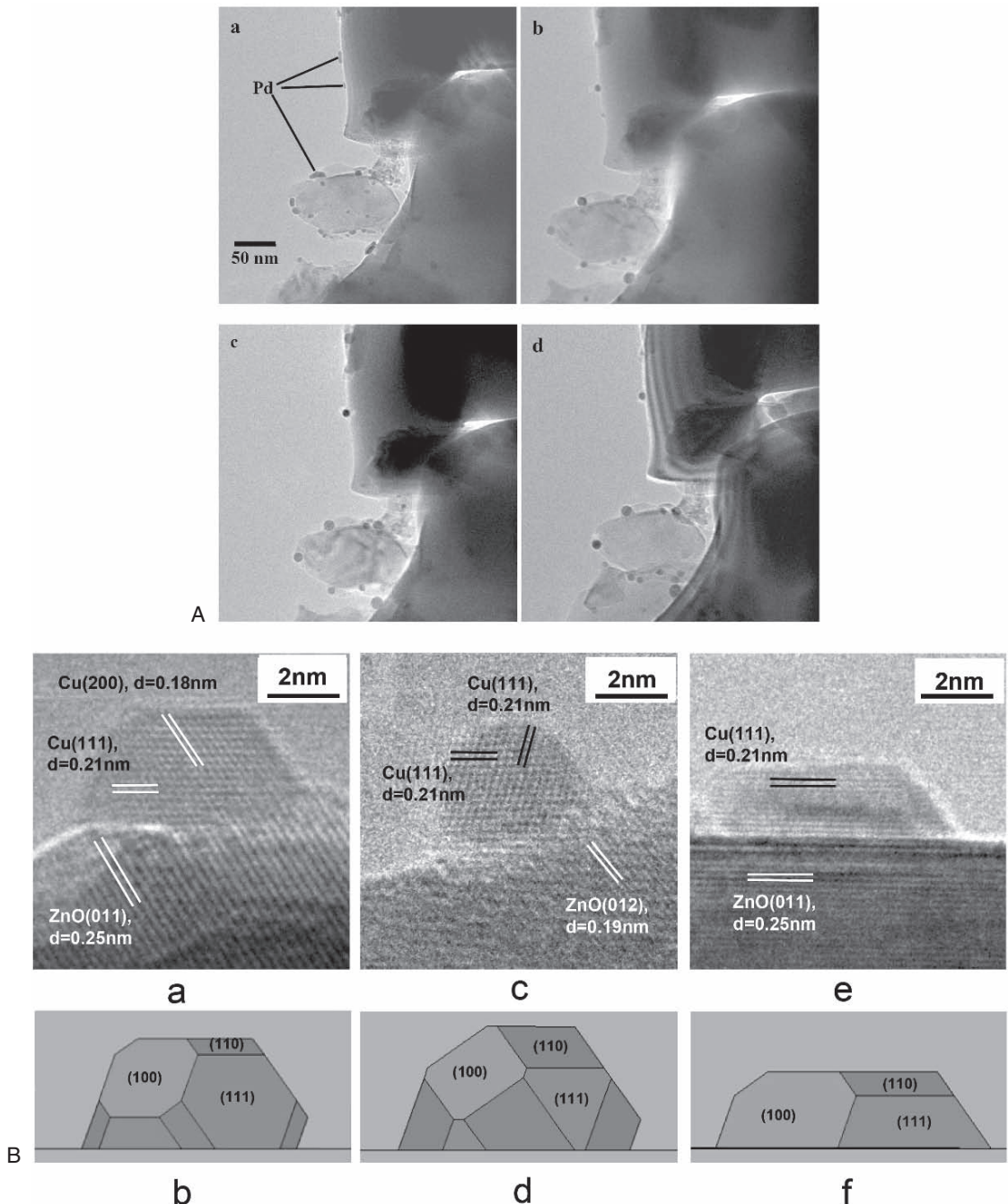


Figure 6-12. *In situ* imaging of catalysts. (A) Fresh Pd/Al₂O₃ catalyst (used for hydrogenation of acetylene) (a) in the as-received condition (room temperature), and (b-d) after heating in 500 m Torr steam at 700°C for 1, 4, and 7 hours. Catalysts are regenerated by heating in steam to remove hydrocarbon buildup, but this causes sintering of the metal particles, reducing activity. *In situ* experiments show that, for fresh catalysts, sintering is by conventional Ostwald ripening, while movement and coalescence occurs for used catalysts. (Reprinted with permission from R.-J. Liu et al., © 2004 AAAS.) (B) Images of a Cu/ZnO catalyst (the methanol synthesis catalyst) in various environments at 220°C, together with the corresponding Wulff constructions of the Cu nanocrystals. (a, b) 1.5 mbar H₂ at 220°C; (c, d) in a mixture of H₂ and H₂O with ratio 3:1 at a total pressure of 1.5 mbar; (e, f) in a mixture of 95% H₂, 5% CO at a total pressure of 5 mbar. These images allow the relative surface energies to be determined as a function of environment. (From Hansen et al., © 2002. Courtesy of Cambridge University Press.)

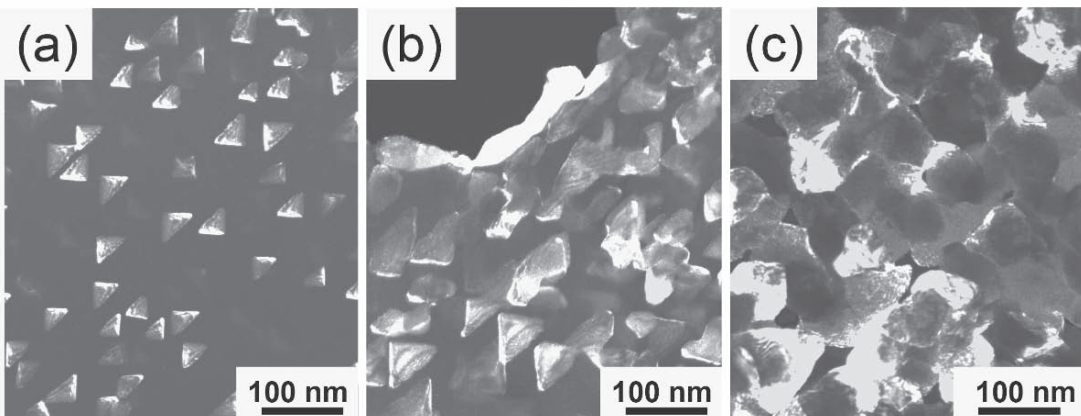


Figure 6-13. Mechanism of copper oxidation. Dark-field images obtained during oxidation of Cu at 0.1 Torr and 350°C in a UHV TEM. Imaging using the Cu₂O {110} reflection showed that oxidation is not planar, but takes place by Cu₂O island (a) nucleation (5 min), (b) growth (15 min), and (c) coalescence (25 min). The specimen was prepared by floating a 60-nm Cu film onto a support and then removing the surface oxide *in situ* by annealing at 350°C in methanol vapor for 15–30 min. The area and number density of the islands grown both at low pressure and at high pressure (shown here) were modeled using Johnson–Mehl–Avrami–Kolmogorov theory to give surface diffusion parameters. (Reprinted with permission from Yang et al., © 2002. American Institute of Physics.)

metal oxidation remains largely unstudied, but *in situ* experiments could clearly offer the possibility of improving corrosion resistance through alloying or surface processing.

Silicon oxidation is another industrially significant process, as a defect-free Si/SiO₂ interface is fundamental to transistor operation. For Si(111) (Figure 6-14A), forbidden-reflection imaging showed that steps do not move during oxidation, meaning that any surface roughness remains during processing (Ross and Gibson, 1991; Ross et al., 1994b). For Si(001), the same result is seen (Figure 6-14B). Forbidden reflection experiments are useful in their ability to probe the buried Si/SiO₂ interface, and are complementary to results obtained by *in situ* scanning reflection electron microscopy (Ichikawa, 1999).

High resolution imaging provides insights into reactions in more complex materials. By oxidizing and reducing niobium oxides, Sayagues and Hutchison (1996, 2002) showed the formation of a series of block structures with changing stoichiometry (Figure 6-15). The combination of analytical techniques with imaging would undoubtedly lead to further useful insights into oxidation and related reactions.

3.4 Growth of Carbon Nanostructures

The growth of carbon nanostructures has been extensively studied *in situ* since the discovery of these interesting materials by TEM. It is relatively easy to form carbon structures *in situ* with a controlled environment plus a catalyst or a graphitic precursor (Figure 6-16). Beam effects provide an important ingredient in the synthesis, especially if catalysts are not used. The beam interacts with the atmosphere above the specimen producing a plasma that can generate fullerenes (Burden and Hutchison, 1998). Alternatively, irradiation of graphitic materials

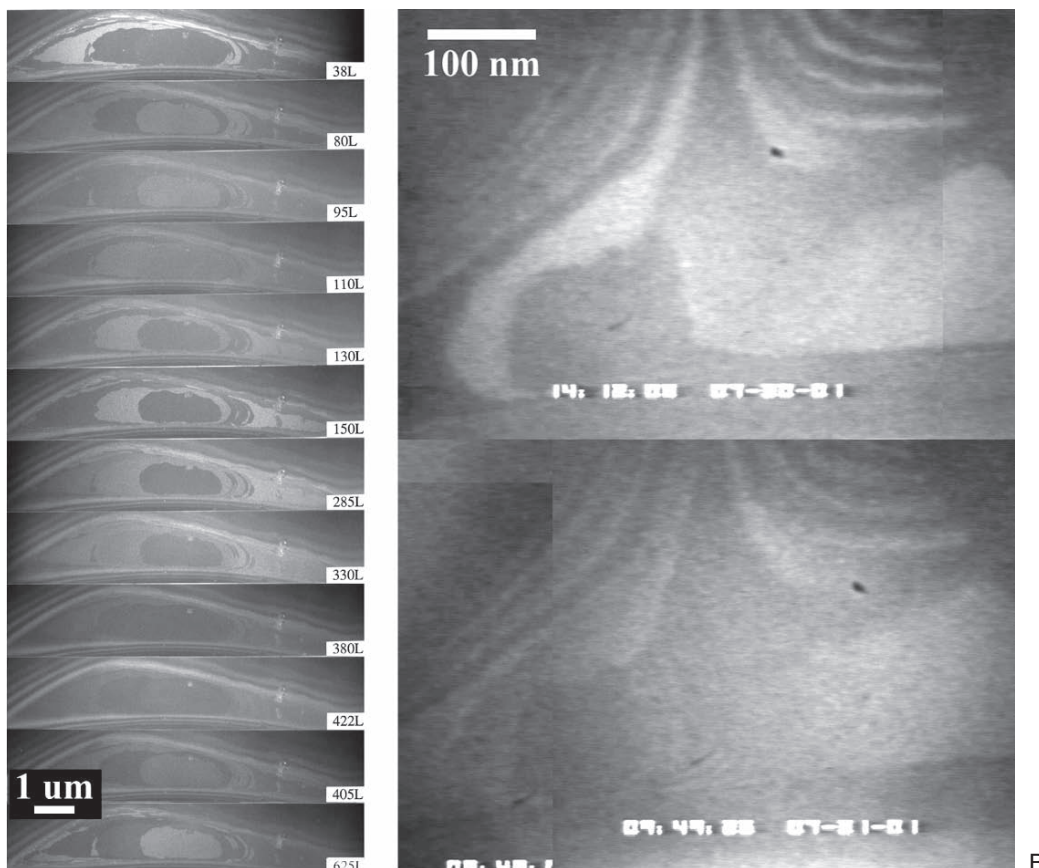


Figure 6–14. Mechanism of silicon oxidation. (A) Series of images of an Si(111) sample observed in plan view during oxidation in 2×10^{-6} Torr water vapor at 400°C . The time of each frame is given. A $1/3$ (422) forbidden reflection was used to form the images so that the gray levels correspond to terraces, with intensities repeating every unit cell (three steps). Steps do not move during oxidation of several layers showing that step sites are no more reactive than terrace sites. (Reprinted with permission from Ross and Gibson, © 1991 by the American Physical Society.) (B) Two images of an Si(001) sample observed before and after oxidation in air at room temperature. A $1/4$ (220) forbidden reflection was used to form these images. The steps do not move on this surface either.

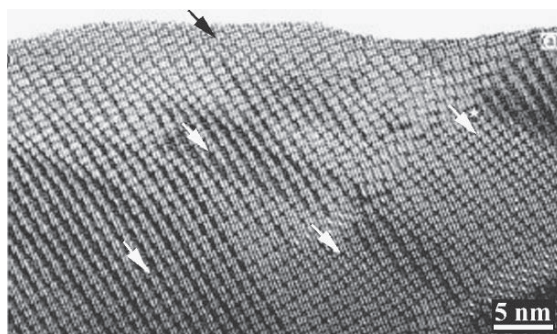


Figure 6–15. Oxidation of a block oxide structure. High-resolution image of an $\text{Nb}_{22}\text{O}_{54}$ crystal after heating by the electron beam and exposure to 15 mbar oxygen. The partly oxidized structure consists of microdomains of $\text{Nb}_{10}\text{O}_{25}$ (arrowed) in an $\text{Nb}_{22}\text{O}_{54}$ matrix. These images have been used to identify the structure of the $\text{Nb}_{10}\text{O}_{25}$ phase and the complete oxidation sequence from $\text{Nb}_{12}\text{O}_{29}$ to $\text{Nb}_{10}\text{O}_{25}$ has been determined using *in situ* experiments. (From Sayagues and Hutchison, 2002 with permission from Elsevier.)

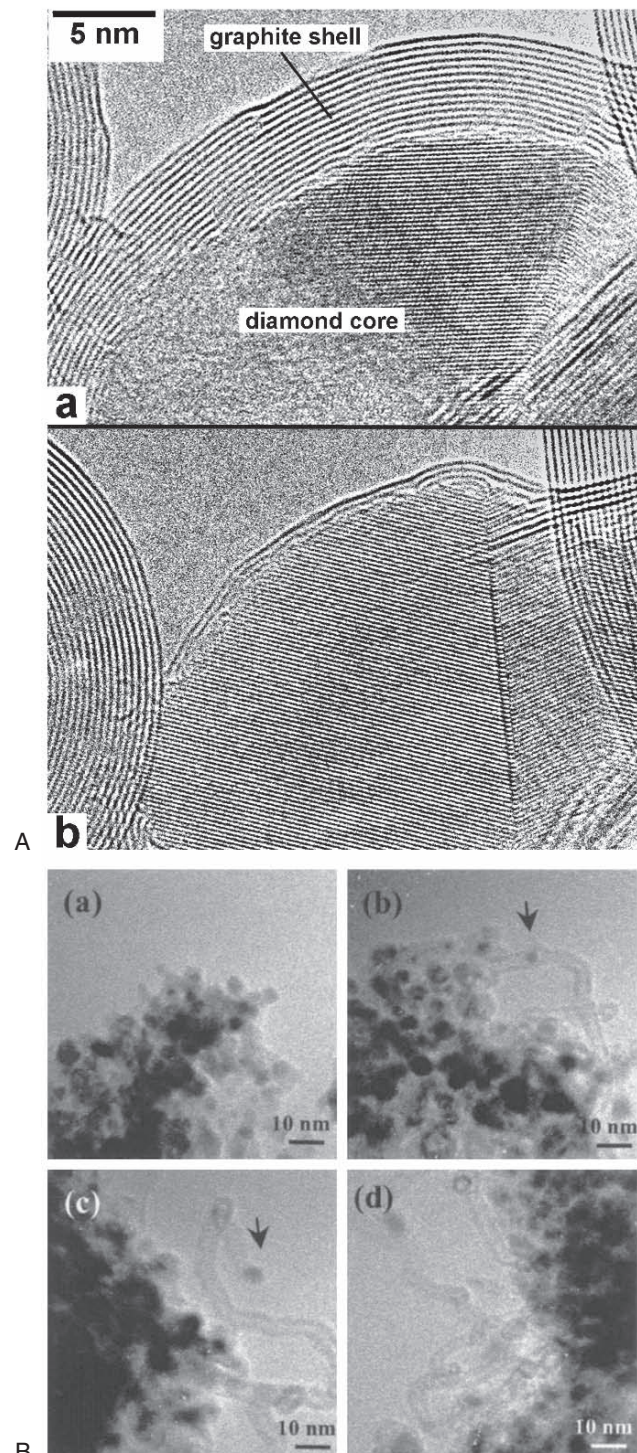


Figure 6-16. Carbon nanostructure growth *in situ*. (A) Formation of diamond *in situ*. Polyhedral graphitic particles were produced by arc-discharge and were transformed into perfectly spherical onions by electron beam irradiation above 600K. The decreasing distance between shells toward the center showed that the onions are in a state of high self-compression. The nucleation of cubic diamond occurs in the centers of the onions during irradiation above 900K, and the diamond grows until, surprisingly, almost all the onion shells are consumed. (a) After 2 h of irradiation at 1.25 MeV and 20 mA cm^{-2} . (b) After a further hour of irradiation. A typical twin is visible in the diamond. High pressure appears necessary to nucleate the diamond, but further growth is by beam-induced defects. (Reprinted with Permission from Banhart, © 1997. American Institute of Physics.) (B) Growth of multiwalled carbon nanotubes by catalytic chemical vapor deposition. Bright-field images showing an Ni-SiO₂ catalyst (a) exposed to H₂ at 450°C; (b) after exposure to acetylene (300 mTorr of an H₂-C₂H₂ mixture), and (d) another part of the sample after 3 min. The arrows show an individual Ni particle. At higher temperatures single-walled tubes formed but with catalysts present at the bases rather than the tips of the tubes. (Reprinted with permission from Sharma and Iqbal, © 2004. American Institute of Physics.)

generates point defects which deform the graphitic sheets, forming new structures (Ugarte, 1992; Banhart, 1997), while irradiation of materials such as Cu implanted with C causes graphitic onions to grow (Abe et al., 2002). Familiar or new C and BN structures, and even formation of diamond from graphite, can thus be observed *in situ* (Ugarte, 1992; Ru et al., 1996; Niihara et al., 1996; Banhart, 1997, 1999, 2003; Bengu and Marks, 2000; Roddatis et al., 2002; Troiani et al., 2003; Gloter et al., 2004; Wang et al., 2005).

Carbon nanotubes are of particular interest, and can be grown *in situ* by introducing a precursor gas such as methane, propylene, or acetylene over a catalyst (Sharma and Iqbal, 2004; Sharma et al., 2005). During growth, individual catalyst particles change their shape, and nucleation sites can be identified (Helveg et al., 2004). Once grown, carbon nanotubes can be modified with the beam (Terrones et al., 2000, 2002) to produce more complex structures.

3.5 Epitaxial and Polycrystalline Thin Film Growth

The experiments in Section 3.4 have shown the exciting possibilities for controlled environment growth of nanostructures. Continuous thin films can also be grown *in situ*, and this allows important processes such as nucleation, development of surface morphology, and relaxation to be observed. Although some studies describe polycrystalline film growth (for example Al; Drucker et al., 1995), most systems examined *in situ* have been epitaxial. These include Au on MgO (Kizuka and Tanaka, 1997a, b), Ge on Si (see below), and silicides on Si (Section 2). These experiments can provide detailed and quantitative information if growth conditions such as flux and temperature are calibrated carefully.

The most detailed studies have examined Ge and SiGe epitaxy on Si. This is a “test system” for studying epitaxial growth phenomena which also has great relevance to the development of microelectronic devices. A true UHV environment is required for the experiments, as the Si substrate foil is cleaned by heating in UHV to above the oxide desorption temperature. Growth is then carried out by UHV-CVD using gases such as disilane or digermane. Growth was observed by Krishnamurthy et al. (1991) in STEM, and by Minoda and Yagi (1996) and Ichikawa et al. (1998) in REM. But most work in this system has been carried out using conventional weak beam imaging in plan view, giving the highest sensitivity to strain fields (Figure 6–17). LeGoues et al. (1996) and Hammar et al. (1996) grew Ge on Si(111) and (001) *in situ*, clearly imaging the initial surface reconstruction, the nucleation of Ge islands, and later their growth and coalescence. The structures produced depend strongly on growth conditions. By varying the parameters, a range of fascinating phenomena now known to be common in other epitaxial systems was observed, such as the change in island shape during the introduction of stress-relieving dislocations (LeGoues et al., 1994, 1995). The range of structures observed in these studies would have been tedious to capture *ex situ*, and dynamic phenomena

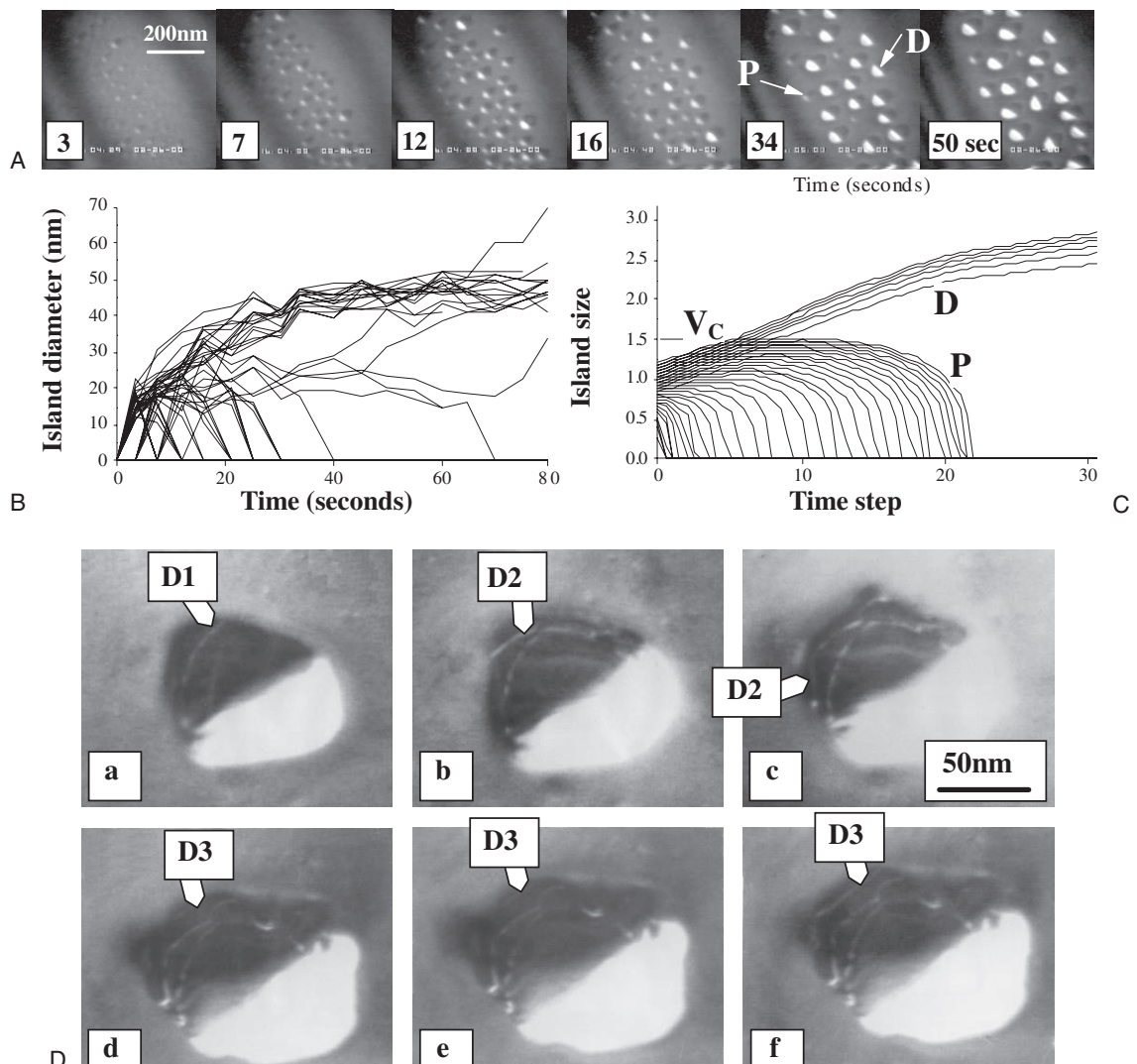


Figure 6-17. Ge island nucleation, growth, and relaxation. (A) Island coarsening. A series of video frames showing stages of island growth within a $0.5\mu\text{m} \times 0.5\mu\text{m}$ area. Growth conditions were 5×10^{-7} Torr Ge_2H_6 and 650°C . Weak beam images were acquired in a (g, 3g) condition with $g = 220$. The time of each frame after “nucleation” (first appearance of islands) is given. (B) The time evolution of every island within the area. (C) A simulation showing the fate of islands with different initial sizes, based on a modified Ostwald ripening process in which islands coarsen but also undergo a shape transition at V_c . The scale of the plot is chosen to match the data shown in (b). (Reprinted with permission from Ross et al., © 1998 by the American Physical Society.) (D) The introduction of dislocations into a partially relaxed island. Images were obtained 59, 94, 96, and 140 min after the beginning of growth, with the last three images taken within 1 s of each other. Growth conditions were 650°C and 10^{-6} Torr of 10:1 He:GeH₄. Only dislocations in the dark part of the image can be seen (D1–D3). (From Hammar et al., 1996 with permission from Elsevier.)

such as island shape changes and the essential role of Ostwald ripening (Ross et al., 1998) would not have been detected without the use of *in situ* TEM. Changes caused by the presence of surfactants during growth have also been examined *in situ* (Maruno et al., 1996;

Portavoce et al., 2004). It is interesting to note that complementary studies using *in situ* LEEM have been important in fully understanding growth in the SiGe system, as LEEM is more sensitive to surface structure (e.g., Ross et al., 1999b).

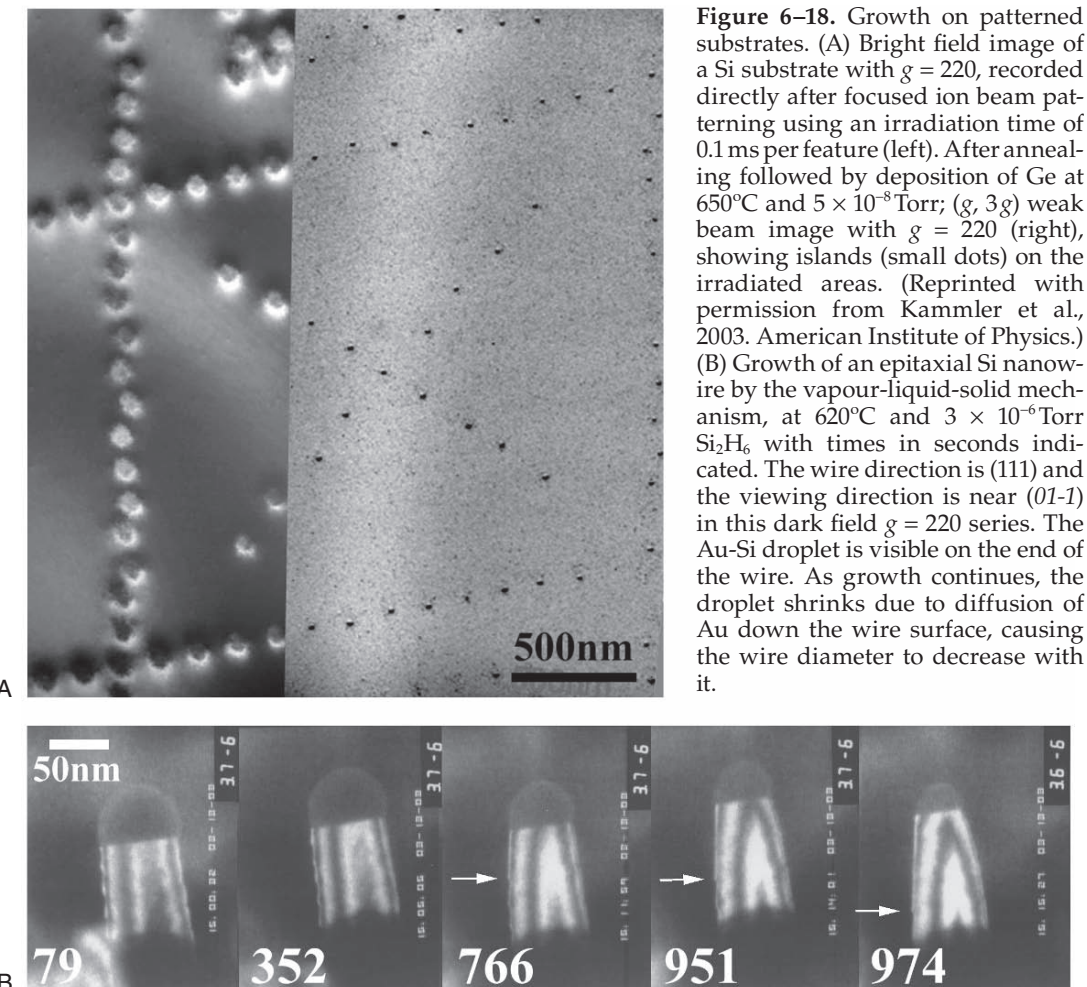
When low Ge content (say 15%) SiGe is grown on Si, islands are not seen, but instead a continuous flat layer forms. When sufficiently thick, this film relaxes by introduction of dislocations. The motion of these dislocations can be measured during film deposition and compared with dislocation dynamics during post-growth annealing, which will be discussed in Section 5. Interestingly, the parameters governing dislocation motion are different during growth, where the surface is H terminated, versus during annealing, where the surface is oxidized (Stach et al., 1998b, 2000). A higher kink nucleation rate under the oxidized surface, perhaps due to surface stress or increased point defects, is the probable cause. This is important for modeling relaxation during device processing, and shows once again the unique information that can be obtained when materials are observed during growth rather than *ex situ*.

3.6 Crystal Growth on Patterned Surfaces

An interesting extension of the growth studies described above is the study of crystal growth on a non-uniform substrate. By carrying out growth on substrates which have been patterned to create areas of different reactivity, strain, or topographic contrast, the effect of these parameters on growth may be visualized directly and even quantitatively, if kinetic data is obtained.

Again, most work has been done in the SiGe system, motivated by an interest in controlling island self-assembly for fabricating novel electronic devices. It is well known that if Ge is deposited on patterned Si, islands form at positions aligned with the topography. *In situ* measurement of nucleation times at different locations (Ross et al., 2004) showed that this is controlled by competition between edge adsorption of adatoms and terrace nucleation. Patterns may also be created with a focused ion beam. At low doses, this forms a shallow topography (Figure 6–18A) that is sufficient to control nucleation and alter wetting layer thickness (Kammler et al., 2003; Portavoce et al., 2006). In these experiments the focused ion beam gun was installed in a chamber connected to the TEM by UHV. The inclusion of surface processing tools that are not *in situ* (i.e., in the polepiece) but are within the microscope's vacuum system enables a wider range of processes to be carried out controllably.

A second example also relates to semiconductor nanostructures: vapor-liquid solid growth of nanowires. Here, a droplet of liquid eutectic catalyzes growth to form elongated wirelike structures. This process has been imaged *in situ* in plan view, allowing wire growth to be observed qualitatively, in Si/Au (Wu and Yang, 2001), Si/Fe (Zhou et al., 2002), and GaN (Stach et al., 2003). In GaAs/Au (Persson et al., 2004), post-growth heating of wires was used to deduce an alternative mechanism, vapor-solid-solid growth. If experiments are performed in



reflection geometry, however, growth kinetics can be measured quantitatively (Figure 6–18B). Such studies demonstrate effects that are not expected from the basic growth model, such as surface faceting (Ross et al., 2005) and catalyst diffusion during growth (Hannon et al., 2006).

3.7 Summary

In this section we have highlighted insights in surface physics and crystal growth derived from *in situ* TEM. Experiments in this field, while often requiring dedicated equipment with complex additional preparation chambers, provide information that is difficult or impossible to obtain using other techniques. Continuous and direct observation *in situ* avoids artifacts arising from *ex situ* observation, which may be especially significant for growth studies. It is particularly encouraging that realistic growth conditions can be accessed in the TEM, enabling *in situ* studies of, for example, catalysis or CVD to be related

to their counterparts in the outside world. Indeed, the relevance of *in situ* TEM to the catalyst and microelectronics industries is shown by the presence of environmental microscopes in several industrial laboratories.

Opportunities clearly exist for further study. Growth on patterned surfaces, prepared if necessary with integrated processing tools in the TEM system, seems a particularly exciting way to examine the fundamental processes controlling growth and to fabricate nanoscale objects with particular properties. Another potentially significant area is the correlation of structural or kinetic *in situ* measurements with macroscopic properties such as stress. Stress may be measured by depositing onto a crystalline membrane whose curvature can be observed. This may provide insight into the important processes associated with coalescence and grain boundary motion during polycrystalline film growth, as well as stress relaxation mechanisms in epitaxial films.

4 Magnetic, Ferroelectric, and Superconducting Materials

It is happily convenient that magnetic and ferroelectric domain walls and magnetic flux vortices can be visualised relatively easily in the TEM using several different imaging modes. This provides us with the opportunity to study the dynamics of ferromagnetic and ferroelectric domain switching, as well as interesting phase transformations associated with magnetic, ferroelectric, and superconducting materials. Holography or Lorentz imaging, either in Fresnel or Foucault mode, can be used to visualise magnetic domain walls and flux vortices, while ferroelectric domains can be observed through their strain field or defect structure. By applying a varying magnetic or electric field to the sample, or by changing its temperature, we can modify its magnetic or ferroelectric structure and correlate the change with the physical microstructure. Such experiments have provided insight into domain boundary dynamics, useful in modeling the workings of storage media or memory elements, as well as providing compelling illustrations of the motion of flux vortices through superconductors.

4.1 Magnetic Domain Motion in Ferromagnetic Materials

The interesting physics and industrially important applications of magnetic materials have generated a strong *in situ* experimental effort in this area. Studies have been motivated by a desire for a basic understanding of magnetic phenomena, as well as by the use of magnetic materials in storage, sensor, and other applications, where the magnetization of small regions of a material has to change controllably and reversibly many times. The most powerful experiments have related *in situ* observation of, say, the micromagnetic changes during a hysteresis cycle to the macroscopic magnetic properties. This allows us to understand, for example, the volume fraction of ferromagnetically or antiferromagnetically coupled regions in a material, or the structural reasons for an imperfect coupling of adjacent layers.

To carry out *in situ* magnetic experiments, two components are required: the ability to apply a controlled field to the specimen, and appropriate imaging capabilities for resolving its magnetic structure. Also useful is the ability to heat or cool the sample so that phenomena can be studied around the Curie temperature.

For applying a controlled magnetic field, it is preferable if the microscope is designed so that the sample sits in a field-free or low-field region. However, if a conventional microscope is used, the objective lens can be switched off, and the magnification this lens usually supplies can be achieved with the other lenses. The controlled magnetic field can then be applied using coils placed in the column or on the specimen holder. Several different designs of specimen holders incorporating coils have been developed to generate in-plane and out of plane fields, preferably without shifting the beam (for recent examples see Uhlig et al., 2003 and Yi et al., 2004). An alternative holder geometry (Park et al., 2005) uses a sharp needle made of a permanent magnet to produce a strong field near the specimen. A simpler solution that does not involve modification of the sample holder is to tilt the sample in an excited objective lens, thereby changing the field it experiences. This has been used to good effect in the experiments on superconductors described in Section 4.2.

Several imaging techniques are available for magnetic structures. These are described in detail elsewhere (Zhu and De Graef, 2001), and include holography, Lorentz imaging in the Fresnel (easier) or Foucault (higher resolution) modes, and the differential phase contrast technique. These techniques have been used extensively to examine static magnetic structures, but here we discuss only experiments where the magnetic structure is deliberately changed. Such experiments have been carried out on single crystals, thin films (often of complex multilayers), and patterned magnetic elements.

4.1.1 Thin Film Magnetic Materials

The motion of domain walls in polycrystalline magnetic materials has been studied for over 30 years to determine how domain walls move in perfect materials, how they interact, and how grain boundaries and other defects alter their motion by pinning. For example, macroscopic hysteresis loops have been correlated with pinning and domain size in Co/Pt (Donnet et al., 1993), and during magnetization reversals in Nd-Fe-B, the grain structure has been shown to affect the mechanism and motion of the domain boundaries (Thompson et al., 1997; Volkov and Zhu, 2000).

Interesting and complex functionalities can be obtained by fabricating multilayered materials where each layer has different magnetic properties. For example, two ferromagnetic materials separated by a conducting layer can show giant magnetoresistance properties which have applications in nonvolatile magnetic random access memory and magnetoresistive read head technologies. When one ferromagnetic layer is “pinned” by an adjacent antiferromagnetic layer, multistep hysteresis loops make the structures suitable for spin valves or spin tunnel junctions. Magnetic tunnel junctions made of two (or more)

magnetic layers separated by an insulating tunnel barrier can also be used for storage or sensing. Details of the magnetization reversal mechanism (for example, whether it occurs by domain nucleation and growth or by spin rotation), and the relationship of the hysteresis loop to the microstructure (interface roughness and grain size) are open questions in these interesting multilayers. For NiFe/Al-oxide/Co and Co/NiFe/Al-oxide/NiFe multilayers, Lorentz imaging in Fresnel mode (Yu et al., 2002a, b) showed the process of magnetization reversal by wall motion and rotation (Figure 6–19), and the relationship of grain size and texture to domain wall motion. Lim et al. (2002, 2004) examined reversal in the complex structures such as PtMn/CoFe/Ru/CoFe/Cu/CoFe/NiFe used in advanced spin valves, while Portier et al. (1999a) studied the effect of heating on Ta/NiFe/Cu/Co/MnFe/Ta films to model thermal damage in spin valves. In IrMn/CoFe films, *in situ* experiments showed that magnetization reversal must overcome two energy barriers, explaining the asymmetry in the reversal behavior and other features of the hysteresis loop, as well as the dependence of the properties on the layer thicknesses (Y.G. Wang et al., 2002). It is clear that *in situ* experiments provide a unique way of studying the properties of the ever more complex multilayers being developed for modern read heads and other applications.

4.1.2 Small Magnetic Elements

Since most applications of magnetic materials require the material to be patterned into small elements, it is naturally useful to examine the behavior of individual elements *in situ*. Typically an electron transparent substrate such as a SiN layer is used, on which magnetic elements of different shapes and sizes are patterned using electron beam lithography. The elements may either be far apart so that they can be studied in isolation, or near their neighbours so that crosstalk can be observed. It is possible to perform micromagnetic simulations of the complete structures, to provide a way to understand the microstructural observations and relate them to macroscopic measurements of hysteresis loops.

A switching experiment carried out on arrays of Co elements is shown in Figure 6–20 (Volkov et al., 2004). Such experiments have allowed the switching field of several materials to be measured (e.g., K.J. Kirk et al., 1999). Permalloy (NiFe) elements have been particularly closely examined (Johnston et al., 1996, McVitie and Chapman, 1997, Schneider et al., 2001, 2002, 2003, X.X. Liu et al., 2004, Lau et al., 2005). These studies showed how the different configurations of remanent magnetization and the process of magnetization reversal depend on the aspect ratio and symmetry of the elements, as well as the temperature, and how the reversal rate of the field affects the final domain configuration. Multilayer elements can also be studied, and by examining spin valve elements, Portier and Petford-Long (2000) showed that certain end shapes allowed easier switching by enabling 360° domain walls to form. Analogous phenomena occur when arrays of holes (antidots) are patterned in an otherwise continuous film. In Permalloy, antidots alter the domain structure and reversal mechanism (Toporov et al., 2000).

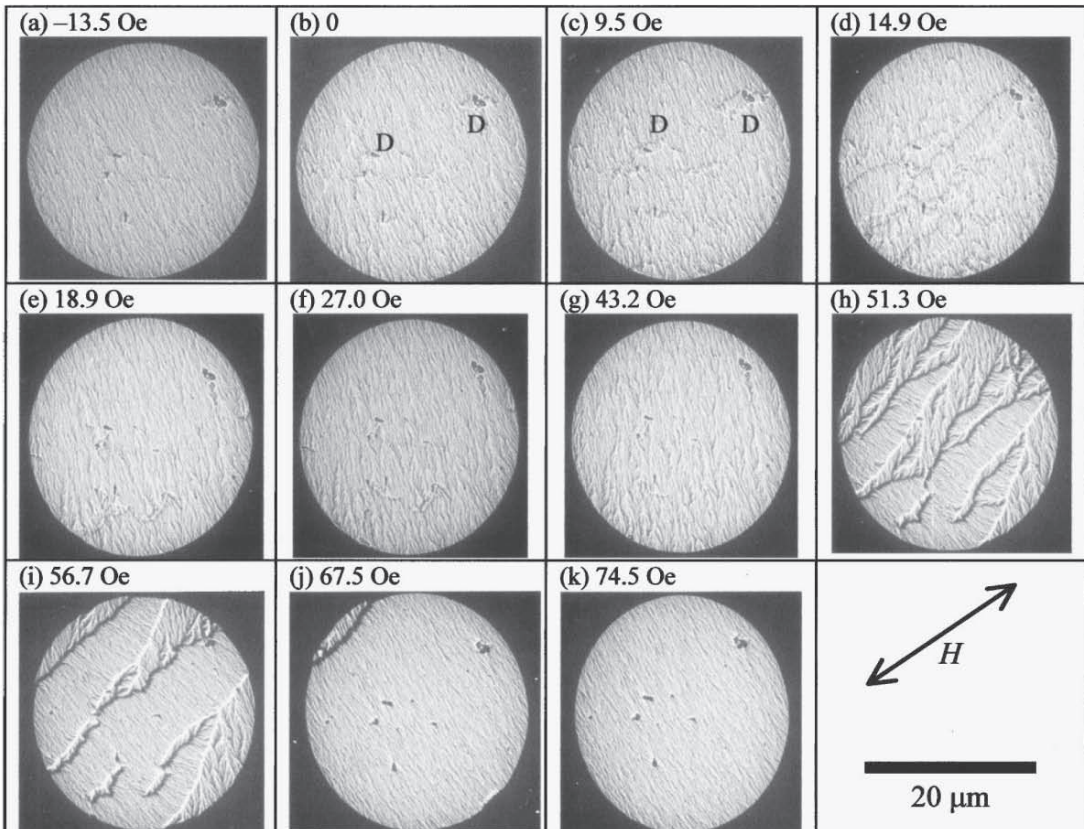


Figure 6-19. Magnetization of a multilayered film *in situ*. Lorentz Fresnel images (a–k) of the magnetization process for an NiFe/Al-oxide/Co junction film. The direction of the applied field H is indicated. All images are of the same area. Also shown is the normalized magnetization vs applied field for the same film. The corresponding domain structure at different field values along the hysteresis loop is shown. (Reprinted with permission from Yu et al., © 2002a. American Institute of Physics.)

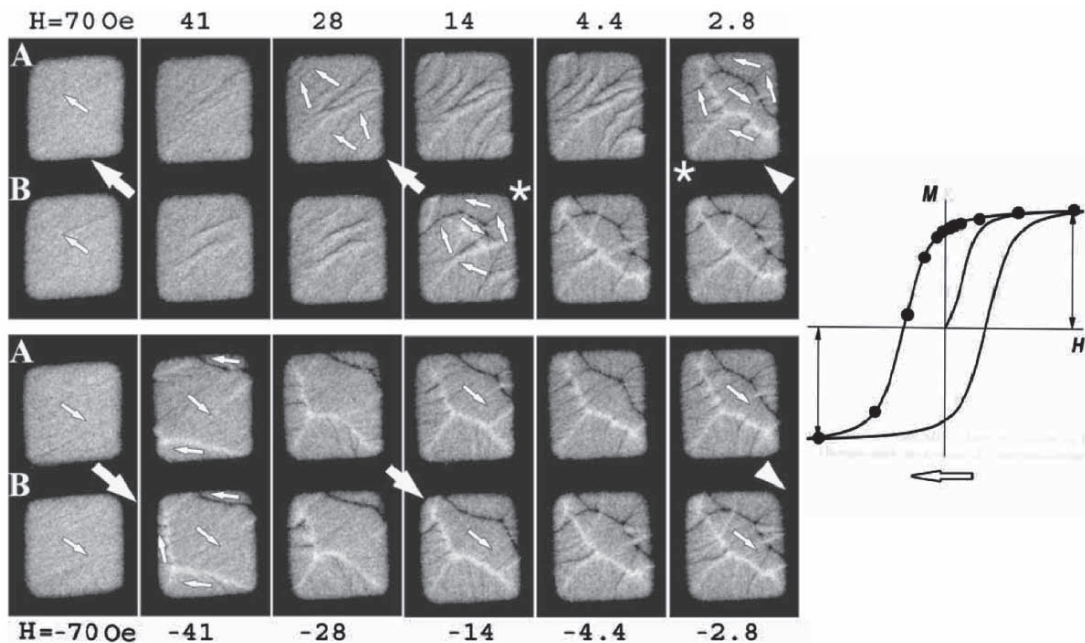


Figure 6–20. Magnetization of small elements. (A, B) *In situ* magnetization of two Co elements 25 nm thick and 6 μ m on a side on an SiN membrane. Images are shown as a function of decreasing applied field, achieved by tilting the sample in a fixed normal field excited by the objective lens (160 Oe), and images are obtained using defocused Fresnel mode. Large and small arrows show the direction of the applied field and local magnetization, respectively. The nucleation of the reverse domain is indicated with asterisks. Only the upper semiloop of the hysteresis curve is shown; the reverse process is somewhat alike but differs in the reverse switching field. The processes observed in these images are coarsening of ripples, due to coherent spin rotation; nucleation and expansion of reverse domains; wall motion and spin rotation in the remaining domains; expulsion of unfavorable boundary domains; and edge annihilation. (From Volkov et al., 2004 with kind permission of Taylor and Francis Ltd.)

An interesting extension of these *in situ* studies on magnetic elements has been the simultaneous measurement of resistivity. Using a holder in which the resistivity of a single lithographically patterned element can be measured while its magnetization is changed, Portier et al. (1997, 1998, 1999b) were able to correlate magnetoresistance with the magnetic domain structure. Studies on single spin valves made of multilayers such as NiFe/Cu/Co/NiFe/MnNi allowed magnetoresistance to be correlated with the angle between the magnetization directions in the ferromagnetic layers. It was also possible to show the mechanism of magnetization reversal, and to demonstrate the effect of stray-field coupling, which introduces edge domains, on the reversal mechanism.

4.1.3 Phase Transitions in Magnetic Materials

The industrial application of materials with giant magnetoresistance has stimulated study of an unusual class of materials which show colossal magnetoresistance. These are certain manganites with the perovskite structure, such as LaSrMnO₃, which have both ferromag-

netic and paramagnetic phases. The phase transition and mixed phase regions in these materials can be studied *in situ* in a cooling stage using electron holography. The nucleation of ferromagnetic domains can be observed on cooling (Yoo et al., 2004a), while in the mixed phase region, application of a magnetic field creates channels connecting ferromagnetic regions, thereby changing the conductivity (Yoo et al., 2004b). These studies help to explain details of the mechanism of colossal magnetoresistance.

Another interesting class of magnetic materials is ferromagnetic shape memory alloys such as Ni₂MnGa and CoNiAl. In these materials, the shape change may be induced by applying a magnetic field. Again, *in situ* TEM using Lorentz imaging and a cooling stage (Murakami et al., 2002, Park et al., 2003) allows the correlation of the magnetic domain structure with the grain structure in these materials. Phase transformations in Ni₂MnGa are shown in Figure 6–21. In experiments like this on bulk materials, the effects of varying sample thickness on domain motion should be considered in order to obtain the most quantitative results.

4.2 Superconducting Materials

In situ TEM has provided a fascinating glimpse into the dynamics of superconducting materials. Over the last several years, several groups, most notably that of Tonomura and coworkers, have observed the presence and dynamics of vortices in superconductors using *in situ* techniques. Single vortices, with their magnetic flux of $h/2e$, have an observable effect on the phase of the imaging electrons. Thus Lorentz microscopy or holographic techniques can be used to determine their positions and characteristics. A medium or high voltage TEM with a cooling stage is used for these studies and the magnetic field can be conveniently applied to the sample by tilting the sample in the existing field of the objective lens.

These experiments have provided unique insights into the behavior of superconducting materials, in particular concerning the formation of vortex lattices, as well as vortex pinning, which must be controlled for practical applications of superconductors. Real time imaging has allowed vortex pinning and dynamics to be related to microstructural features for several superconducting materials (Figure 6–22). The motion of vortices was first imaged in Nb foils below 5K (Figure 6–22A). The effects of grain boundaries on vortex motion were immediately visible (Harada et al., 1992, Bonevich et al., 1993; Tonomura, 2002). The role of dislocations in pinning vortices and nucleating locally ordered regions of vortices (the Abrikosov lattice) was demonstrated (Horiuchi et al., 1998). Nb specimens which had been irradiated with an FIB to produce artificial pinning centers showed fascinating vortex dynamics in which local regions of Abrikosov lattice formed and most motion took place at the boundaries of such lattices (Matsuda et al., 1996). Regular arrays of vortices could be formed with period matching the pinning point period (Harada et al., 1996a). Vortex annihilation was also observed (Harada et al., 1997) and the interactions between vortices

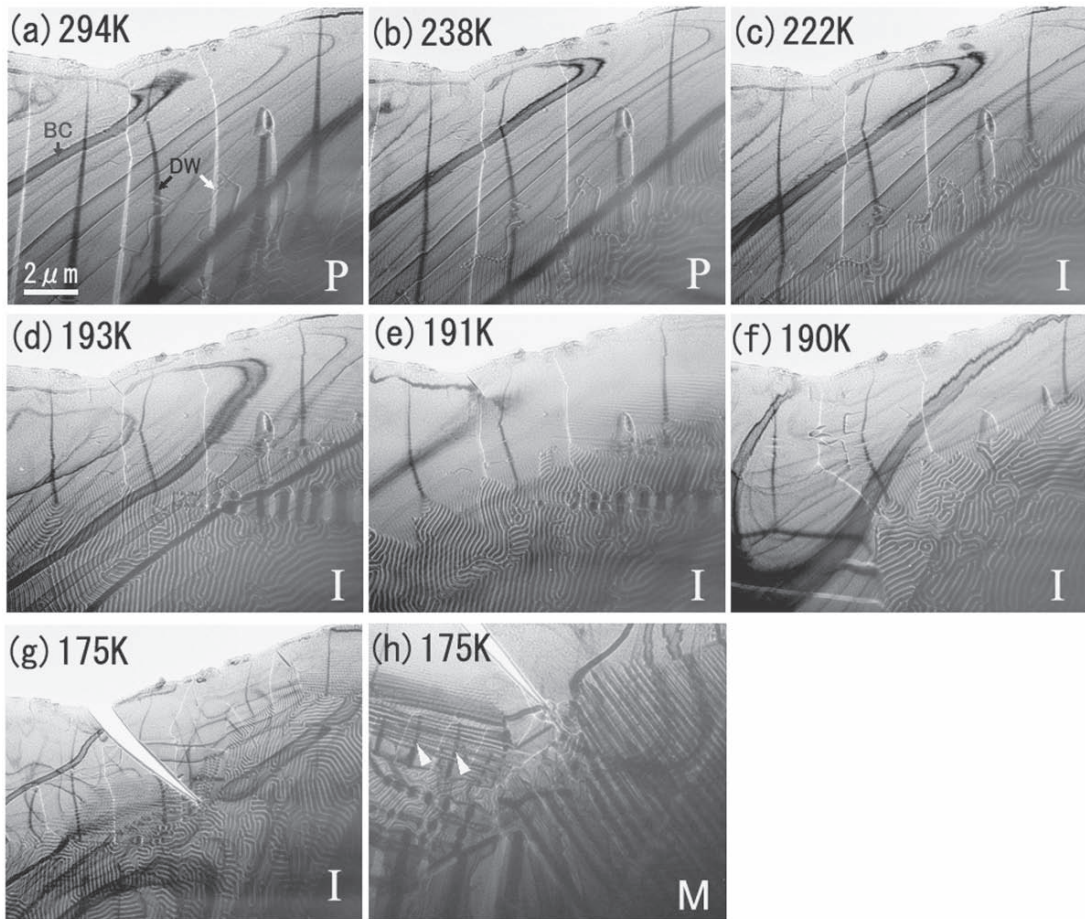


Figure 6-21. Phase transformation in a magnetic material. (a–h) Bright-field images and electron diffraction patterns of the three phases of Ni_2MnGa : the parent phase at 294K, intermediate phase at 207K, and martensite at 170K (P, I, and M, respectively). Both the crystal structure (via diffraction) and the magnetic structure (magnetic domains observed by Lorentz microscopy) are visible. BC and DW represent the bend contours and the domain walls, respectively. (Reprinted with permission from Park et al., © 2003. American Institute of Physics.)

quantified (Sow et al., 1998) by analyzing their motion through the foil. Most recently, asymmetric (one-way) motion of vortices has been controlled by FIB-patterning asymmetric channels (Togawa et al., 2005).

For high temperature superconductors, with their potentially wide range of applications, the pinning of vortices is weak and therefore particularly important to understand and control. Harada et al. (1996b) showed that, in these materials, vortex dynamics also depend on the defects present. The effects of artificial pinning centers are highly temperature dependent, giving useful insight into the different mechanisms active (Tonomura et al., 2001). Furthermore, the vortices adopt unusual chainlike arrangements in these superconductors (Matsuda et al., 2001, Tonomura et al., 2002), as shown in Figure 6-22B. It is worth noting that a high voltage (1 MeV) TEM was required to obtain the necessary resolution for studying these materials (Tonomura, 2003).

4.3 Ferroelectric Phenomena

Ferroelectric domain boundary motion due to an applied electric field or stress has applications in information storage, and the piezoelectric properties of these materials make them interesting as sensors, actuators and transducers. Two key issues in the development of ferroelectric devices are fatigue, in other words the change in boundary dynamics resulting from repeated cycling, and the effects of film thickness and electrode material on boundary dynamics. Polarized optical

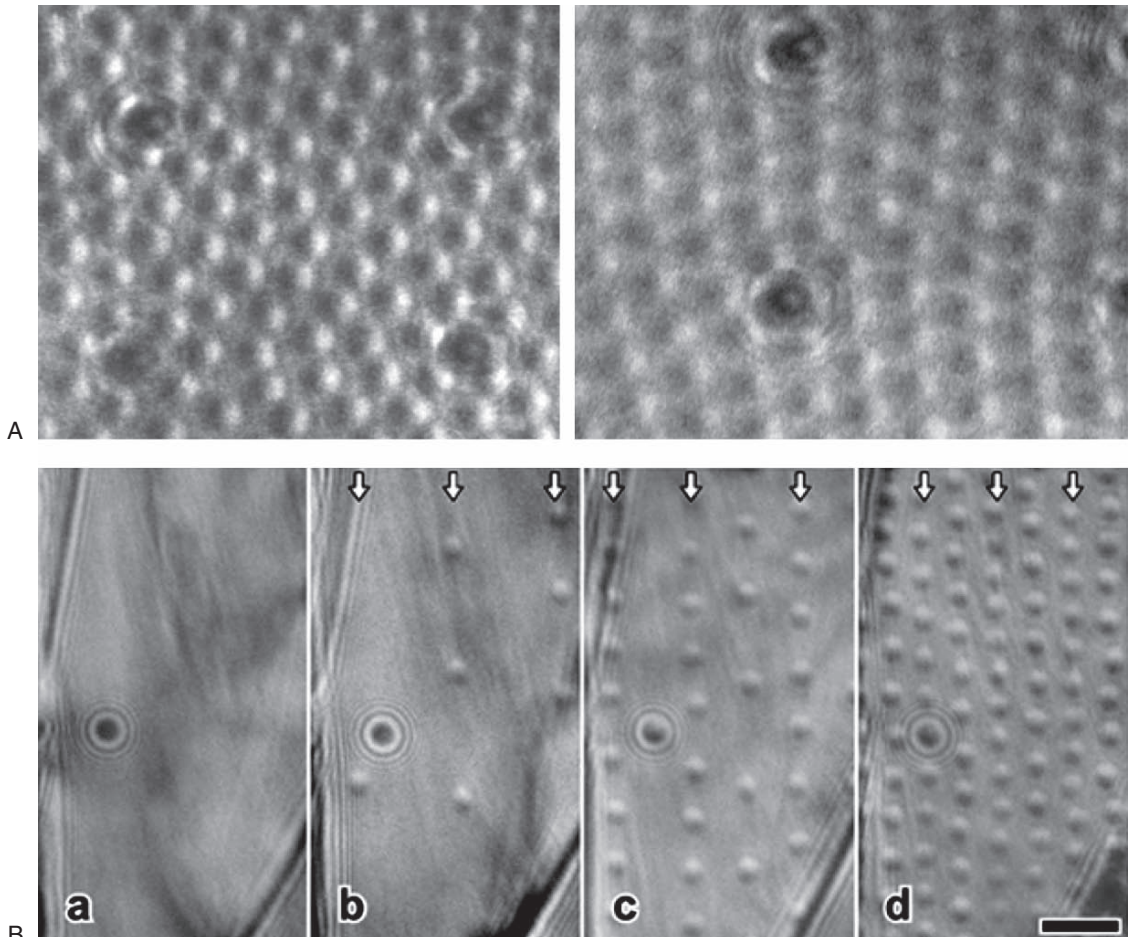


Figure 6–22. Vortex motion in superconductors. (A) Pinning of vortices in Nb. Typical interaction between the vortex lattice and an array of defects produced in an Nb thin foil by irradiation with a Ga+ focused ion beam. In the first image, obtained at 4.5K, the pinning site acts as a domain boundary, while at higher temperatures (8K, lower image) pinning points typically act as cores of edge dislocations in the lattice. (From Harada et al., 1997b with permission from Elsevier.) (B) A series of Lorentz micrographs of vortices in field-cooled Bi-2212 film at 50K when a magnetic field B_z perpendicular to the layer plane is applied. The in-plane magnetic field B_x is fixed at 5 mT. (a) $B_z = 0$ (b) $B_z = 0.02$ mT. (c) $B_z = 0.1$ mT. (d) $B_z = 0.17$ mT. The arrangement of the vertical vortices in chains is marked with arrows. These chains are caused by interactions with horizontal vortices produced by the in-plane field. (Reprinted with permission from Tonomura et al., © 2002 by the American Physical Society.)

microscopy and AFM have been used successfully to investigate the overall features of boundary motion, but naturally TEM is unparalleled in its ability to relate the microstructural features within the material to boundary motion. *In situ* experiments are usually carried out by using a specimen holder with electrical connections to apply an electric field, although domain motion during heating and straining has also been studied. A heating biasing holder is preferable as it allows domain dynamics to be studied at different distances from the transition temperature.

Ferroelectric biasing has been carried out both on mechanically thinned polycrystalline or single crystal samples, and on thin films deposited on a substrate. Depending on the material geometry, the electrical contacts may either both be on top of the sample or one on each surface. As in other experiments, for quantitative analysis a well controlled specimen and field geometry is important. Changes in sample thickness may change the area of domain walls and therefore influence kinetics. Furthermore, as we show below, defects affect wall motion, so the defects introduced during sample preparation must be minimized. For all these reasons, experiments on bulk materials may provide more qualitative information, whereas thin films, especially on substrates which can be made into electron transparent membranes with a controlled electrode geometry and with minimal processing, provide the best opportunity for quantitative results. For example, thin film studies provide the opportunity to understand the “dead layer,” in which surface pinning retards domain motion.

Domain motion has been observed under electron beam heating, for example in $\text{K}(\text{Ta},\text{Nb})\text{O}_3$ (Xu et al., 1993), and during straining, for example in ferroelastic zirconia (Baufeld et al., 1997). Most studies, however, have used *in situ* biasing or controlled heating to achieve domain motion. The most detailed results have come from studies of BaTiO_3 and related materials. For example, Ren et al. (1994) observed domain wall motion in PbTiO_3 , while Snoeck et al. (1994) observed domain growth in BaTiO_3 by tip motion and then by lateral wall motion, and noted defects along the domain boundaries. Krishnan et al. (1999, 2000, 2002; Figure 6-23) observed different modes of domain wall motion in BaTiO_3 and KNbO_3 under heating, biasing, and UV irradiation. These studies showed that the motion of 90° boundaries depends on their curvature and on locking interactions with neighboring domains, and that motion may occur by rippling rather than rigidly. Interestingly, images showed the presence of trapped charge at curved or tilted boundaries or at domain tips. The buildup of charge at boundaries observed *in situ* may be important in fatigue.

In relaxor ferroelectrics such as $\text{Pb}(\text{Mg},\text{Nb})\text{O}_3\text{-PbTiO}_3$, cracking is important in piezoelectric applications. The structures of domain wall intersections has been characterized in these materials (Tan and Shang, 2004a, b; Tan et al., 2005). Cycling the electric field causes cracking in the TEM specimens, thereby providing information on crack propagation pathways along domain walls (Xu et al., 2000; Tan et al., 2000, 2005).

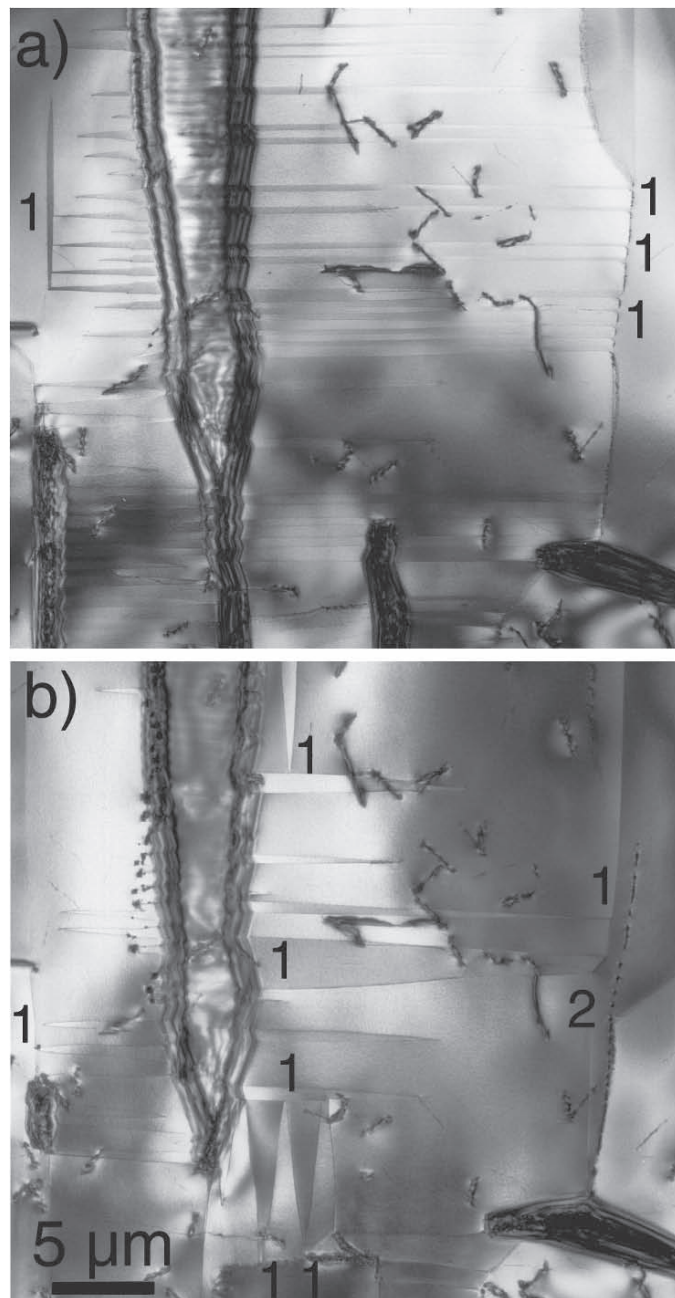


Figure 6–23. Domain wall motion in ferroelectrics under biasing. Bright field images of single crystal KNbO₃ viewed close to the [010] direction. (a) Before applying an E-field. (b) After applying the field. Initially, numerous needle-like 90° domain walls as well as dislocations (dark wiggly features) and other domain wall geometries (vertical stripes) exists. On application of the field, the needle like walls move readily, coarsening the domain structure and forming straighter walls which then move less easily. This is because curved and tilted 90° domain walls (indicated by 1) must support a geometrically required Maxwellian displacement charge hence experience a direct force from an applied field, while charge-neutral domain wall regions (indicated by 2) do not experience a direct force. This suggests an intrinsic mechanism of fatigue. (Reprinted with permission from Krishnan et al., © 2000. American Institute of Physics.)

By analogy with the magnetic phase transitions described in Section 4.1.3, ferroelectric phase transitions may be examined by applying an electric field *in situ*. An example is the electric field-induced transformation of incommensurate modulations in Sn-modified Pb(Zr,Ti)O₃ (He and Tan, 2004, 2005). Other ferroelectric materials, such as Ba₂NaNb₅O₁₅, show interesting incommensurate phases on heating or cooling, and these have been studied *in situ* for several decades. For Ba₂NaNb₅O₁₅, the incommensurate to tetragonal phase transition has been examined in diffraction (Pan et al., 1985; S. Mori et al., 1997). The nucleation of the incommensurate phase can be investigated (Verwerft et al., 1988) as well as the effect of beam-induced defects on the phase transformation (Barre et al., 1991).

We have seen that many ferroelectric phenomena have been examined using electric field and/or hot stage TEM. But it is worth noting that, in comparison with magnetic studies of reversal phenomena, the study of ferroelectric materials has not been as quantitative. As with the magnetic studies, it may be possible to combine simulations with *in situ* studies on patterned ferroelectric elements (Lin et al., 1998), perhaps prepared using focused ion beam processing, to obtain a more detailed understanding of switching and phenomena such as surface effects and fatigue.

4.4 Summary

In situ experiments have provided a persuasive demonstration of the dynamic processes within superconducting, magnetic, and ferroelectric materials: domain motion, flux vortex arrays, and pinning. In the future, where applications of nanostructured ferroelectric and ferrromagnetic materials in storage and microelectronic devices may become even more important, *in situ* techniques are ideally suited to analyze switching and fatigue effects. This will be especially useful in combination with nanoscale patterning to create well-defined geometries. We envisage interesting results if such studies are combined with high speed imaging techniques as well as 3D analysis techniques, such as tomography, for boundary or vortex configurations. However, it is also worth noting that real materials are buried within structures, giving boundary conditions for the electric, magnetic, and strain fields which are different from those found in a TEM foil. Care must be taken that this does not limit the utility of *in situ* TEM. For modeling real life systems, these effects must be included, perhaps by imaging at higher voltage or using tomographic or other analytical techniques to pick out the material of interest from within a complex structure.

5 Elastic and Plastic Deformation

TEM is well suited for studying the mechanical properties of materials. Under appropriate conditions, TEM is very sensitive to lattice distortion, allowing observation of both elastic and plastic deformation via strain fields. *In situ* deformation studies aim to impose a known stress

on a sample and measure the response quantitatively. This may be achieved using a straining stage to pull the specimen uniaxially or biaxially with piezo or mechanical linkages. Alternatively, stress can be imposed by heating samples with a thermal expansion mismatch or an inbuilt stress, such as epitaxial films. Straining can even be carried out in a controlled atmosphere to simulate phenomena such as hydrogen embrittlement. The sample itself may be a thin film, a nanostructure or a bulk material, perhaps notched to initiate cracks. The information from *in situ* experiments is important because deformation is a bulk process and so requires a technique that can see deep into the specimen; surface techniques can not give the whole picture, even if the signature of dislocations can sometimes be seen on the surface. Of course TEM samples are thin in the beam direction so have free surfaces nearby, a factor that must be considered in interpreting results. This can actually be put to good use, though, in studies of tribology or the deformation of individual nanostructures *in situ*.

5.1 Microscopic Phenomena during Deformation of Bulk Materials

Structural changes during deformation, such as grain boundary motion, dislocation motion, and cracking have been studied *in situ* for just about every class of bulk material. These experiments have yielded useful information on dislocation interactions, pinning, the transfer of strain across boundaries, and the effects of temperature. This area has a history going right back to the start of high voltage microscopy, and a review of the first, pioneering work can be found in Butler and Hale (1981). Here we discuss some recent studies on metals, ceramics, semiconductors and alloys. Most experiments require straining stages which are also capable of heating, up to very high temperatures in some cases. Design rules for such extreme heating and straining holders are discussed by Messerschmidt et al. (1998) and Komatsu et al. (1994). Other studies examine the mechanical response of materials to irradiation and will be discussed in Section 8.

5.1.1 Deformation Phenomena in Single Crystals and Polycrystalline Materials

For single crystals, it is possible to relate an applied stress to the motion and interactions of specific types of dislocations. *In situ* observations provide detailed measurements of dislocation generation and multiplication mechanisms, as well as geometry, dissociation, interactions, and slip systems (Figure 6–24A). Studies on polycrystalline materials, on the other hand, allow us to understand the important process of strain transmission across grain boundaries. Heating, straining, and heating/straining experiments have been the focus of several groups, and comprehensive reviews are available (Messerschmidt et al., 1997; Mori, 1998; Pettinari et al., 2001; Vanderschaeve et al., 2001; Messerschmidt, 2003).

We first consider metals and alloys. Dislocation motion has been studied in single crystals such as Mg, Cu, and Al at moderate temperature, while refractory metals require high temperatures (Mori, 1998).

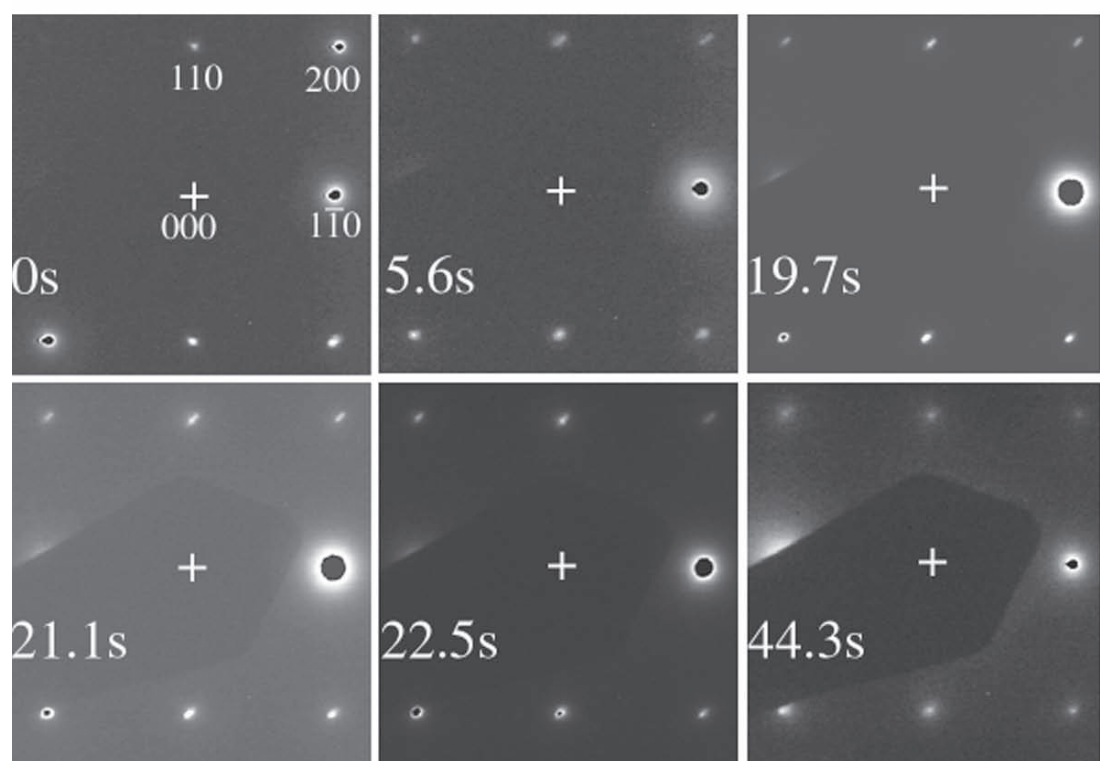
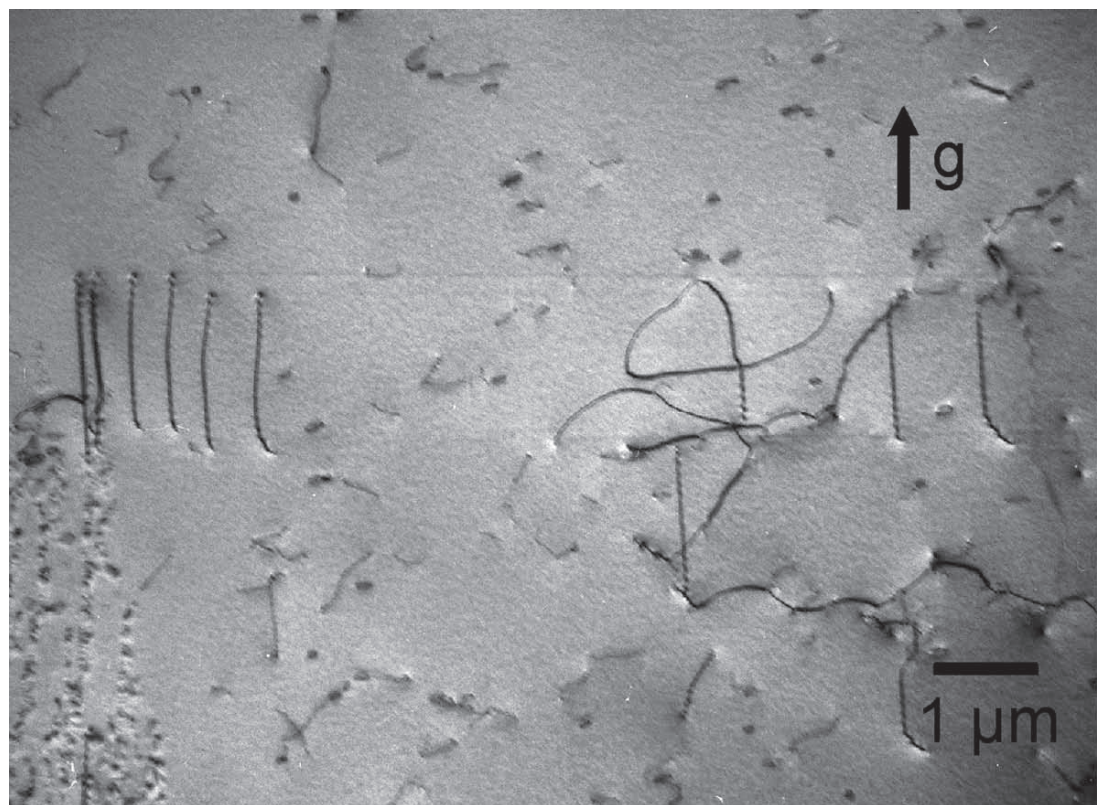


Figure 6–24. Deformation of bulk crystals. (A) Dislocations moving away from a localized source during *in situ* deformation of a MoSi₂ single crystal at ~900°C. The loading axis is [201], which is a soft orientation, and dislocations of Burgers vectors 1/2 <111> are activated on {110} planes. The traces of these slip planes run horizontally. Owing to the generation of these dislocations in localized sources, as shown here, planar slip dominates. The foil plane is (010) and $g = [220]$. (From Messerschmidt et al., © 1998. Courtesy of Cambridge University Press.) (B) Deformation of a refractory metal, V, without formation of dislocations. Diffraction patterns are obtained near the crack tip during deformation of a notched foil. As the internal stresses increase, the spots expand perpendicularly to the crack so appear elongated. (The central spot is masked to prevent overexposure.) Images do not show clusters of point defects in V, unlike the case of Au strained under the same conditions. (From Komatsu et al., 2003 with permission from Elsevier.)



Most studies apply a uniaxial stress, although, for example, cyclic shearing of Al single crystals has been described (Kassner et al., 1997). Plastic deformation does not always require dislocation generation or motion, and in V, Mo, and other bcc metals, deformation may occur by formation of point defects rather than dislocations. This too can be observed *in situ* with appropriate diffraction and imaging techniques (Komatsu et al., 2003; Figure 6–24B). The challenge in all these straining experiments is to make them quantitative. One interesting technique for the measurement of local stress is through the curvature of dislocations between pinning points (Pettinari et al., 2001).

As an intermediate case between single crystal and polycrystalline metals, bicrystals provide the opportunity to apply the precision of single crystal experiments to studies of strain transfer across boundaries. For example, in symmetric Σ 3 Fe-4 at.% Si bicrystals, Gemperlova et al. (2002) determined the primary slip system and studied the particular slip systems which can transmit stress across the boundary.

For polycrystalline metals, deformation can be investigated for thin films by either straining or heating. TEM is well suited to these thin film studies, although the sample geometry must still be controlled (for example with respect to thickness uniformity) to avoid artifacts, and surface passivation can affect the results. Straining experiments have shown, for example, that the failure mode of polycrystalline Ni films depends on grain boundary structure (Hugo et al., 2003). Thermal cycling experiments show grain boundary motion (see Section 2.1.3) and the interactions of dislocations with grain boundaries and precipitates (e.g., Kaouache et al., 2003). For thin Cu and Al films, the higher yield stress known for these materials has been related to particular types of dislocation motion (Dehm and Arzt, 2000; Balk et al., 2003). Threading dislocation motion and the effect of the passivation layer have also been studied (Keller-Flaig et al., 1999; Legros et al., 2002). Recent progress with nanoindentation stages (Section 5.3.1) and the development of specimens incorporating microelectromechanical (MEMS) free-standing films (Section 5.1.2) promise further developments in understanding the deformation of polycrystalline films in the future.

We now consider intermetallics, which have been examined *in situ* to understand the mechanism of their high temperature toughness and phase transformations. Generally, dislocation dynamics change as a

function of temperature in these materials (e.g., Haussler et al., 1999). Dislocation interactions, cross slip, and nucleation of loops control work hardening, ductility, and the critical resolved shear stress (Legros et al., 1996, 1997; Legros and Caillard, 2001). Dislocation motion during creep has also been examined (Malaplate et al., 2004).

Polysynthetically twinned TiAl crystals have lamellar structures with well-defined boundaries. By analogy with the bicrystal experiments, strain propagation across these boundaries can be quantified *in situ* (Zghal et al., 2001; Pyo and Kim, 2005). Transformations in shape memory alloys have already been mentioned in Section 2, and *in situ* straining experiments relate the microstructural changes during deformation to the stress-strain response (Jiang et al., 1997; Dutkiewicz et al., 1995; Gao et al., 1996). The cracking of intermetallics is also important in applications. Dislocations emitted at a crack tip can be analyzed (in NiAl; Caillard et al., 1999), and amorphization can be detected at crack tips (in NiTi ordered alloys; Watanabe et al., 2002).

Quasicrystals have interesting mechanical properties and dislocation geometry. *In situ* heating and straining experiments have led to the identification of shear systems and models for dislocation motion in these materials (Messerschmidt et al., 1999; Messerschmidt, 2001; Caillard et al., 2002; Mompiou et al., 2004; Bartsch et al., 2005).

Ceramics have been important subjects of study since the 1970s, with an interest in comparing dislocation motion at lower and higher temperatures (e.g., in zirconia, Messerschmidt et al., 1997; alumina, Komatsu et al., 1994; MoSi₂, Guder et al., 2002). In quartz, strain-induced phase transformations have been studied by combined straining/heating experiments (Snoeck and Roucau, 1992).

We finally consider semiconductors. Kinetic studies show that dislocation motion is consistent with glide governed by the Peierls mechanism (Vanderschaeve et al., 2001). From dislocation motion and pinning, the kink mean free path and formation and migration energies can be determined (Gottschalk et al., 1993; Vanderschaeve et al., 2000; Kruml et al., 2002). Radiation enhances the glide of dislocations by changing some of these parameters (Section 8). Most studies have used low resolution, dark field imaging to record dislocation motion, but it is actually possible to observe directly the thermal motion of kinks in Si using a high resolution forbidden reflection imaging technique (Kolar et al., 1996). This generates fascinating information. The kink formation energy and unpinning barrier can be derived from the distribution and pinning of individual kinks, and videos show directly that kink migration is the rate limiting step in dislocation motion. This technique should be applicable to other materials and is expected to lead to further advances in our understanding of dislocation motion (Spence et al., 2006).

5.1.2 Deformation of Multiphase, Composite, or Layered Materials

Deformation experiments in multiphase materials, such as dispersion strengthened alloys, are particularly important in materials development, since they show how strain is transmitted between components. Dispersion strengthened Al alloys have been examined extensively, to

characterize the nucleation of dislocations at precipitates and their motion past precipitates (Vetrano et al., 1997; Hattenhauer, 1994). These phenomena are critical in high temperature deformation of such alloys. Other phenomena, such as grain boundary migration, coalescence, and elimination of subboundaries, occur during dynamic continuous crystallization on loading in the TEM (Vetrano et al., 1995; Dougherty et al., 2003), with *in situ* studies helping to understand the processes. Steel

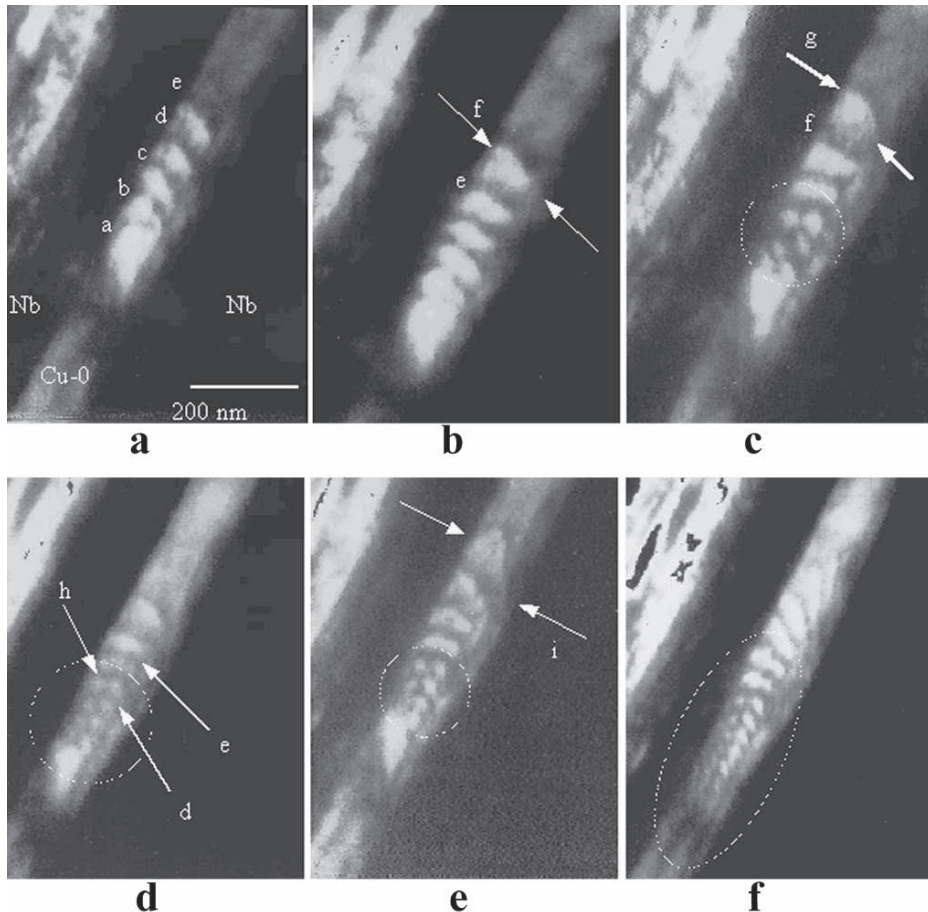


Figure 6–25. Deformation in a Cu–Nb multifilamentary composite. Nanocomposite materials are used in wires requiring high strength and high conductivity. This sample was prepared by cold drawing an Nb rod inside a Cu jacket several times until a composite was formed consisting of Cu–17%vol–Nb with 10^7 Nb filaments 40 nm across in Cu. The Cu channels have <111> texture, the Nb filaments have <110> texture, and the Cu–Nb interfaces are semicoherent. The sequence of images shows the introduction of dislocations under an applied force of 8 N. At this point Cu is plastically deformed while Nb is still elastically deforming. The area shown is a Cu channel of width about 100 nm (white) between two Nb filaments (black). At the beginning of the sequence (image a), five dislocation loops are present on parallel planes. A few seconds later the sixth and seventh loops appear (images b and c). By the end of the sequence 13 loops are present, and they have interacted to produce a honeycomb pattern (circles in images c–f). This dislocation behavior is used in a plastic flow model, which explains the very high ultimate tensile stress of fcc–bcc nanocomposite structures. (From Thilly et al., 2002, with kind permission of Taylor and Francis Ltd.)

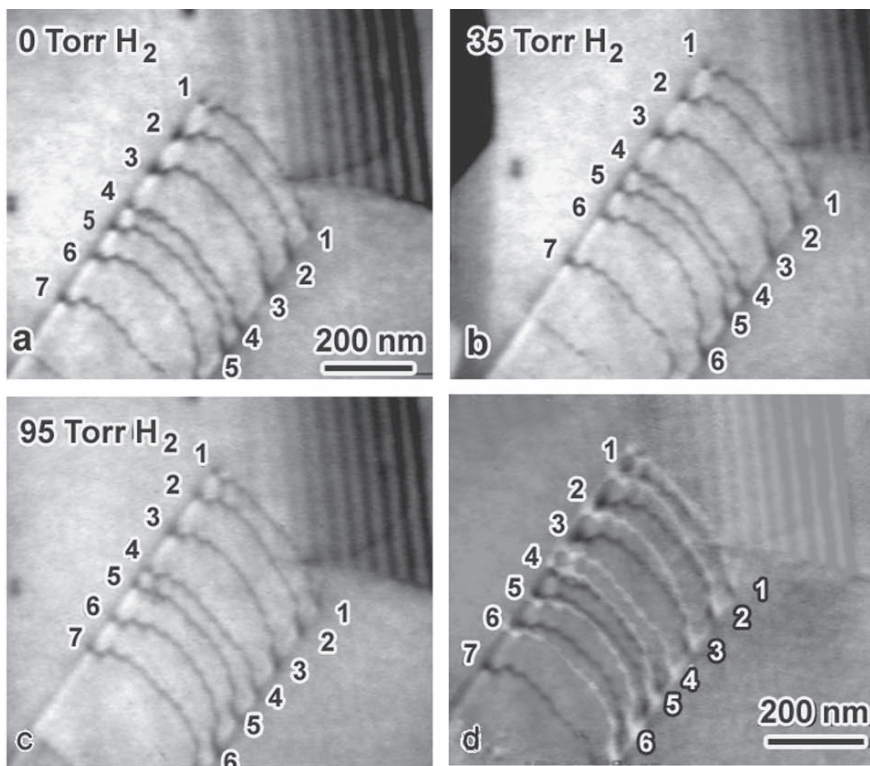


Figure 6–26. Dislocation motion in H atmosphere. Showing the effect of H on the mobility of dislocations in 310S stainless steel. (a) dislocation configuration in vacuum under constant load; (b) 35 Torr; (c) 90 Torr of hydrogen; (d) composite image formed by subtracting (c) from (a). (Reprinted with permission from Robertson and Teter, © 1998 by the American Physical Society.)

is of course another multiphase material whose behavior *in situ* has been studied for some time (Caillard et al., 1980); industrially relevant studies of dislocation motion and slip transmission through interfaces in steels continue (Verhaeghe et al., 1997; Janecek et al., 2000; Zielinski et al., 2003). Many other nanocomposite materials provide interesting examples of dislocation-interface interactions. One such is shown in Figure 6–26 (Thilly et al., 2002) and other work is reviewed by Louchet et al. (2001).

Techniques developed for multiphase materials extend easily to engineered multilayers, where the interaction of dislocations or cracks with interfaces is of interest. Cross sections of multilayers may be prepared using a FIB to form a thin section at which cracks will initiate (Wall et al., 1995; Wall and Barbee, 1997). Alternatively, multilayers (or thin films) may be integrated into a mechanical testing stage. One example is a piezo stage for cyclic loading of solder thin films, used to show that cavitation is the dominant fatigue damage mechanism (Tan et al., 2002). In this stage, a multilayered structure is fabricated which includes the material of interest as well as a piezoelectric layer.

The future for thin film and multilayer studies undoubtedly lies in extending this sort of approach, achieving controlled deformation using MEMS-based techniques. MEMS force sensors and displacement

measurement systems can be integrated with the film of interest, allowing for quantitative experiments. Stages for uniaxial tensile testing of free-standing thin films have already been demonstrated (Haque and Saif, 2003, 2004, 2005; Hattar et al., 2005), with initial results on polycrystalline Al thin films, and other functionalities such as heating are under development (Zhang et al., 2005). We anticipate further exciting progress in this area.

5.1.3 Deformation in a Controlled Atmosphere

By combining mechanical testing with controlled environment TEM, a very important objective, understanding the mechanism of hydrogen embrittlement of steels, has been achieved (Figure 6–27). *In situ* straining experiments carried out in an environmental cell showed that solute hydrogen can increase the speed at which dislocations move through the material, as well as increasing the rate of crack propagation (Robertson and Teter, 1998; Teter et al., 2001; Sofronis and Robertson, 2002). By quantitatively analyzing dislocation dynamics on adding and removing hydrogen, competing mechanisms for embrittlement could be distinguished. The hydrogen shielding model was confirmed, in which the hydrogen-enhanced localized plasticity mechanism is the shielding of the dislocation from interactions with other strain centers such as pinning points, other dislocations, or solutes. Few other materials have been strained in a controlled atmosphere, although Maeda et al. (2000) showed that the incorporation of hydrogen from a plasma increases the motion of dislocations in semiconductors. Further studies could provide a sensitive probe of dislocation properties and interactions.

5.2 Relaxation of Epitaxially Strained Materials

In this section, we consider another method of straining a material: growth of the material epitaxially on a lattice mismatched substrate. As the layer is deposited a high intrinsic stress builds up, and, once above a “critical thickness,” the layer may relax by forming a network of dislocations at the layer-substrate interface (Figure 6–27A, B). This phenomenon can be examined *in situ*. First, a layer thicker than the critical thickness is grown, but at a temperature that is too low to allow dislocation nucleation or propagation. Then a plan view TEM specimen is prepared and heated *in situ*, allowing relaxation to be observed as a function of temperature. The advantage of this type of experiment is that the stress state is very well defined, making this a situation where dislocation dynamics can be measured quantitatively. Such studies are motivated by their importance to the microelectronics industry, since the positions of individual dislocations, the density of threading arms, and the motion of dislocations during processing are known to affect device performance.

This work was carried out for the system $\text{Si}_{1-x}\text{Ge}_x$ on Si, with x ranging from about 0.05 to 0.3 (Hull et al., 1989, 1991). Measurements of dislocation velocity as a function of layer parameters are shown in Figure 6–27C. For capped layers, the results supported the diffusive kink pair model of dislocation propagation, and for uncapped layers they showed that propagation is through motion of single kinks.

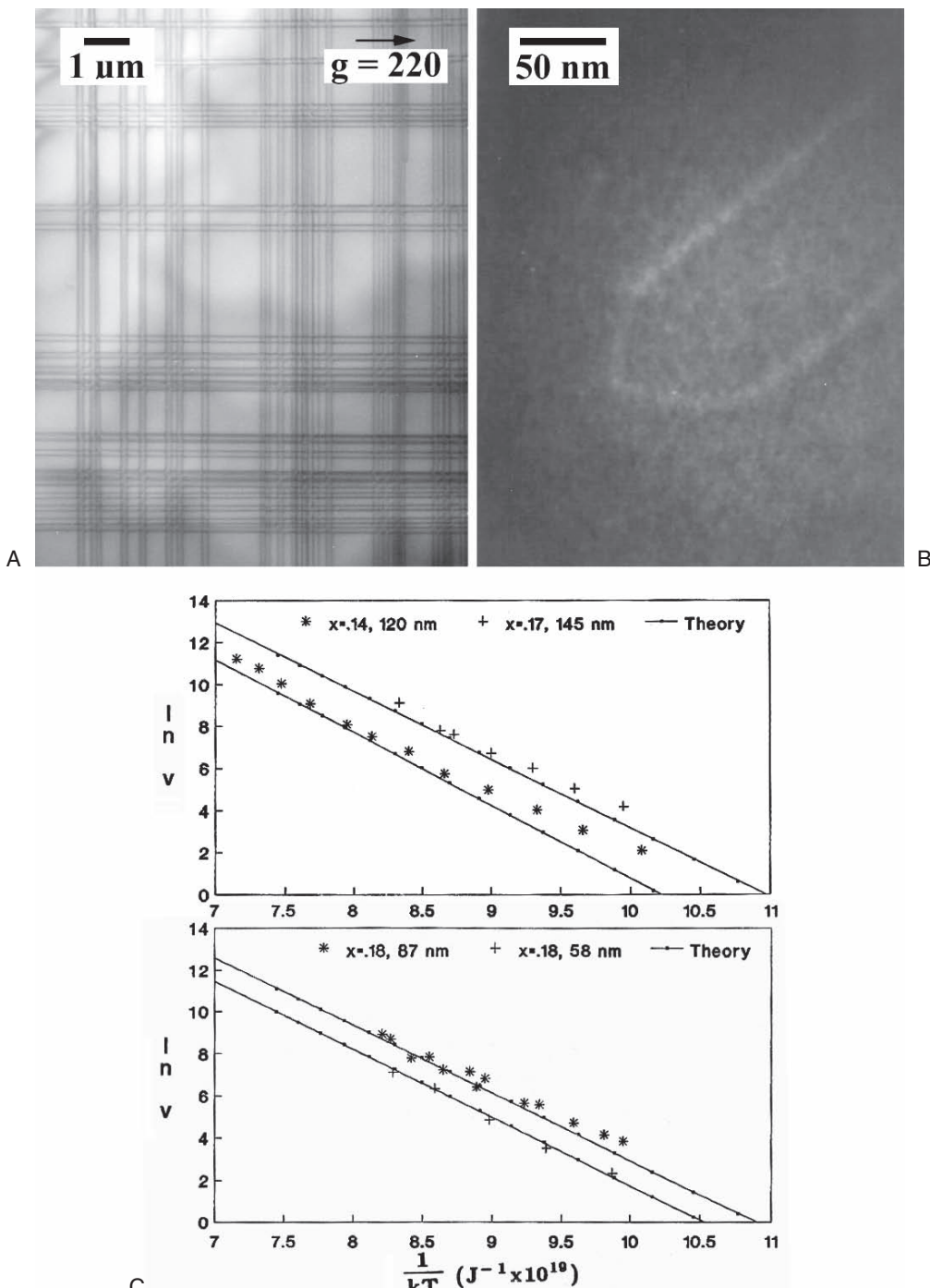


Figure 6-27. Dislocation dynamics in SiGe heterostructures. (A) Image showing the typical dislocation structure in SiGe heterostructures. Plan-view TEM image of a relaxed 300 nm Si/150 nm $\text{Si}_{80}\text{Ge}_{20}/\text{Si}(001)$ heterostructure. Closely spaced interfacial dislocation pairs are segments of the same dislocation loop at the top and bottom SiGe/Si interfaces. (From Stach et al., © 1998b Courtesy of Cambridge University Press.) (B) $220g, 3g$ weak-beam dark-field micrograph of a threading dislocation segment connecting two interfacial dislocation segments. (From Stach et al., 1998b.) (C) Measured dislocation velocities compared with predictions of the double-kink theory for SiGe layers buried beneath a 300 nm Si cap, as in (A). The Ge concentrations, x , and epilayer thicknesses are given on the graphs while the dislocation velocities are given in Angstrom s^{-1} . The fitting parameter used in the model is half the double-kink nucleation energy, taken as 1.0 eV. (Reprinted with permission from Hull et al., 1991. American Institute of Physics.)

Activation energies and prefactors were measured for dislocation nucleation and propagation. Note that a well calibrated system is necessary if TEM-derived parameters such as activation energy are to be meaningful. In this case, the sample temperature was calibrated using Si regrowth (Section 2.1.1), and finite element analysis was used to determine the conditions under which sample bending could be neglected (Hull and Bean, 1994). The parameters determined *in situ* were eventually used in a processing model for microelectronic device design (Hull et al., 1989).

A similar experimental approach allows other features of the relaxation process to be examined as well. Dislocation nucleation has been studied in SiGe/Si implanted with F (Stach et al., 1998a) and with He, which forms platelets and bubbles (Follstaedt et al., 1997; Hueging et al., 2005). Although most work has been in the SiGe/Si system, a few other epitaxial systems have been studied as well, such as BaTiO₃ on SrTiO₃ (Sun et al., 2004), ZnSe on GaAs (Lavagne et al., 2001), and Al on Al₂O₃ (Dehm et al., 2002). Clearly, many other materials systems could yield useful information with this technique.

We finally note that dislocation configurations in thin films, such as in Figure 6–27A, are somewhat random. However, in well controlled geometries—relaxed epitaxial islands, or surfaces with modulated stress fields—dislocation locations can be predicted accurately (Liu et al., 2000; Kammler et al., 2005). This suggests opportunities for *in situ* TEM to provide quantitative information on dislocation nucleation and growth in finite nanostructures with built in strain, such as epitaxial islands or composite wires or ribbons.

5.3 Mechanical Properties of Nanostructures, Thin Films, and Surfaces

TEM is particularly appropriate for studying the mechanical properties of small volumes of material. In the work discussed so far, the same stimulus (strain, heat) is applied to the entire specimen. By applying the stimulus to only a small part of the specimen, the correlation between mechanical input and structural response can hopefully be made more precise. In this section we discuss experiments in which small volumes of a specimen are mechanically deformed (nanoindentation), the surface is probed, or nanostructures are deformed. These experiments make use of scanning probe techniques to bring a tip near the sample for controlled deformation of an area under observation.

5.3.1 In Situ Indentation of Thin Films

By integrating a nanoindenter into a specimen holder, it is possible to examine localized deformation of single crystals, polycrystalline materials, and layered structures. Nanoindentation holders have been described by Wall and Dahmen (1998), Stach et al. (2001), Minor et al. (2001), Bobji et al. (2003) and Ii et al. (2004). The design must include some way of making sure the indent occurs in an electron transparent region of the specimen. In the design of Wall and Dahmen, for example, a Si sample (mounted vertically) is etched to form a ridge which projects out into the beam. Elastic deformation followed by dislocation

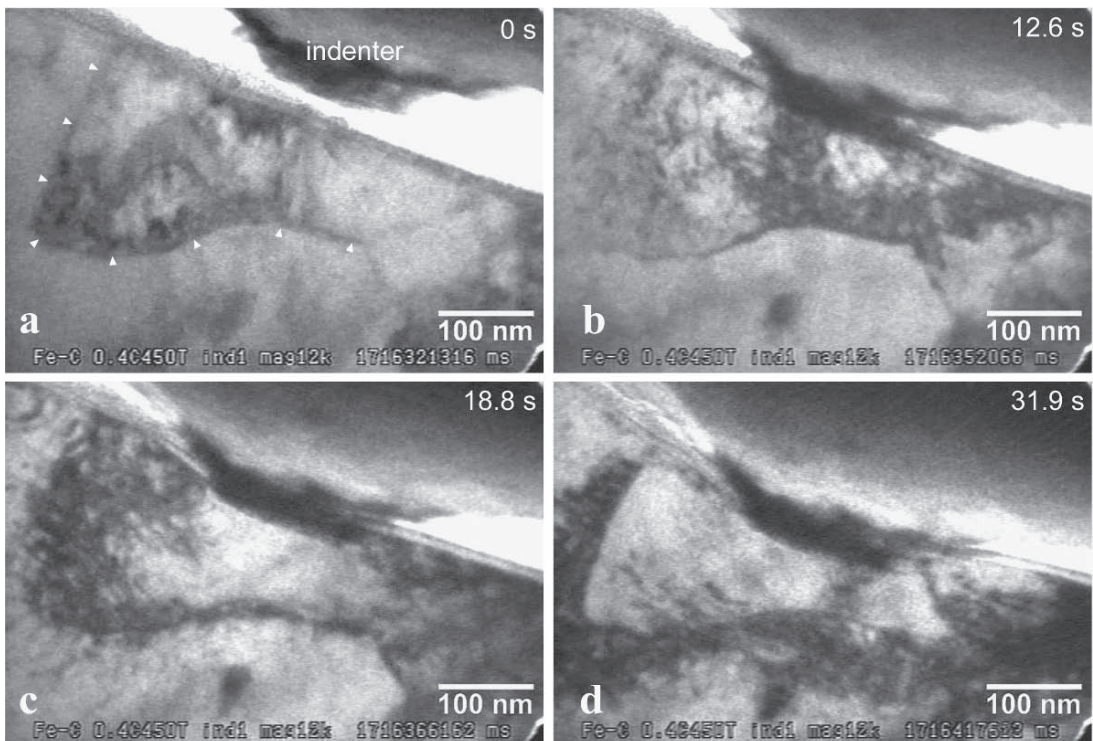


Figure 6-28. Nanoindentation of steel. Series of images of an Fe-C martensite, including a low-angle grain boundary. (a) Before indentation, (b) at 21 nm penetration depth, showing dislocation emission beneath the indenter, (c) at 46 nm penetration depth, showing dislocation pileup at the grain boundary, and (d) at 84 nm penetration depth, demonstrating dislocation emission at the far side of the grain boundary. (From Ohmura et al., ©2004. Courtesy of Institute of Materials Research Society.)

formation is visible in this ridge during indentation. Using this sample geometry, the motion of dislocations and grain boundaries under the indenter tip has been studied in a variety of materials deposited onto the substrate. In ultra fine grained Al, for example, grain boundary motion occurs under the tip (Jin et al., 2004). This does not occur in Al-Mg, suggesting that solute drag is important (Soer et al., 2004). Similarly, in Ni, deformation proceeds by diffusion-controlled grain boundary-mediated processes rather than dislocation motion within grains (Shan et al., 2004). Si shows dislocation plasticity on room temperature nanoindentation (Minor et al., 2005). Nanoindentation of martensitic steel is shown in Figure 6-28 (Ohmura et al., 2004), and the formation of dislocations and the strain transfer across grain boundaries are visible. As well as dislocation formation and motion, nanoindentation can cause crack propagation. The nature and pathway for such cracks can be determined (Ii et al., 2004; Matsunaga et al., 2004). In the future, we expect to see exciting developments in the area of *in situ* nanoindentation, driven by the incorporation of sensors that allow stress-strain curves to be measured during deformation. This suggests exciting possibilities for quantitative analysis of nanoscale mechanical properties.

5.3.2 Tribology and Nanomanipulation

Nanoindentation is only one of several interesting experiments that can be carried out in holders incorporating a scanning tip with piezoelectric actuators. For example, the tip can be used for fundamental studies of tribology by scraping it across a surface. Tip-substrate interactions were observed in reflection mode geometry as a graphite specimen was imaged using STM (Spence et al., 1990; Lo and Spence, 1992), and changes in the surface were attributed to shearing and abrasion. Using a similar holder in a UHV TEM, Naitoh et al. (2000) correlated the atomic configuration at a tip surface with the resolution of STM images it produced. Fujisawa and Kizuka (2003a) and Ohnishi et al. (1998a) observed the motion of a tip across a stepped surface and determined the effects of rastering and surface topography on lateral displacement. This sort of information is naturally important in interpreting scanning probe images.

Alternatively, an *in situ* STM tip can be used to form small necks or grain boundaries by touching it to the surface, deforming both materials (Figure 6–29). The structure of these necks can then be observed at

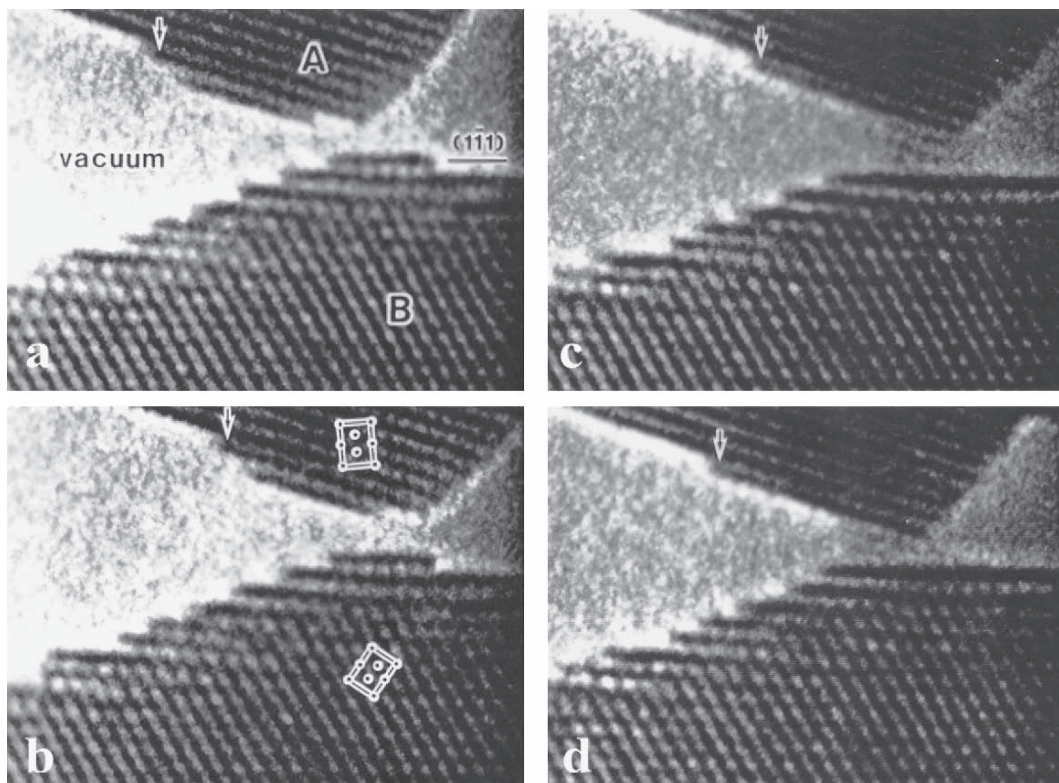


Figure 6–29. STM surface manipulation. Series of high-resolution images of atomic-scale removal type mechanical processing of an Au surface. A region six atomic columns wide on the fixed side (B) is removed by the Au tip on the mobile side (A). On both sides the beam is parallel to the [110] axis. The time is (a) 0 s, (b) 1.2 s, (c) 3.5 s, and (d) 5.8 s. Boxed circles show the unit cell of Au. These images give a visual impression of events that may occur during STM operation as well as phenomena associated with friction. (From Kizuka et al., © 1998c. Courtesy of Cambridge University Press.)

high resolution. Kizuka and Hosoki (1999) recorded the interactions as two oxidized Si tips came into contact, observing the strength of the boundaries formed, and Naitoh et al. (2000) observed twins in necks of Si formed between clean Si and a W tip. Most work, however, has involved Au. Kizuka (1998a, b) showed formation of a neck between Au contacts and observed compression, shear, deformation, slip, and twinning. These videos give a stunning visual impression of the interaction of the tip with a surface during scanning, and allow a study of friction at the nanoscale (Fujisawa and Kizuka, 2003b). Naturally, the electrical properties of such necks can also be studied, and this will be described in Section 6.

5.3.3 Mechanical Properties of Nanostructures

The mechanical properties of elongated nanostructures are a natural subject for *in situ* studies. For carbon nanotubes, mechanical parameters such as Young's modulus were first measured by observing the vibration of tubes which extend out as cantilevers (Krishnan et al., 1998). These tubes vibrate because of coupling to motion in the stage. However, the mechanical properties of tubes can also be measured by bending them with an STM tip. Individual CNTs can be bent and broken (Kuzumaki et al., 2001) and stress and strain can be measured during deformation (Asaka and Kizuka, 2005). The welding of CNTs to a tip can be seen (Hirayama et al., 2001; Kuzumaki et al., 2004). A tip can even be used to operate a bearing made of telescoping CNTs (Cumings and Zettl, 2000; Figure 6–30). Such experiments can use the

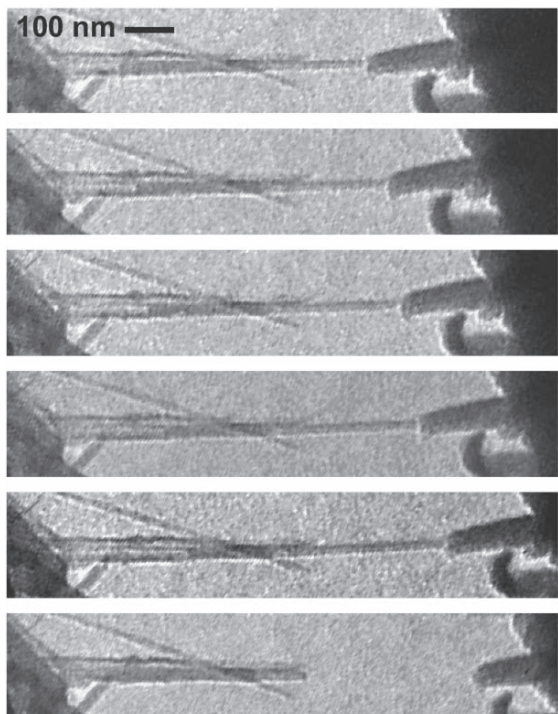


Figure 6–30. Mechanical properties of a carbon nanotube. Selected frames of a video recording of the *in situ* telescoping of a multi-walled nanotube. In the first five frames, the core nanotubes are slowly withdrawn to the right. In the sixth image, which occurred one video frame after the core was released, the core has fully retracted into the outer nanotube housing as a result of the attractive van der Waals force. (Reprinted with permission from Cumings and Zettl, © 2000, AAAS.)

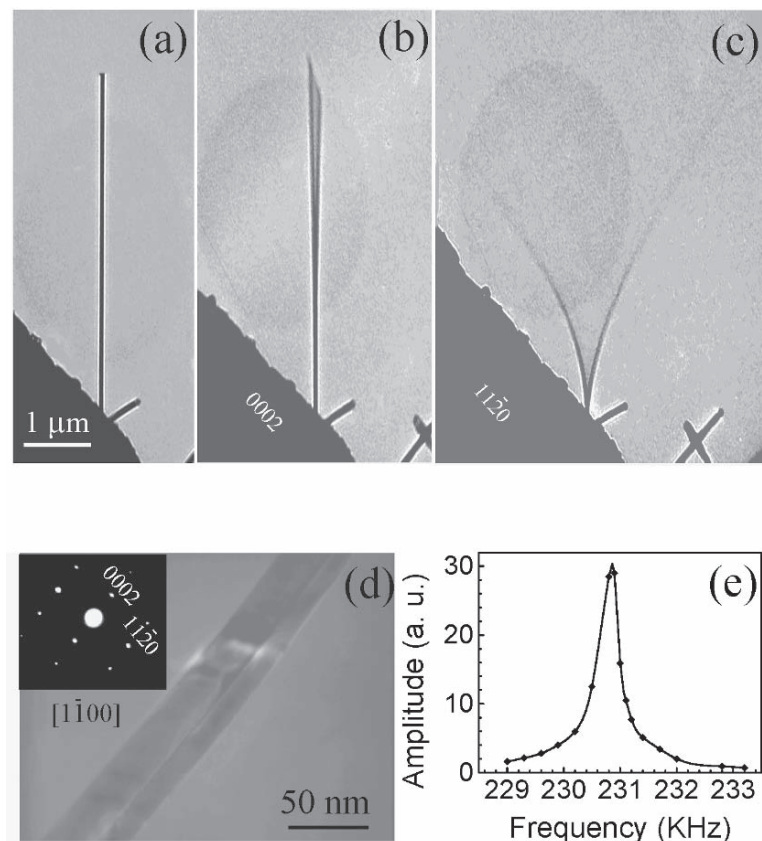


Figure 6–31. Mechanical properties of a nanobelt. A ZnO nanobelt at (a) stationary, (b) the first-harmonic resonance in the x direction, frequency 622 kHz, and (c) the first-harmonic resonance in the y direction, frequency 691 kHz. (d) An enlarged image of the nanobelt and its electron diffraction pattern (inset). The projected shape of the nanobelt is apparent. (e) The FWHM of the resonance peak measured from another ZnO nanobelt. The resonance occurs at 230.9 kHz. (Reprinted with permission from Bai et al., © 2003. American Institute of Physics.)

TEM for more than just imaging; for example, Suenaga et al. (2001) were able, using EELS, to probe changes in electronic structure during bending of multiwalled and bundled single walled CNTs, and correlate these changes with deformation.

By using a stage with piezo drives to induce an alternating electrical field between a nanowire and an electrode, controlled frequency vibrations can be set up in the nanowire (Wang et al., 2001, 2002a). For example, in ZnO wires of rectangular cross section, each direction of vibration has its own resonances from which the modulus and time constant or Q factor can be derived (Bai et al., 2003a; Figure 6–31). Such measurements of bending modulus can be related to defects in individual structures (Gao et al., 2000). In fact, the mechanical resonance depends so sensitively on the structure that modulus measurements have potential use for measuring small masses. A less quantitative application (at present) is a stage developed for stretching chains of nanoparticles, of interest for their use as reinforcing fillers and their

presence in diesel exhausts (Suh et al., 2004). It will be exciting to see these mechanical techniques applied to more complex structures such as composite nanowires or filled CNTs.

5.4 Summary

Mechanical deformation has been successfully examined *in situ* using several innovative techniques. The future challenge in mechanical testing is to make its results even more quantitative and to minimize or account for thin foil effects. Customised design of specimens using MEMS technology, integrating for example tensile testers, tweezers, notches, or other structures, will certainly become more widespread for thin film experiments. Measurement of stress-strain curves during nanoindentation will provide accurate information on the mechanical response of a system, for example as single dislocations are introduced. Deposition of a film of interest, perhaps with an engineered boundary, onto a crystalline membrane may become useful in some cases, since the substrate deformation can be measured accurately from its strain contrast. Integration of such experiments with controlled atmosphere TEM will allow materials to be tested under the most realistic conditions. Elegant results on nanostructures have already been achieved using nanomanipulation with a tip. There is no doubt that these types of experiments are already bringing our understanding of the mechanical properties of small volumes of materials to a new level of precision.

6 Correlation of Structural and Electrical Properties of Materials

We have shown that fascinating data can result from the correlation between an applied stimulus, such as temperature, environment, or strain, and a microstructural change. Extending this approach, if we measure the electrical properties of a material while also observing or changing its structure, we can investigate structure-electrical property relationships in a unique way. The material under study can have a large volume, perhaps most or all of the TEM sample. Alternatively, structure-property relationships can be derived for individual nanostructures.

These interesting experiments all require electrical biasing holders, but not necessarily video rate recording, since the sample itself may change only slowly, or not at all. Examples include measuring the conductivity of individual nanowires as a function of their diameter, measuring changes in resistance as voids form during electromigration, measuring the potential distribution across p-n junctions as a function of bias, or measuring conductivity after dislocations are introduced.

6.1 Electrical Measurements on TEM Samples: Complete Samples as Devices

Many important processes can be studied by applying a voltage across a bulk or patterned specimen *in situ*. We have already described the

use of an applied voltage to generate an electric field for ferroelectric switching (Section 4.3), and now consider other possibilities. One interesting example is the measurement of electric fields across p-n junctions. This has been a favorite topic from the early days (Darlington and Valdre, 1975). More recently, a varying bias has been applied *in situ* across a FIB-prepared p-n junction, using holography to measure the potential distribution (Twitchett et al., 2002, 2004). The eventual aim of such studies is to understand the complex fields within real transistors, although quantitative image matching shows that surface effects must first be understood. Similar biasing experiments can be useful probes of other materials too. For example, the potential distribution across the boundary in a ferroelectric bicrystal was mapped by holography (Johnson and Dravid, 1999, 2000), showing breakdown and the presence of trap states associated with dopants.

In situ biasing also allows resistivity to be measured, which can then be correlated with a structural transformation. Thus, the amorphous to crystalline transformation for phase-change memory materials (Section 2.1) can be correlated with resistivity, as shown in Figure 6–32A (Verheijen et al., 2004). Similarly, phase transformations in TiNi shape memory alloys can be related to resistivity (Ma and Komvopoulos, 2005). Another interesting application of *in situ* resistivity measurement is the observation of conductivity changes during ion or electron beam irradiation to determine the cross section and threshold energy for Frenkel pair production (King et al., 1981; Haga et al., 1986).

In situ resistivity measurements have also been used to probe the electrical properties of dislocations (Ross et al., 1993). In this experiment, dislocations are formed progressively in a p-n junction diode by heating a metastable SiGe layer (Section 5.2) *in situ*. Measurement of the diode reverse leakage current as a function of dislocation density yielded the leakage current per length of dislocation, useful in device modeling. In this experiment, however, leakage was measured through the whole device, while dislocation density was measured only in the electron transparent area. Imaging of the whole device would have been more precise. Mathes et al. (2003) were, in fact, able to thin the entire active region of a laser structure by FIB, and observed degradation by dislocation formation during device operation. Such biasing studies could be combined with laser excitation *in situ* to examine degradation mechanisms and photoplasticity.

Current flow through narrow metal lines results in electromigration. Due to its importance and its strong dependence on microstructure, electromigration has been studied intensively *in situ* (Figure 6–32B). Current is passed through an Al or Cu line patterned onto an oxide substrate, with the aim of observing void formation and dynamics at microstructural features such as grain boundaries and precipitates. There are two important experimental concerns in these experiments. Passivation of the metal surface is known from SEM studies to alter failure lifetimes (Doan et al., 2001); passivating the lines makes the experimental results more relevant to real life, but it is then harder to see void shapes and dynamics. Joule heating in the lines can be another problem (Shih and Green, 1995), especially since elevated temperatures

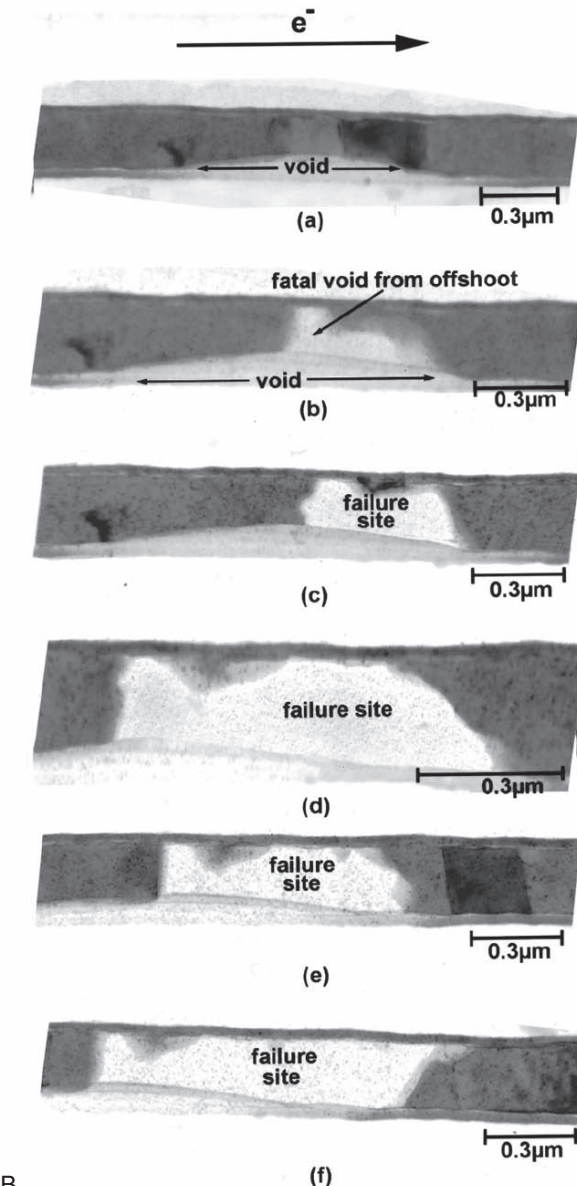
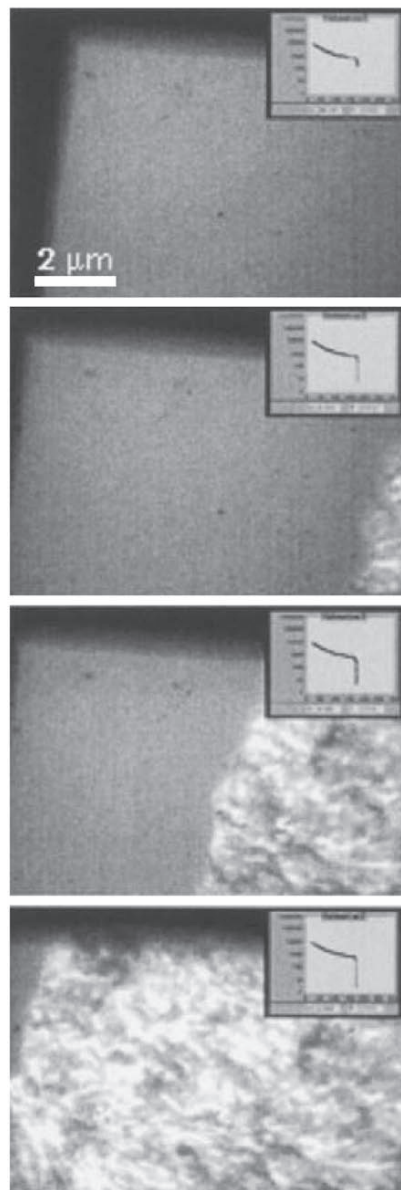


Figure 6-32. Correlation of resistivity with structure. (A) Video images taken at 15 s time intervals simultaneously displaying the crystallization of an Al-Ge film at 450 K and the accompanying drop in electrical resistance (insets). The crystallization front can be seen to proceed from the right- to the left-hand side. (Reprinted with permission from Verheijen et al., © 2004. American Institute of Physics.) (B) Evolution of a 300 nm wide Al (0.5 wt% Cu) interconnect line, 400 nm thick and 150 mm long on a 20 nm TiN underlayer. Lines are deposited on a SiN/SiO₂ bilayer membrane to minimise changes in the stress state on heating. 100 nm oxide passivation is added, and the lines are then annealed to form the bamboo structure (i.e., all grain boundaries run perpendicularly across the line). In situ stressing is carried out at 320°C and a current density of 2×10^6 A cm⁻², for (a) 3.5, (b) 4.0, (c) 4.1, (d) 4.5, (e) 4.6 and (f) 5.5 hours. (Reprinted with permission from Lau et al., © 1998 by the American Physical Society.)

and current densities above 10^6 Acm^{-2} are used for accelerated testing, so in some experiments, on-chip heat sink structures are integrated into the samples (Prybyla et al., 1998).

These studies show that electromigration-induced voids nucleate well before complete failure of the lines (Riege et al., 1996), and void dynamics depend on the local grain boundary structure. The failure mechanism depends on temperature, since at high temperature voids unpin from grain boundaries while at lower temperatures they grow at their nucleation site (Prybyla et al., 1998). Interestingly, when TiN barrier layers are present, voids do not migrate, presumably due to changes in surface diffusion (Lau et al., 2000). Even thin oxide films alter electromigration kinetics. Surface diffusion is in fact the dominant failure mechanism if grain boundary motion is hindered (Vook, 1994; Chang and Vook, 1995).

Since a thick passivation layer may be essential for meaningful results, in some studies the sample is mounted vertically and imaged in cross section at high voltage (Okabayashi et al., 1996; H. Mori et al., 1997). Such experiments show mass transport through Al and TiN layers, as well as vertical void and whisker growth. The measurement of local strain by CBED during electromigration (Nucci et al., 2005) is an exciting recent development that promises to relate these *in situ* results more closely to models.

6.2 Electrical Measurements on Individual Nanostructures

The experiments described above, where electrical biasing is applied to a relatively large volume of the specimen, probe several important phenomena. At the nanoscale, equally interesting information is provided by biasing individual nanostructures using STM technology. Commercial TEM/STM holders are in fact becoming increasingly common for both electrical and mechanical applications (www.nanofactory.com, www.gatan.com).

As with the mechanical experiments in Sections 5.3.2 and 5.3.3, carbon nanotubes and Au wires are favored for electrical studies. We firstly discuss CNTs. One can bias a tip on which a tube has been placed or grown, or equivalently bias the tip and approach a tube on the substrate. This allows observation of the electric field distribution at the tip of a biased tube (Cumings et al., 2002), and structural changes during field emission (Wang et al., 2002b; Kuzumaki et al., 2004; Jin et al., 2005). The work function of CNTs can be measured and related to structure (Gao et al., 2001; Bai et al., 2003b; Xu et al., 2005a, b) and CNT growth can be observed in the gap between a biased tip and the substrate (Yamashita et al., 1999).

If an individual tube is contacted, its conductivity can of course be measured. Kociak et al. (2002) were even able to correlate the chiral indices of double walled tubes, measured using diffraction, with their transport properties (Figure 6–33). Conductivity measurements show that CNTs are ballistic conductors at room temperature (Poncharal et al., 2002), and that the telescoping multiwalled CNTs mentioned in Section 5.3.3 behave as near-ideal rheostats (Cumings and Zettl, 2004).

Structural changes taking place during current transport have also been observed (Huang et al., 2005).

The other common material for electrical studies is Au. When thin wires are formed by touching Au tips to a substrate and then pulling away, the conductance can be measured and correlated with the structure. Figure 6–34 demonstrates quantized conductance through single and double Au chains (Ohnishi et al., 1998b). Single chains in fact show a metal-insulator transition (Kizuka et al., 2001a). Conductance and structure change together, showing the dynamic nature of the system (Kizuka et al., 2001b; Oshima et al., 2003c). Catalytically grown nanowires (Section 3.6) provide another interesting subject for study. Although Larsson et al. (2004) measured the conductivity of GaAs nanowires, nanowire electrical properties have generally not been examined in as much detail as Au wires or CNTs.

For any nanostructure studied *in situ*, the nature of the contact, for example how the STM tip is cleaned, is important in ensuring that the measurements relate to the structure rather than the contact. A drop of Hg can be used (Poncharal et al., 1999; Wang et al., 2001; Kociak et al., 2002) to measure properties like work function and quantum conductance, but there are still real issues in creating ohmic contacts to nanostructures (Larsson et al., 2004) which must be solved before extending these experiments to a wider range of materials systems.

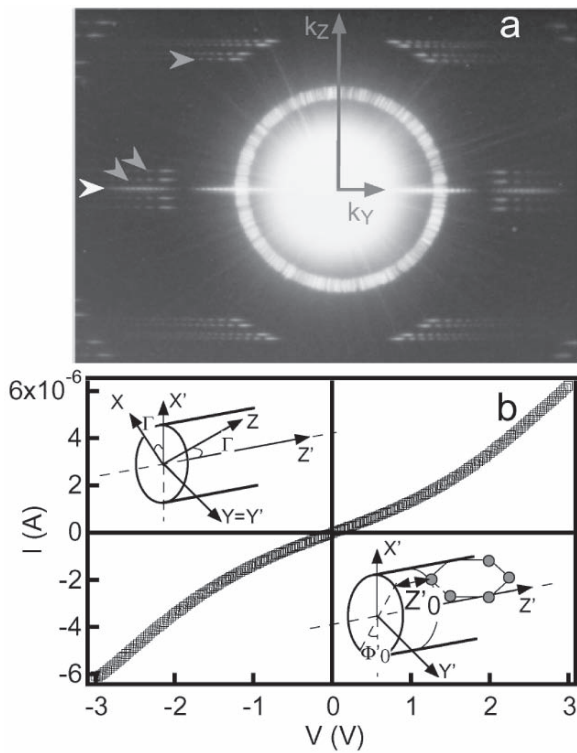
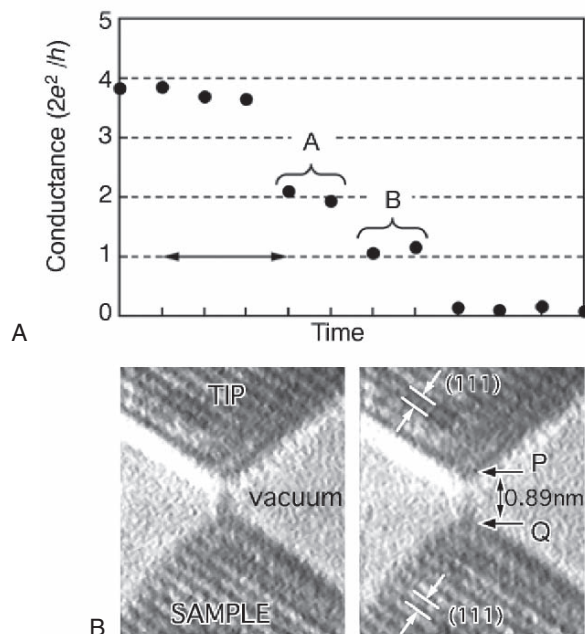


Figure 6–33. Simultaneous structure analysis and measurement of transport properties for a double-walled nanotube (DWNT). (A) Experimental diffraction pattern of a DWNT. The iris-like ring is an artifact. Note the layered line structure of the diffraction pattern. The white arrow indicates the equatorial line, and the gray ones indicate some other intensity lines. (B) Current-voltage characteristic of the same tube. Ohmic behavior is visible up to 0.5 V. Insets: Diffraction geometry. The upper inset shows the electron beam oriented along X with (X', Y', Z') the frame of reference of the MWNT. The diffraction pattern is recorded in the YZ plane. In the lower inset, a carbon atom (gray dot) is characterized by a translation distance Z'_0 and a rotation angle Φ'_0 with respect to the tube axis. (Reprinted with permission from Kociak et al., © 2002 by the American Physical Society.)

Figure 6–34. Electrical properties of nanowires. Quantized conductance of a single and a double strand of gold atoms prepared by contacting an Au surface with an STM tip in a UHV TEM. (a) Conductance change of the contact while withdrawing the tip. Conductance is shown in units of $G_0 = 2e^2/h = (13k\Omega)^{-1}$. (b) Electron microscope images of gold bridges obtained simultaneously with the conductance measurements in (a). Left, bridge at step A; right, bridge at step B. The bridge at step A has two rows of atoms; the bridge at step B has only one row of atoms. The distance from P to Q [(see (b)] is about 0.89 nm, wide enough to have two gold atoms in a bridge if the gold atoms have the nearest-neighbor spacing of the bulk crystal (0.288 nm). (From Ohnishi et al., © 1998. Courtesy of Nature/NPG.)



6.3 Outlook

In situ electrical experiments have touched a range of phenomena, providing detailed and unique information on both bulk and nanoscale materials. With nanostructured materials appearing in more and more electronic applications, we anticipate increased demand for the sort of information that only these experiments can provide. We also anticipate that other properties may be amenable to an analogous approach. Perhaps nanoscale optical response could be studied by feeding a laser beam into the sample area, or thermoelectric properties could be measured in nanoscale structures. No doubt equally fascinating behavior would be revealed.

7 Liquid Phase Processes

We now consider another unusual application of *in situ* TEM: studying the important class of processes that takes place in the liquid phase. For the vapor phase crystal growth and surface reaction processes of Section 3, real time observations clearly improved our understanding of nanostructure formation and thin film growth. Is it possible to carry out the same sort of quantitative studies for crystal growth from the liquid phase, or study other liquid processes? The answer, perhaps surprisingly, is yes, and the presence of a liquid is not incompatible with the vacuum requirements of the TEM. In this section we describe several studies involving liquids, which range from electrochemical deposition to the hydration of minerals and the growth of polymers.

In Sections 2.1 and 2.3 we presented examples of experiments involving melting and crystallization. These succeeded in the TEM either because the liquid was naturally trapped as an inclusion in a solid matrix, or because it had a low vapor pressure. Studies of vapor-liquid-solid growth (Section 3.6) also succeeded because of the low vapor pressure of the eutectic. For example, the vapor pressure above the Si-Au droplets in Figure 6-18 is only 10^{-10} Torr at the growth temperature.

But for liquids with higher vapor pressure, most importantly water, TEM can present some challenges. The liquid must be artificially encapsulated or differentially pumped to keep the pressure at the gun low enough for operation. Thus it is necessary either to use a special "window cell," in which the liquid is hermetically sealed between electron transparent membranes (windows), or to modify the microscope to increase pumping to the specimen area. Both approaches have advantages and disadvantages.

If a hermetically sealed cell is used, the windows cause undesirable background in the images. Furthermore, since the liquid scatters just as strongly as a solid, it must be confined within a short path length. Either it must be present as a thin film covering a solid support, or (if it is to fill the cell) the windows must be very close together, which can be an engineering challenge. Even for thin liquid films on a solid support, the window separation should be minimized, as a long path length of vapor above the liquid leads to undesirable electron-gas interactions, especially for water vapor (Shah, 2004). Window cells are complex and do not usually allow heating or two-axis tilting, although, as we will see below, electrical connections are possible. In spite of the experimental limitations, a hermetically sealed cell can allow liquid-covered specimens to be examined in a close to natural state, or can be used to maintain a solvent-rich atmosphere.

In the alternative approach, no windows are used, but instead additional apertures are incorporated into the TEM and the pumping in the specimen area is modified to maintain a high pressure at the sample while leaving the rest of the column at low pressure. Microscopes with differential pumping have already been described in the context of gas phase reactions, but they can also be used to observe samples on which a liquid is present. The liquid can be introduced by injecting it through a valve. This approach requires a dedicated microscope, but has the potential to provide higher resolution images than are possible using window cells, and is also compatible with conventional heating, cooling, and tilting holders.

Several studies involving liquids have overcome the experimental challenges described above and have yielded useful and unique information. Liquid phase TEM is still uncommon, however, and this is an area offering many opportunities.

7.1 Imaging in a Saturated Environment or Under a Liquid Film

Window cells or differentially pumped microscopes have been used in studies of a range of phenomena including hydration and dehydration of minerals, the growth of nanostructures, and the action of cata-

lysts. Early work was carried out using window cells to provide a water saturated atmosphere, for example in studying the hydration of Portland cement (see Butler and Hale, 1981, for a review). The use of high voltage microscopes meant that the window separation was not too critical. Since then, several groups have used window cells to image biological and non-biological samples. Such cells are often based on the design of Fukami et al. (1991). The windows consist of 20 nm amorphous C membranes attached over a perforated metal disc. This material can withstand a pressure differential of 250 Torr and does not produce much background in the images. Imaging in an atmosphere of ~100 Torr air saturated with water vapor allowed Sugi et al. (1997) to examine an interesting biological mechanism: the movement of the myosin head in living muscle filaments. It also allowed Daulton et al. (2001) to determine the oxidation state of Cr in particles produced by an important Cr-reducing bacterium. Use of a window cell for biological materials avoids cryofixation with its attendant artifacts, so that for example bacterial cells do not burst, although beam damage still occurs at high doses. By injecting liquid droplets into a window cell, Foo et al. (2001) and Chiou et al. (2002) examined the arrangement and shape of small particles suspended in solvent, such as fume silica, smectite, and Au modified with DNA. Use of the window cell avoided the problem of agglomeration which usually occurs on evaporation. Although not strictly *in situ* experiments, this work illustrates the possibilities for examining liquid phase dynamics of small particles.

As mentioned above, the use of a differentially pumped electron microscope allows for greater flexibility in the sample holder during liquid experiments. This approach has been successful for examining melting of Xe films (Zerrouk et al., 1994), liquid phase synthesis of Au nanorods (Gai and Harmer, 2002), and several important catalytic reactions, including the sequence used to form nylon (Gai, 2002b). The first reaction in this sequence, shown in Figure 6–35, was observed by injecting the precursor, in a methanol solvent, over a metal/TiO₂ catalyst specimen, while simultaneously heating the catalyst and flowing hydrogen; the second reaction was observed at a higher temperature on introduction of adipic acid. Since many commercial polymerization reactions take place from solution, these types of experiments can have significant impact on the development of industrial processes, in the same way that gas phase experiments have supported industrial development of gas reaction catalysts. Recently, imaging in an environment of varying relative humidity using differential pumping and a cooling stage has allowed the deliquescence of salt and aerosol particles to be correlated with their structure and composition (Wise et al., 2005). The importance of these particles in the Earth's atmosphere makes this an urgent area for further investigation.

7.2 Electrochemical Deposition

Electrochemical deposition is an important crystal growth process which takes place from the liquid phase. Among its many applications

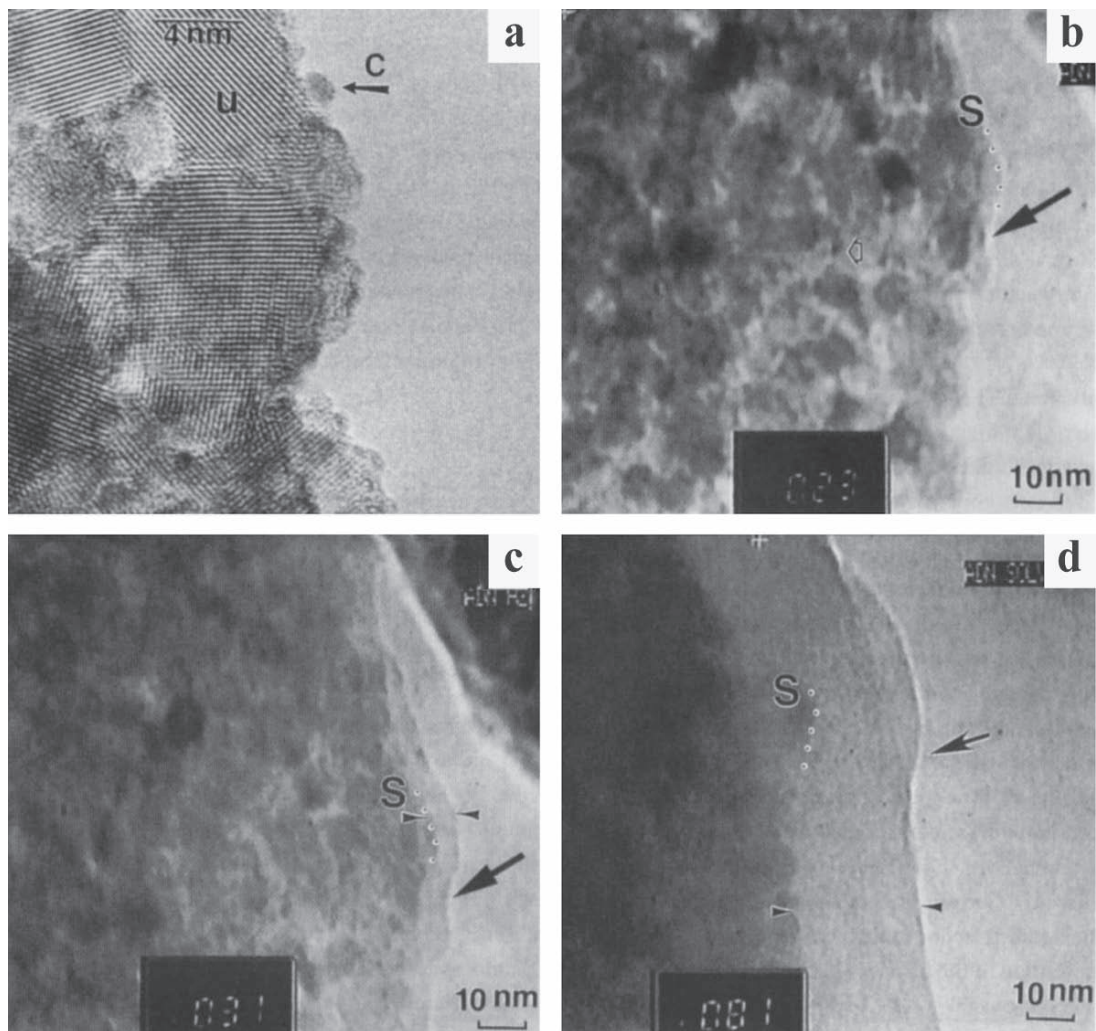


Figure 6–35. A liquid phase reaction *in situ*. The hydrogenation of adiponitrile (ADN) forms hexamethylene diamine (HMD), an important material since it in turn is reacted with adipic acid and polymerized to produce nylon 6,6. The ADN to HMD reaction is carried out with ADN in a methanol solvent under gaseous hydrogen over a metallic catalyst. (a) High-resolution image of the catalyst, nanoclusters of Co–Ru (arrowed, c) over rutile titania support (with larger grains, u), at RT. (b) After immersion in adiponitrile in solvent and H_2 gas, at RT. (c) The formation of layers of the product HMD at 31°C. The width is indicated by double arrows. (d) Thicker layers form at 81°C (arrowed) after 3 min. (S with dots indicated the original catalyst profile.) (From Gai, 2002. Courtesy of Cambridge University Press.)

is the formation of the copper interconnects in integrated circuits, and a detailed understanding of nucleation and growth is important in optimizing this process. In order to study electrochemical deposition, not only must imaging be carried out in a stable liquid environment, but it must also be done under electrochemical control. Thus the experiment uses a window cell, as described above, with electrical connections, as discussed in Section 6.

The electrochemical window cell (Williamson et al., 2003; Radisic et al., 2006) includes three electrodes connected externally to a potentiostat, allowing the same degree of control as a standard electrochemical cell. The entire volume between the windows is filled with the electrolyte, and the current passes between the working and counter electrodes through this liquid. The working electrode, on which the material of interest is deposited, is patterned over one of the windows. The counter electrode and reference electrodes are thin wires extending into the liquid reservoir. Since the cell volume is completely filled, unlike the experiments described above, it is particularly important to restrict the window spacing to below 1–2 µm to minimize multiple scattering. An imaging filter may be used to improve the contrast.

Typical results, given in Figure 6–36, show the nucleation and growth of copper clusters on a gold electrode in real time, with simultaneous measurement of the voltage applied and the current flowing in the cell. If care is taken to verify that the behavior of the small area of electrode under observation is typical of the entire electrode, and that the small volume cell behaves like a standard electrochemical cell, quantitative data on individual clusters can be compared with electrochemical models. In the experiment shown here, conventional electrochemical models could not explain the nucleation density and growth rates observed. Conventional models include only direct attachment of copper ions onto existing clusters, and to explain the results it was necessary to modify these models to include a parallel pathway, direct attachment of Cu onto the electrode followed by surface diffusion to clusters (Radisic et al., 2006).

Although complex, the electrochemical liquid cell developed here may be adapted for a variety of electrochemical growth and corrosion processes. In the future, this type of experiment could be enhanced by combining the cell with microfluidics technology to allow flowing rather than stationary liquid, and to enable controlled mixing or heating of liquids.

7.3 Outlook

Dynamic processes which take place in liquids and at liquid/solid interfaces have great importance across broad areas of science and technology. The results described in this section show that processes involving water or other liquids may indeed be observed in real time and with reasonable spatial resolution *in situ*, providing information which is difficult to obtain using techniques such as scanning probe microscopy or SEM. Further experiments could improve our understanding of, for example, changes in electrode surfaces during battery charging or underwater corrosion of metals such as steel. We anticipate that future liquid studies in the TEM will provide important information relevant to microelectronics fabrication, catalyst design, and certain biological processes, making this a key area of *in situ* TEM for further development.

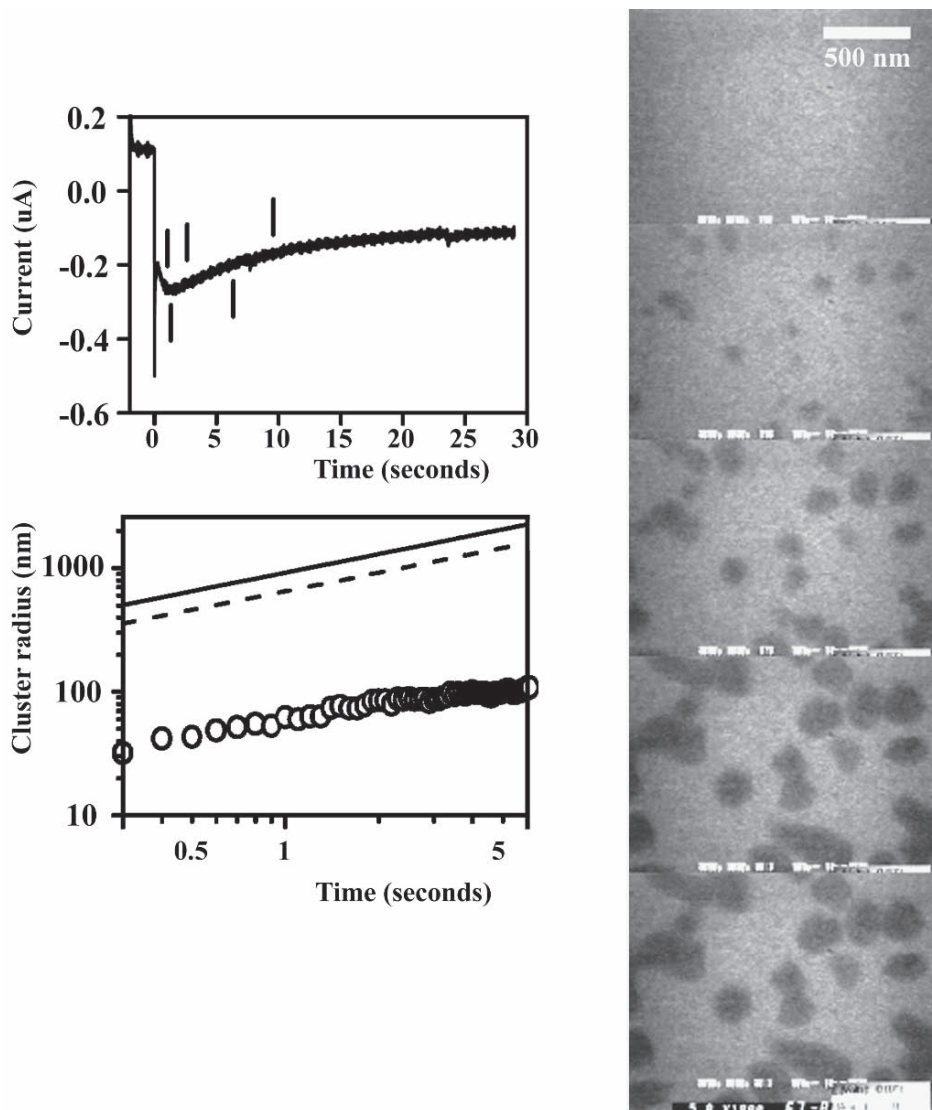


Figure 6–36. Electrochemical deposition of copper. Deposition was carried out *in situ* onto a gold electrode from acidified CuSO_4 solution. First a reverse potential was applied for 2 seconds to clean the electrode, then deposition was carried out at a constant potential of -0.07 V , measured with respect to a Cu reference electrode. The upper graph shows the current flowing through the TEM cell. After a sharp transient, the current curve shows a characteristic maximum ($-0.26\text{ }\mu\text{A}$ after 1.5 seconds in this case) which can be fitted with a model of cluster nucleation and growth. The images provide a direct view of cluster evolution on part of the electrode, with Cu appearing dark. The lower graph shows the growth of a single cluster (radius vs. time) compared with the prediction of two models. The growth rate is much slower than predicted, and the cluster density much higher, suggesting that the models need to be modified by the inclusion of surface diffusion effects. (From Radisic et al., © 2006 with permission of the American Chemical Society.)

8 Ion and Electron Beam-Induced Processes

Ion and electron beams have multiple effects on a specimen, depending on the material, and atomic displacements, implantation of atoms, or ionization may all be seen during *in situ* experiments. Irradiation

effects are certainly worthy of study both as basic and applied science, and are of interest far beyond simply understanding TEM artifacts. Historically, irradiation damage by ions, electrons, or both simultaneously was studied *in situ* in attempts to model neutron damage in the context of nuclear electric power generation and the development of host materials for long term nuclear waste storage. The high dose rates possible make TEM useful for accelerated experiments, and irradiation-induced defects and the effects of irradiation on phase equilibria and electrical and mechanical properties were studied. However, several other areas have recently become interesting. These include materials processing (ion beam assisted deposition, ion beam modification of interfaces, and ion implantation for microelectronics processing), development of semiconductor devices for aerospace applications, photoplasticity, and the study of radiation damage in minerals in order to improve the dating of radioisotope-bearing minerals. A recent review can be found in Birtcher et al. (2005).

8.1 Electron Beam-Induced Phenomena

In this section we discuss several effects of the electron beam on the specimen. Electron beam effects may be obvious, such as heating that induces or accelerates phase transformations, or more subtle, such as an increased point defect concentration that may affect deformation. Beam effects must of course be considered when interpreting any TEM observation, but can also be used to probe defect dynamics or growth processes.

8.1.1 Interaction with the Atmosphere Above the Specimen

As discussed in Section 3.4, the interaction of the electron beam with the column atmosphere produces a plasma in which structures such as fullerenes can grow, or certain components of oxides can be etched. Water vapor has a particularly strong interaction with the beam, as mentioned in Section 7. Beam-atmosphere interactions must be considered when using a microscope without a controlled environment, because they can lead to uncontrolled effects. But even when the environment is controlled, interactions will of course still occur. For example, in the hydrogen embrittlement studies described in Section 5.1, the electron beam significantly increases the “fugacity” (an effective partial pressure) of the hydrogen (Bond et al., 1986).

Beam effects in a reactive atmosphere can be used to advantage for deposition. For example, tungsten can be deposited via electron beam stimulated decomposition of $\text{W}(\text{CO})_6$ (Furuya et al., 2003) to grow structures such as that shown in Figure 6–37. Similarly, iron can be deposited from $\text{Fe}(\text{CO})_5$ (Tanaka et al., 2005; Takeguchi et al., 2005). Three dimensional structures may even be formed using a programmed STEM (Shimojo et al., 2004).

8.1.2 Formation and Dynamics of Point Defects

Once the beam hits the sample it creates point defects, and both point defect motion and the dynamics of phenomena induced by point defects can be examined *in situ*. In general, individual point defects are

difficult to see. However, if the specimen is thin and has a well-defined structure, such as a carbon nanotube, it may be possible to image point defects directly. Thus, point defects caused by irradiating graphene sheets may be imaged at high resolution (Hashimoto et al., 2004), and individual vacancy-interstitial pairs can be observed in double walled CNTs (Urita et al., 2005). Their relaxation can be measured, as can the defect-induced migration of metal atoms (Urita et al., 2004).

When point defects cluster into extended defects, the extended defect dynamics can be measured to obtain indirect information about the point defects such as their diffusion parameters. The fundamentals of point defect motion have been studied in many materials in this way using high voltage microscopy and are reviewed by Kiritani (1999). For example, by measuring the growth and shrinking of interstitial loops during intermittent irradiation, it is possible to obtain activation energies for vacancy migration and self diffusion (Arai et al., 1995). The density of point defects can be measured by examining the formation of jogs in dislocation loops (Arakawa et al., 2000) while their diffusion parameters can be measured by examining extended defect dynamics far from the irradiated area (Arai et al., 2004). Loop growth and shrinkage can even be used to investigate defects produced by *ex situ* neutron irradiation (Horiki et al., 1998; M.A. Kirk et al., 1999).

Extended defect dynamics also provides information on interactions between point defects and extended defects. In Cu, irradiation causes growth of stacking fault tetrahedra, and an analysis of size fluctuations showed that growth is by ledge motion after capture of defects (Arakawa et al., 2002). In Si, irradiation forms interstitial clusters, and Fedina et al. (1998) and Vanhellemont et al. (1995) observed their structure and formation kinetics (Figure 6–38). Strain fields influence point

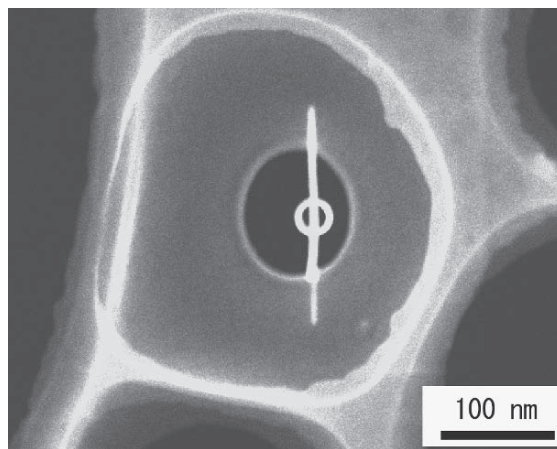


Figure 6–37. Fabrication of nanostructures by beam-vapor interaction. Nanoscale fabrication carried out on a carbon grid, using a JEM 2500SE STEM operated at 200 kV with a beam size of 0.8 nm and a beam current of 0.5 nA. W(CO)₆ gas was used at a flux of approximately 2×10^{-4} Pa L s⁻¹. A line across a hole was produced followed by fabrication of a circle. (From Shimojo et al., 2004; with kind permission of Blackwell Publishing, Ltd., Oxford, U.K.)

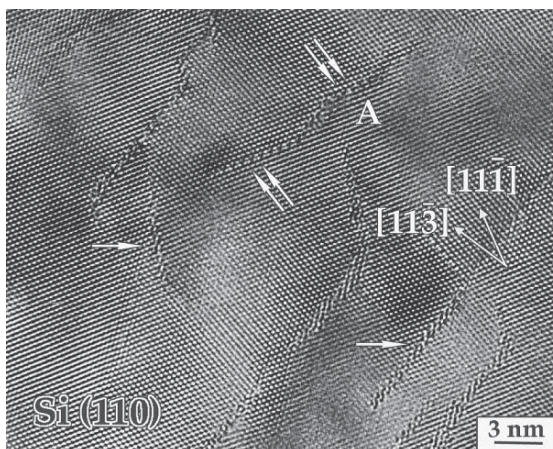


Figure 6–38. Irradiation damage. High-resolution electron micrograph image of point defect aggregates created in Si during electron irradiation at room temperature. Irradiation was carried out at 400 kV and 10^{20} electrons $\text{cm}^{-2}\text{s}^{-1}$ for 35 min. The {113} and {111} defects are marked with single and double arrows, respectively. (From Fedina et al., 1998 with kind permission of Taylor and Francis Ltd.)

defect clustering (Vanhellemont et al., 1995; Fedina et al., 1997), so presumably clustering could be used to measure strain locally. However, imaging of defect clusters can be challenging and special weak beam imaging techniques may be necessary (M.A. Kirk et al., 1999).

High voltage electron irradiation can be used to move atoms, say from the surface into the bulk of a substrate, via elastic collisions of the electrons with the heavy atoms. Systems studied include Au implanted into Si (Mori et al., 1992), Hf into SiC (Yasuda et al., 1992), and Au into Al (Lee et al., 2002b), which forms Al_2Au phases that move downstream. These experiments are useful in studying the phenomena taking place during ion beam processing.

8.1.3 Beam-Induced Phase Transformations, Surface Reactions and Growth

We have seen examples throughout this chapter where the beam has induced a phase transformation or caused a growth process. To understand these phenomena it is important to separate heating effects from those caused by knock-on damage or electronic excitations. This may require detailed hot stage measurements.

Amorphization is the most commonly observed beam-induced transformation, taking place for example in SiC (Inui et al., 1992), Si (Takeda and Yamasaki, 1999) and GaAs (Yasuda and Mori, 1999). In InGaN, beam-induced amorphization looks just like compositional fluctuations (Smeeton et al., 2003) which may of course cause problems in image interpretation. Interestingly, in Zr_2Ni and Zr_3Al , the amorphization kinetics are changed by the presence of hydrogen (Tappin et al., 1995), which alters the stability of the defective structure. Thus the microscope atmosphere should be considered in these transformations as well. The reverse process of beam-induced recrystallization also

occurs, for example in semiconductors (e.g., Jencic et al., 1995). It may be seen at voltages below those required to create point defects, and may be caused by the formation of dangling bonds at the crystalline/amorphous interface. Other beam effects include phase separation and the formation of non-equilibrium phases (Section 2). For example, in borosilicate glasses, which have applications in nuclear waste storage, B-rich phases separate under the beam (K. Sun et al., 2005).

Beam-induced growth processes have interesting applications in nanofabrication. Apart from the beam-induced deposition described in Section 8.1.1, nanostructures can be built by defect generation in suitable substrates (see Section 3.4 for C examples) and wires can be formed by beam-enhanced surface diffusion (see Section 3.1 for an Au example). Nanostructured material can also be formed by beam-induced decomposition. This has been examined particularly in SiO₂, where a combination of sputtering and desorption produces Si rich regions (Fujita et al., 1996; Chen et al., 1998; Du et al., 2003; Furuya et al., 2003). Beam-induced decomposition occurs in many materials (Al₂O₃, MgO, AlF, etc.) and may proceed from either or both surfaces. Several processes are active, including interactions with the atmosphere, changes in surface diffusion (Mera et al., 2003) and surface roughening (Grozea et al., 1997). If the beam is finely focused, such as in a STEM, hole drilling may occur (e.g., Berger et al., 1987; Walsh, 1989; Kizuka and Tanaka, 1997a, b), another possible method of fabricating nanostructures.

8.1.4 Radiation-Enhanced Dislocation Motion

In many materials, the electron beam influences dislocation motion. Radiation-enhanced dislocation glide during heating or straining has been studied quantitatively by recording the motion of individual dislocations (Figure 6–39). Such measurements suggest a mechanism based on an enhancement in the creation rate of kink pairs, due to energy that is released by nonradiative recombination of electron-hole pairs at electronic levels associated with dislocations (Levade et al., 1994; Werner et al., 1995; Yonenaga et al., 1999; Vanderschaeve et al., 2000, 2001; Maeda et al., 2000). The radiation-enhanced motion of individual kinks can actually be observed directly in plan view (Inoue et al., 1998). A radiation-enhanced climb process can also occur, due to absorption of interstitials by dislocations (Yonenaga et al., 1998). These studies are important in interpreting *in situ* deformation experiments, but also have a close relationship to the phenomenon of photoplasticity which is relevant to optoelectronic device degradation.

8.2 Ion Implantation

It is possible to irradiate a sample with ions while simultaneously imaging or irradiating it with electrons. This area of research requires complex, expensive instruments with tandem accelerators. However, because of the importance of the results, such equipment has been funded by several institutions around the world. A discussion of the microscopes capable of simultaneous ion and electron irradiation can be found in Allen and Ryan (1998) and some of the research has been summarized by Ruault et al. (2005). Our understanding of sputtering, ion

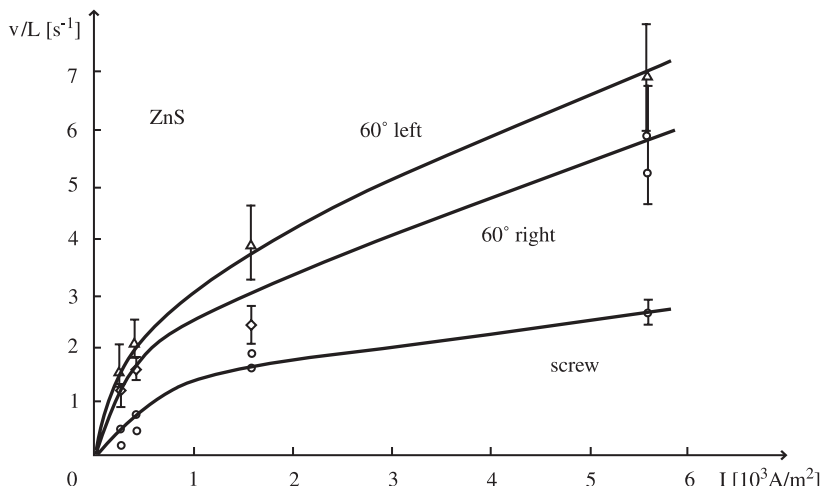


Figure 6–39. Radiation-induced dislocation glide. Velocity of dislocations in ZnS of different types per unit length, plotted as a function of electron beam intensity. Velocities were measured during *in situ* straining at $40\pm10\text{ MPa}$ and 390 K . The motion remains slow suggesting that the Peierls mechanism still controls motion, and velocity is proportional to dislocation length showing that kinks form individually and do not collide. The linear regime at low intensity suggests a change (reduction) in apparent activation energy due to nonradiative recombination of carriers at dislocations, assisting kink formation. At high intensities the recombination rate saturates. (From Levade et al., 1994 with kind permission of Taylor and Francis Ltd.)

implantation, and materials processing, for example by impurity doping, may be developed using tandem microscopes. However, the driving force for these microscopes is a need to understand the effects of radiation on materials which may be used in reactor walls or for storage of radioactive waste. Simultaneous ion and electron irradiation simulates the defect types and concentrations created by irradiation with high energy neutrons from nuclear reactions. Neutrons induce displacement damage and cause the formation of helium as a byproduct. The helium forms bubbles and causes swelling, embrittlement, and radiation-induced segregation, and phase stability may change as a result.

Because of their industrial importance, many irradiation studies have been carried out in steels. These include determining the stability of different phases after Xe irradiation (Chu et al., 2002) and measuring parameters of the motion of bubbles formed by He implantation (Ono et al., 2002). Quantitative studies provide information on the key defect formation and diffusion processes taking place. For example, in Cu, the kinetics of displacement collision cascade formation and the recombination of point defects into clusters were measured using Kr irradiation (Daulton et al., 2000), while in Si, irradiation with Si shrinks the bubbles caused by H implantation (Ruault et al., 2002). Bubble motion has been studied in most detail in a simple system, however. This model system consists of insoluble noble gases such as Ar, Ne, or Xe implanted into an Al or similar matrix, forming small precipitates (Figure 6–40A). Implantation can be carried out *ex situ* (Birtcher et al.,

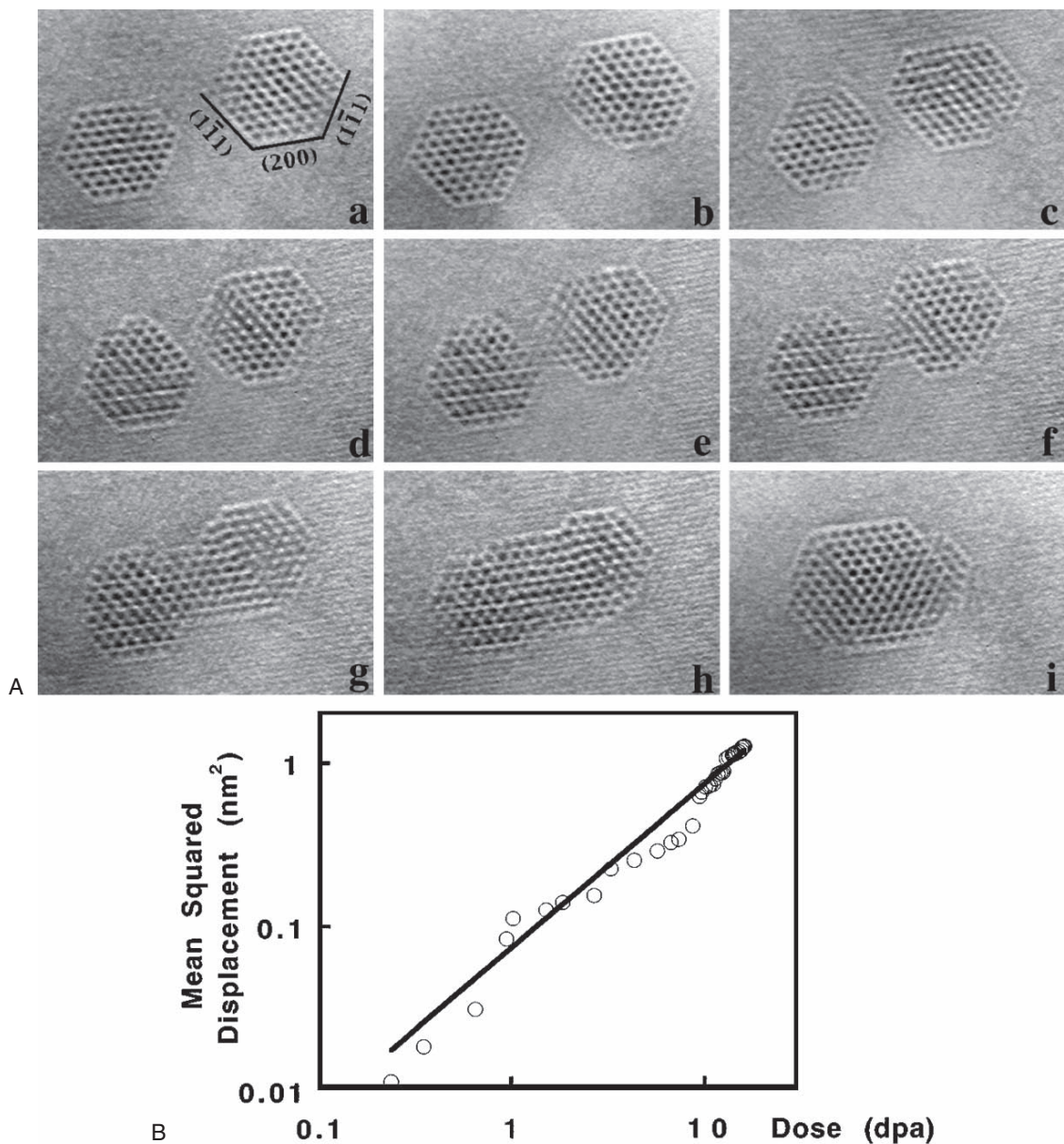


Figure 6-40. Dynamics of Xe precipitates. (A) Motion and coalescence of two isolated crystalline Xe precipitates (Xe implanted *ex situ*) during continuous 1 MeV electron irradiation at room temperature. The irradiation causes a damage rate in Al of approximately 3.9×10^{-2} displacements per atom (dpa) per second. Measured from the first image, the elapsed times at which video frames were recorded are (a) 0, (b) 101, (c) 418, (d) 549, (e) 550, (f) 551, (g) 561, (h) 584, and (i) 727 s. Traces of crystallographic planes are indicated in frame (a). Analysis of such data shows that surface diffusion of Al is responsible for motion and shape changes, while the Xe deforms by shear in response to the reshaping of its cavity. Since the total volume, not the surface area, was conserved during coalescence, cavity pressure depends on the gas structure and not just the interface structure. (Reprinted with permission from Birtcher et al., © 1999 by the American Physical Society.) (B) Mean square displacement of a Xe precipitate containing approximately 38 Xe atoms (in a volume equivalent to that of approximately 128 Al atoms), as a function of damage in the Al matrix under 1 MeV electron irradiation. The precipitate moves because of Al jumps on its surface, and these data yield values for the diffusivity and an average jump frequency of about 5600 jumps/dpa. (Reprinted with permission from Allen et al., © 1999. American Institute of Physics.)

1999; Allen et al., 1999; Ono et al., 2002) or *in situ* (Song et al., 2002), so that the coalescence of defects to form the precipitates can be studied as a function of dose. Striking dynamic changes occur in these precipitates under 1 MeV electron irradiation (Birtcher et al., 1999; Allen et al., 1999) or on heating (Ono et al., 2002): migration, shape changes, faulting, melting, crystallization, and coalescence. The shape, nature, and motion of the enclosed phase provide information on interface energies, structure, and diffusion pathways (Donnelly et al., 2002; Allen et al., 2003; Figure 6–40B).

We conclude with a related but lower voltage ion irradiation project: the integration of a 20 kV focused ion beam into a TEM (M. Tanaka et al., 1998; Gnauck et al., 1998). This tandem microscope allows the damage produced by the FIB to be observed directly, which is useful for understanding artifacts and low voltage damage effects. It also allows sample thinning to be carried out *in situ* so that the area imaged has not been exposed to the air. Studies of focused ion beam damage are increasingly important since the FIB is used for materials processing, surface patterning, growth, and fabrication of nanostructures.

9 Outlook

In this chapter we have attempted to show some of the outstanding recent results achieved using *in situ* microscopy and to illustrate the huge variety of experiments possible. In spite of experimental complexity, many successful and informative experiments have mimicked the real world inside the microscope column.

It has become clear that there is no one “*in situ* microscope.” Interesting experiments can be done in conventional machines, using standard holders, just by heating the sample with the electron beam. More complex experiments can be carried out by purchasing commercial *in situ* holders (heating, cooling, straining) or by developing customized ones (nanoindenters, electrical biasing holders, window cells). Many experiments also require the ability to measure some property of the sample, such as resistivity, simultaneously with imaging its structure. The most complex *in situ* experiments take place in expensive microscopes which are modified to achieve a controlled specimen environment or are designed for UHV.

This is an exciting time for *in situ* microscopy. Specimen design is developing rapidly with innovative use of FIB preparation or integration of thin film specimens into micromachined substrates. Furthermore, as we have emphasized throughout this chapter, the increased interest in nanostructures fits perfectly with the ability of TEM to analyze small volumes of material with minimal sample preparation. Apart from thin foil effects and beam-induced artifacts, the main limitation of *in situ* microscopy has been the small space available in the polepiece. In the future this problem too will be solved by the ongoing developments in aberration correction. Corrected microscopes have an increased polepiece gap for the same resolution. The extra space will help experiments requiring combined stimuli (heating and irradiation,

straining in a gas environment, simultaneous E and B fields) or new stimuli (lasers, micromanipulators, microfluidics). An increased pole-piece gap will also improve calibration of the sample environment. It is hard to overemphasize the importance of this for quantitative results. For example, one could include a fiber optic coupled to a radiation thermometer (Isshiki et al., 1998), a thickness monitor for growth experiments, a pressure gauge, or MEMS-based sensors. Aberration correction would also allow low voltage microscopes to achieve a resolution comparable with today's high voltage microscopes. This will reduce beam damage, although sample thickness, or more generally sample design, will remain a constraint to decreasing the voltage.

However, there are many areas where *in situ* techniques could be extended even without aberration correction. Relatively few *in situ* experiments have used analytical techniques, such as energy filtered imaging or EELS, to examine time-resolved chemical changes. This is probably because rapid acquisition limits the signal to noise ratio. Thus, the ongoing improvements in detectors are promising for *in situ* analytical studies. Similarly, convergent beam electron diffraction has not been widely used *in situ*, but could give useful information on changes in local strain. And other advanced TEM techniques such as tomography, holography, or imaging of amorphous materials could also be used *in situ*, providing the phenomenon of interest is slow enough to make image acquisition feasible. High speed imaging, discussed elsewhere in this book, will of course open a new set of phenomena for study. And in terms of data collection and analysis, direct storage of images and videos on disc is improving the searchability of data, although most data collection still leaves something to be desired in terms of usability. Intelligent analysis of video data, such as object detection and tracking, is currently a limitation, as custom software often has to be developed for each experiment.

A final comment arises from the complexity of controlled environment *in situ* microscopes, which has increased since the development of the first such TEM by Poppa (1965). Although some processes, such as sample heating, must take place in the polepiece, it is an advantage to keep others out of the polepiece though still in the same vacuum system. Examples include ion guns or deposition tools such as evaporators. Moving some capabilities *ex situ*, but within the same vacuum system, improves the reliability of complex microscope systems and provides a more flexible approach to experiments, especially in a multi-user environment where time is a constraint.

The field of *in situ* transmission electron microscopy has advanced tremendously since its beginning in the 1960s. We anticipate even more exciting results over the next few decades.

Acknowledgments. I would like to acknowledge the inspirational scientists with whom I have had the pleasure of working. In particular, my Ph.D. advisor the late Mike Stobbs, who emphasized quantitative information from TEM; my colleagues Murray Gibson, Robert Hull, Uli Dahmen, and Ruud Tromp; and Mike McDonald, Mark Reuter, and

Arthur Ellis, whose outstanding technical help made out *in situ* experiments possible. I would like to acknowledge the support of IBM's T.J. Watson Research Center with its far sighted view of basic research. I would also like to thank my husband and baby daughter, without whom writing this chapter would have been much easier.

References

- Abe, H., Yamamoto, S. and Miyashita, A. (2002). *J. Electron Microsc.* **51** (Supplement), S183–187.
- Allen, C.W. and Ryan, E.A. (1998). *Microsc. Res. Tech.* **42**, 255–259.
- Allen, C.W., Birtcher, R.C., Donnelly, S.E., Furuya, K., Ishikawa, N. and Song, M. (1999). *App. Phys. Lett.* **74**, 2611–2613.
- Allen, C.W., Birtcher, R.C., Donnelly, S.E., Song, M., Mitsuishi, K., Furuya, K. and Dahmen, U. (2003). *Philos. Mag. Lett.* **83**, 57–64.
- Aoki, K., Minoda, H., Tanishiro, Y. and Yagi, K. (1998). *Surface Rev. Lett.* **5**, 653–663.
- Arai, S., Morita, C., Arakawa, K. and Kiritani, M. (1995). *J. Electron Microsc.* **44**, 1–7.
- Arai, S., Tsukimoto, S., Muto, S. and Saka, H. (2000). *Micros. Microanal.* **6**, 358–361.
- Arai, S., Tsukimoto, S. and Saka, H. (2003). *J. Electron Microsc.* **52**, 79–84.
- Arai, S., Satoh, Y., Arakawa, K., Morita, C. and Kiritani, M. (2004). *J. Electron Microsc.* **53**, 21–27.
- Arakawa, K., Satoh, Y., Arai, S. and Kiritani, M. (2000). *Philos. Mag. A* **80**, 2041–2055.
- Arakawa, A., Arai, S., Orihara, H., Ono, K. and Kiritani, M. (2002). *J. Electron Microsc.* **51** (Suppl.), S225–229.
- Asaka, K. and Kizuka, T. (2005). *Phys. Rev. B* **72**, 115431.
- Bai, X.D., Gao, P.X., Wang, Z.L. and Wang, E.G. (2003). *App. Phys. Lett.* **82**, 4806–4808.
- Bai, X.D., Wang, E.G., Gao, P.X. and Wang, Z.L. (2003b). *Nano Lett.* **3**, 1147–1150.
- Balk, T.J., Dehm, G. and Arzt, E. (2003). *Acta Mat.* **51**, 4471–4485.
- Banhart, F. (1997). *J. App. Phys.* **81**, 3440–3445.
- Banhart, F. (1999). *Rep. Prog. Phys.* **62**, 1181–1221.
- Banhart, F., Hernandez, E. and Terrones, M. (2003). *Phys. Rev. Lett.* **90**, 185502/1–4.
- Barre, S., Mutka, H., Roucau, C., Litzler, A., Schneck, J., Toledano, J.C., Bouffard, S. and Rullier-Albenque, F. (1991). *Phys. Rev. B* **43**, 11154–11161.
- Bartsch, M., Schall, P., Feuerbacher, M. and Messerschmidt, U. (2005). *J. Mat. Res.* **20**, 1814–1824.
- Baufeld, B., Baither, D., Messerschmidt, U., Bartsch, M., Foitzik, A.H. and Ruhle, M. (1997). *J. Amer. Ceramic Soc.* **80**, 1699–1705.
- Bengu, E. and Marks, L.D. (2001). *Phy. Rev. Lett.* **86**, 2385–2387.
- Benson, W.E. and Howe, J.M. (1997). *Philos. Mag. A* **75**, 1641–1663.
- Berger, S.D., Salisbury, I.G., Milne, R.H., Imeson, D. and Humphreys, C.J. (1987). *Philos. Mag. B* **55**, 341–358.
- Bhattacharya, P., Bhattacharya, V. and Chattopadhyay, K. (1999). *J. Electron Microsc.* **48** (Supplement), S1047–1054.
- Birtcher, R.C., Donnelly, S.E., Song, M., Furuya, K., Mitsuishi, K. and Allen, C.W. (1999). *Phys. Rev. Lett.* **83**, 1617–1620.
- Birtcher, R.C., Kirk, M.A., Furuya, K., Lumpkin, G.R. and Ruault, M.O. (2005). *J. Mat. Res.* **20**, 1654–1683.

- Blanpain, B., Legresy, J.-M. and Mayer, J.W. (1990). *Colloque Phys.* **C-4**, 131–137.
- Bobji, M.S., Ramanujan, C.S., Doole, R.C., Pethica, J.B. and Inkson, B.J. (2003). *Mat. Res. Soc. Symp. Pro.* **778**, 105–110.
- Bond, G.M., Robertson, I.M. and Birnbaum, H.K. (1986). *Scripta Metallurgica* **20**, 653–658.
- Bonevich, J.E., Harada, K., Matsuda, T., Kasai, H., Yoshida, T., Pozzi, G. and Tonomura, A. (1993). *Phys. Rev. Lett.* **70**, 2952–2955.
- Bovin, J.-O., Wallenberg, R. and Smith, D.J. (1985). *Nature* **317**, 47–49.
- Burden, A.P. and Hutchison, J.L. (1998). *Carbon* **36**, 1167–1173.
- Butler, E.P. and Hale, K.F. (1981). Dynamic Experiments in the Electron Microscope, Vol. 9. In *Practical Methods of Electron Microscopy* (North-Holland, Amsterdam).
- Cai, W., Murakami, Y. and Otsuka, K. (1999). *Mat. Sci. Eng. A* **273–275**, 186–189.
- Caillard, D., Martin, J.L. and Jouffrey, B. (1980). *Acta Metallurgica* **28**, 1059–1067.
- Caillard, D., Vailhe, C. and Farkas, D. (1999). *Philos. Mag. A* **79**, 723–739.
- Caillard, D., Roucau, C., Bresson, L. and Gratias, D. (2002). *Acta Materialia* **50**, 4499–4509.
- Cantoni, M., Uchida, M., Matsui, Y., Takekawa, S., Tsuruta, T. and Horiuchi, S. (1998). *J. Electron Microsc.* **47**, 443–448.
- Chang, C.Y. and Vook, R.W. (1993). *Thin Solid Films* **223**, 23–30.
- Chatterjee, K., Howe, J.M., Johnson, W.C. and Murayama, M. (2004). *Acta Mat.* **52**, 2923–2935.
- Chen, G.S., Boothroyd, C.B. and Humphreys, C.J. (1998). *Philos. Mag. A* **78**, 491–506.
- Chiou, W.-A., Ishikawa, A., Foo, K.H., Miyata, H., Tsukada, H. and Fukushima, K. (2002). *Proc. ICEM-15* **1**, 937–938.
- Chong, R.K.K., Yeadon, M., Choi, W.K., Stach, E.A. and Boothroyd, C.B. (2003). *App. Phys. Lett.* **82**, 1833–1835.
- Chu, F., Song, M., Mitsuishi, K., Yasuda, H. and Furuya, K. (2002). *J. Electron Microsc.* **51** (Supplement), S231–234.
- Collazo-Davila, C., Grozea, D. and Marks, L.D. (1998). *Phys. Rev. Lett.* **80**, 1678–1681.
- Crozier, P.A., Oleshko, V.P., Westwood, A.D. and Cantrell, R.D. (2001). *Electron Microsc. Anal.* **2001**. Proceedings 393–396.
- Cumings, J. and Zettl, A. (2000). *Science* **289**, 602–604.
- Cumings, J. and Zettl, A. (2004). *Phys. Rev. Lett.* **93**, 086801/1–4.
- Cumings, J., Zettl, A., McCartney, M.R. and Spence, J.C.H. (2002). *Phys. Rev. Lett.* **88**, 056804/1–4.
- Dahmen, U., Hagege, S., Faudot, F., Radetic, T. and Johnson, E. (2004). *Philos. Mag.* **84**, 2651–2662.
- Dannenberg, R., Stach, E., Grozac, J.R. and Dresser, B.J. (2000). *Thin Solid Films* **379**, 133–138.
- Darlington, E.H. and Valdre, U. (1975). *J. Phys. E* **8**, 321–324.
- Daulton, T.L., Kirk, M.A. and Rehn, L.E. (2000). *Philos. Mag. A* **80**, 809–842.
- Daulton, T.L., Little, B.J., Lowe, K. and Jones-Meehan, J. (2001). *Microsc. Microanal.* **7**, 470–485.
- Dehm, G. and Arzt, E. (2000). *App. Phys. Lett.* **77**, 1126–1128.
- Dehm, G., Wagner, T., Balk, T.J., Arzt, E. and Inkson, B.J. (2002). *J. Mat. Sci. Tech.* **18**, 113–317.
- Diebolt, L., Sharma, R., McKelvy, M. and Glaunsinger, W.S. (1995). *Mat. Res. Soc. Proc.* **404**, 183–188.

- Doan, J.C., Lee, S., Lee, S.-H., Flinn, P.A., Bravman, J.C. and Marieb, T.N. (2001). *J. App. Phys.* **89**, 7797–7808.
- Donnelly, S.E., Birtcher, R.C., Allen, C.W., Morrison, I., Furuya, K., Song, M., Mitsuishi, K. and Dahmen, U. (2002). *Science* **296**, 507–510.
- Donnet, D.M., Lewis, V.G., Chapman, J.N., O’Grady, K. and van Kesteren, H.W. (1993). *J. Phys. D* **26**, 1741–1745.
- Dougherty, L.M., Robertson, I.M. and Vetrano, J.S. (2003). *Acta Mat.* **51**, 4367–4378.
- Drucker, J., Sharma, R., Weiss, K. and Kouvetsakis, J. (1995). *J. App. Phys.* **77**, 2846–2848.
- Du, X.W., Takeguchi, M., Tanaka, M. and Furuya, K. (2003). *App. Phys. Lett.* **82**, 1108–1110.
- Dutkiewicz, J., Bartsch, M., Miura, S., Messerschmidt, U. and Kato, H. (1995). *J. Phys. IV (Colloque)* **5(C2)**, 275–280.
- Fedina, L., Lebedev, O., Van Tendeloo, G. and Van Landuyt, J. (1997). *Proc. Microsc. Semicond. Mat.* **10**, 55–58.
- Fedina, L., Gutakovskii, A., Aseev, A., van Landuyt, J. and Vanhellemont, J. (1998). *Philo. Mag. A* **77**, 423–435.
- Follstaedt, D.M., Myers, S.M., Floro, J.A. and Lee, S.R. (1997). *Nucl. Inst. Methods Phys. Res. B* **127–128**, 375–378.
- Foo, K.H., Chiou, W.-A., Ishikawa, A., Fukushima, K. and Meshii, M. (2001). *Microsc. Microanal.* **7** (Supplement 2), 1216–1217.
- Fujisawa, S. and Kizuka, T. (2003a). *J. J. App. Phys. Part 2* **42**, L1182–1184.
- Fujisawa, S. and Kizuka, T. (2003b). *Tribol. Lett.* **15**, 163.
- Fujita, S., Maruno, S., Watanabe, H. and Ichikawa, M. (1996). *App. Phys. Lett.* **69**, 638–640.
- Fukami, A., Fukushima, K. and Kohyama, N. (1991). In *Microstructure of Fine Grained Sediments from Mud to Shale* (Bennett, R.H., Bryant, W.R., Hulbert, M.H., Eds.) 321–331 (Springer-Verlag, New York).
- Furuya, K., Mitsuishi, K., Shimojo, M. and Takeguchi, M. (2003). *Rev. Adv. Mat. Sci.* **5**, 381–386.
- Gabrisch, H., Kjeldgaard, L., Vaernholt Olesen, A., Johnson, E. and Dahmen, U. (2000). *Mat. Res. Soc. Sympos. Proc.* **580**, 257–264.
- Gabrisch, H., Kjeldgaard, L., Johnson, E. and Dahmen, U. (2001). *Acta Mat.* **49**, 4259.
- Gai, P.L. (1998). *Adv. Mat.* **10**, 1259–1263.
- Gai, P.L., Kourtakis, K. and Ziemecki, S. (2000). *Microsc. Microanal.* **6**, 335–342.
- Gai, P.L. (2002a). *Top. Catalysis* **21**, 161–173.
- Gai, P.L. (2002b). *Microsc. Microanal.* **8**, 21–28.
- Gai, P.L. and Harmer, M.A. (2002). *Nano Lett.* **2**, 771–774.
- Gai, P.L. and Kourtakis, K. (1995). *Science* **267**, 661.
- Gai, P.L., Smith, B.C. and Owen, G. (1990). *Nature* **348**, 430–432.
- Gajdardziska-Josifovska, M., Malay, M.H. and Smith, D.J. (1997). *Surface Rev. Lett.* **4**, 655–669.
- Gajdardziska-Josifovska, M., Plass, R., Schofield, M.A., Giese, D.R. and Sharma, R. (2002). *J. Electron Microsc.* **51** (Supplement), S13–S26.
- Gajdardziska-Josifovska, M. and Sharma, R. (2005). *Microsc. Microanal.* **11**, 524–533.
- Gao, R., Wang, Z.L., Bai, Z., de Heer, W.A., Dai, L. and Gao, M. (2000). *Phys. Rev. Lett.* **85**, 622–625.
- Gao, R., Pan, Z. and Wang, Z.L. (2001). *App. Phys. Lett.* **78**, 1757–1759.
- Gao, Y. and Bando, Y. (2002). *Nature (London)* **415**, 599.
- Gao, Y., Liu, Y.Q. and Wu, K.H. (1996). *Mat. Res. Soc. Sympos. Proc.* **404**, 171–176.

- Gemperlova, J., Jacques, A., Gemperle, A., Vystavel, T., Zarubova, N. and Janecek, M. (2002). *Mat. Sci. Eng. A* **324**, 183–189.
- Ghica, C., Nistor, L., Bender, H., Steegen, A., Lauwers, A., Maex, K. and Van Landuyt, J. (2001). *J. Mat. Res.* **16**, 701–708.
- Gibson, J.M., Batstone, J.L. and Tung, R.T. (1987). *App. Phys. Lett.* **51**, 45–47.
- Gignac, L.M., Svilan, V., Clevenger, L.A., Cabral, C. and Lavoie, C. (1997). *Mat. Res. Soc. Symp. Proc.* **441**, 225–230.
- Gloter, A., Suenaga, K., Kataura, H., Fujii, R., Kodama, T., Nishikawa, H., Ikemoto, I., Kikuchi, K., Suzuki, S., Achiba, Y. and Iijima, S. (2004). *Chem. Phys. Lett.* **390**, 462–466.
- Gnauck, P., Nisch, W. and Piles, E. (1998). *Proc. 14th Internat. Cong. Electron Microsc.* **3**, 515–516.
- Gottschalk, H., Hiller, N., Sauerland, S., Specht, P. and Alexander, H. (1993). *Phys. Status Solidi A* **138**, 547–555.
- Grant, A.W., Hu, Q.-H. and Kasemo, B. (2004). *Nanotechnology* **15**, 1175–1181.
- Grozea, D., Landree, E. and Marks, L.D. (1997). *App. Phys. Lett.* **71**, 2301–2303.
- Guder, S., Bartsch, M. and Messerschmidt, U. (2002). *Philos. Mag. A* **82**, 2737–2754.
- Haga, K., King, W.E., Merkle, K.L. and Meshii, M. (1986). *Nuc. Inst. Methods Phys. Res. B* **16**, 134–142.
- Hammar, M., LeGoues, F.K., Tersoff, J., Reuter, M.C. and Tromp, R.M. (1996). *Surface Sci.* **349**, 129–144.
- Han, X.D., Wang, R., Zhang, Z. and Yang, D.Z. (1997). *Mat. Lett.* **30**, 23–28.
- Hannon, J.B., Kodambaka, S., Ross, F.M. and Tromp, R.M. (2006). *Nature*, advanced online publication, 29 January (DOI 10.1038/nature04574).
- Hansen, P.L., Wagner, J.B., Helveg, S., Rostrup-Nielsen, J.R., Clausen, B.S. and Topsoe, H. (2002). *Science* **295**, 2053–2055.
- Hansen, T.W., Wagner, J.B., Hansen, P.L., Dahl, S., Topsoe, H. and Jacobsen, C.J.H. (2001). *Science* **294**, 1508–1510.
- Haque, M.A. and Saif, M.T.A. (2003). *Exp. Mech.* **43**, 248–255.
- Haque, M.A. and Saif, M.T.A. (2005). *J. Mat. Res.* **20**, 1769–1777.
- Haque, M.A. and Saif, M.T.A. (2004). *Proc. Nat. Acad. Sci.* **101**, 6335–6340.
- Harada, K., Matsuda, T., Bonevich, J., Igarashi, M., Kondo, S., Pozzi, G., Kawabe, U. and Tonomura, A. (1992). *Nature* **360**, 51–53.
- Harada, K., Kamimura, O., Kasai, H., Matsuda, F., Tonomura, A. and Moshchalkov, V.V. (1996a). *Science* **274**, 1167–1170.
- Harada, K., Kasai, H., Kamimura, O., Matsuda, T., Tonomura, A., Okayasu, S. and Kazumata, Y. (1996b). *Phys. Rev. B* **53**, 9400–9405.
- Harada, I., Kasai, H., Matsuda, T., Yamasaki, M. and Tonomura, A. (1997a). *J. Electron Microsc.* **46**, 227–232.
- Harada, K., Matsuda, T., Kasai, H., Kamimura, O. and Tonomura, A. (1997b). *Ultramicroscopy* **67**, 133–141.
- Hashimoto, A., Suenaga, K., Gloter, A., Uruta, K. and Iijima, S. (2004). *Nature* **430**, 870–873.
- Hattar, K., Han, J., Saif, M.T.A. and Robertson, I.M. (2005). *J. Mat. Res.* **20**, 1869–1877.
- Hattenhauer, R., Bartsch, M., Messerschmidt, U., Haasen, P. and Wilbrandt, P.-J. (1994). *Philos. Mag. A* **70**, 447–461.
- Haussler, D., Bartsch, M., Aindow, M., Jones, I.P. and Messerschmidt, U. (1999). *Philos. Mag. A* **79**, 1045–1071.
- He, H. and Tan, X. (2004). *App. Phys. Lett.* **85**, 3187–3189.
- He, H. and Tan, X. (2005). *Phys. Rev. B* **72**, 24102.

- Helveg, S., Lopez-Cartes, C., Sehested, J., Hansen, P.L., Clausen, B.S., Rostrup-Nielsen, J.R., Abild-Pedersen, F. and Norskov, J.K. (2004). *Nature* **427**, 426–429.
- Hirayama, H., Kawamoto, Y., Ohshima, Y. and Takayanagi, K. (2001). *App. Phys. Lett.* **79**, 1169–1171.
- Homma, Y. and Finnie, P. (2002). *J. Crystal Growth* **237–239**, 28–34.
- Horiki, M., Arai, S., Satoh, Y. and Kiritani, M. (1998). *J. Nucl. Mat.* **255**, 165–173.
- Horiuchi, S., Canton, M., Uchida, M., Tsuruta, T. and Matsui, Y. (1998). *App. Phys. Lett.* **73**, 1293–1294.
- Howe, J.M. (1996). *Philos. Mag. A* **74**, 761–775.
- Howe, J.M. (1997). *Interf. Mat.* (Wiley, New York).
- Howe, J.M. (1998). *Mat. Trans., JIM* **39**, 3–23.
- Howe, J.M., Murray, T.M., Moore, K.T., Csontos, A.A., Tsai, M.M., Garg, A. and Benson, W.E. (1998). *Microsc. Microanal.* **4**, 235–247.
- Howe, J.M., Reynolds, W.T., Jr. and Vasudevan, V.K. (2004). *Z. Met.* **95**, 275–278.
- Huang, J.Y., Chen, S., Jo, S.H., Wang, Z., Han, D.X., Chen, G., Dresselhaus, M.S. and Ren, Z.F. (2005). *Phys. Rev. Lett.* **94**, 236802/1–4.
- Hueging, N., Luysberg, M., Urban, K., Buca, D. and Mantl, S. (2005). *App. Phys. Lett.* **86**, 42112–42113.
- Hugo, R.C. and Hoagland, R.G. (1998). *Scripta Mat.* **38**, 523–529.
- Hugo, R.C. and Hoagland, R.G. (1999). *Scripta Mat.* **41**, 1341–1946.
- Hugo, R.C., Kung, H., Weertman, J.R., Mitra, R., Knapp, J.A. and Follstaedt, D.M. (2003). *Acta Mat.* **51**, 1937–1943.
- Hull, R. and Bean, J. (1994). *Mat. Res. Soc. Bull.* **19** (6), 32–37.
- Hull, R., Bean, J.C. and Buescher, C. (1989). *J. App. Phys.* **66**, 5837–5843.
- Hull, R., Bean, J.C., Bahnck, D., Petcolas, L.J., Jr., Short, K.T. and Unterwald, F.C. (1991). *J. App. Phys.* **70**, 2052–2065.
- Ichikawa, M., Fujita, S. and Maruno, S. (1998). *Proc. 14th Internat. Cong. Electron Microsc.* **13**, 147–148.
- Ichikawa, M. (1999). *J. Phys. Cond. Matt.* **11**, 9861–9870.
- Ii, S., Nishida, M., Murakami, Y. and Shindo, D. (2003). *J. Phys. IV (Proceedings)* **112**, 1035–1038.
- Ii, S., Iwamoto, C., Matsunaga, K., Yamamoto, T., Yoshiya, M. and Ikuhara, Y. (2004). *Philos. Mag.* **84**, 2767–2775.
- Iijima, S. and Ichihashi, T. (1986). *Phys. Rev. Lett.* **56**, 616–619.
- Inoue, M., Suzuki, K., Amasuga, H., Mera, Y. and Maeda, K. (1998). *J. App. Phys.* **83**, 1953–1957.
- Inui, H., Mori, H., Suzuki, A. and Fujita, H. (1992). *Philos. Mag. B* **65**, 1–14.
- Isshiki, T., Ohta, M., Nishio, K. and Shiojiri, M. (1995). *Thin Solid Fims* **271**, 84–87.
- Isshiki, T., Nishio, K., Deguchi, Y., Yamamoto, H. and Shiojiri, M. (1998). *Proc. 14th Internat. Cong. Electron Microsc.* **3**, 521–522.
- Janecek, M., Louchet, F., Doisneau-Cottignies, B. and Brechet, Y. (2000). *Philos. Mag. A* **80**, 1605–1619.
- Jencic, I., Bench, M.W., Robertson, I.M. and Kirk, M.A. (1995). *J. App. Phys.* **78**, 974–982.
- Jiang, B., Tadakit, T., Mori, H. and Hsu, T.Y. (1997). *Mat. Trans., JIM* **38**, 1072–1077 and 1078–1082.
- Jiang, J.C. and Pan, X.Q. (2000). *Philos. Mag. Lett.* **80**, 271–279.
- Jin, M., Minor, A.M., Stach, E.A. and Morris, J.W., Jr. (2004). *Acta Mat.* **52**, 5381–5387.
- Jin, C.H., Wang, J.Y., Wang, M.S., Su, J. and Peng, L.M. (2005). *Carbon* **43**, 1026–1031.

- Johnson, E., Johansen, A., Nelson, C. and Dahmen, U. (2002). *J. Electron Microsc.* **51** (Supplement), S201–209.
- Johnson, E., Levinsen, M.T., Steenstrup, S., Prokofjev, S., Zhilin, V., Dahmen, U. and Radetic, T. (2004). *Philos. Mag.* **84**, 2663–2673.
- Johnson, K.D. and Dravid, V.P. (1999). *Microsc. Microanal.* **5**, 428–436.
- Johnson, K.D. and Dravid, V.P. (2000). *Interface Sci.* **8**, 189–198.
- Johnston, A.B., Chapman, J.N., Khamsehpour, B. and Wilkinson, C.D.W. (1996). *J. Phys. D* **29**, 1419–1427.
- Kaiser, M., van Pieterson, L. and Verheijen, M.A. (2004). *J. App. Phys.* **96**, 3193–3198.
- Kamino, T., Yaguchi, T., Ukiama, M., Yasutomi, Y. and Saka, H. (1995). *Mat. Transac. JIM* **36**, 73–75.
- Kamino, T., Sasaki, K. and Saka, H. (1997a). *Microsc. Microanal.* **3**, 393–408.
- Kamino, T., Yaguchi, T., Tomita, M. and Saka, H. (1997b). *Philos. Mag. A* **75**, 105–114.
- Kammler, M., Hull, R., Reuter, M.C. and Ross, F.M. (2003). *App. Phys. Lett.* **82**, 1093–1095.
- Kammler, M., Chidambarrao, D., Schwarz, K.W., Black, C.T. and Ross, F.M. (2005). *App. Phys. Lett.* **87**, 133116.
- Kaouache, B., Gergaud, P., Thomas, O., Bostrom, O. and Legros, M. (2003). *Microelectr. Eng.* **70**, 447–454.
- Kassner, M.E., Wall, M.A. and Delos-Reyes, M.A. (1997). *Metallurg. Mat. Transac. A* **28**, 595–609.
- Kato, T., Nunome, K., Morimoto, Y., Nishimura, K. and Saka, H. (2000). *Philos. Mag. Lett.* **80**, 187–192.
- Keller, R.-M., Sigle, W., Baker, S.P., Kraft, O. and Arzt, E. (1997). *Mat. Res. Soc. Symp. Proc.* **436**, 221–226.
- Keller-Flaig, R.-M., Legros, M., Sigle, W., Gouldstone, A., Hemker, K.J., Suresh, S. and Arzt, E. (1999). *J. Mat. Res.* **14**, 4673–4676.
- King, W.E., Merkle, K.L. and Meshii, M. (1981). *Phys. Rev. B* **23**, 6319–6334.
- Kiritani, M. (1999). *Radiat. Eff. Def. Sol.* **148**, 233–267.
- Kirk, K. J., Chapman, J.N., McVitie, S., Aitchison, P.R. and Wilkinson, C.D.W. (1999a). *App. Phys. Lett.* **75**, 3683–3685.
- Kirk, M.A., Jenkins, M.L. and Fukushima, H. (1999b). *Mat. Res. Soc. Sympo. Proc.* **540**, 521–526.
- Kizuka, T. (1998a). *Phys. Rev. Lett.* **81**, 4448–4451.
- Kizuka, T. (1998b). *Phys. Rev. B* **57**, 11158–11163.
- Kizuka, T. and Hosoki, K. (1999). *App. Phys. Lett.* **75**, 2743–2745.
- Kizuka, T. and Tanaka, N. (1997a). *Phys. Rev. B* **56**, R10079–10082.
- Kizuka, T. and Tanaka, N. (1997b). *Philos. Mag. Lett.* **76**, 289–297.
- Kizuka, T., Uhmebara, S. and Fujisawa, S. (2001a). *J. J. App. Phys.*, Part 2 **40**, L71–74.
- Kizuka, T., Ohmi, H., Sumi, T., Kumazawa, K., Deguchi, S., Naruse, M., Fujisawa, S., Sasaki, S., Yabe, A. and Enomoto, Y. (2001b). *J. J. App. Phys.* **40**, L170–L173.
- Kizuka, T., Tanaka, N., Deguchi, S. and Naruse, M. (1998c). *Microsc. Microanal.* **4**, 218–225.
- Kleinschmit, M.W., Yeadon, M. and Gibson, J.M. (1999). *App. Phys. Lett.* **75**, 3288–3290.
- Klie, R.F. and Browning, N. (2001). *J. Electron Microsc.* **50** (Supplement), S59.
- Kociak, M., Suenaga, K., Hirahara, K., Saito, Y., Nakahira, T. and Iijima, S. (2002). *Phys. Rev. Lett.* **89**, 155501.
- Koizumi, H., Oshima, Y., Kondo, Y. and Takayanagi, K. (2001). *Ultramicroscopy* **88**, 17–24.

- Kolar, H.R., Spence, J.C.H. and Alexander, H. (1996). *Phys. Rev. Lett.* **77**, 4031–4034.
- Komatsu, M., Mori, H. and Iwasaki, K. (1994). *J. Amer. Ceramic Soc.* **77**, 839–842.
- Komatsu, M., Matsukawa, Y., Yasunaga, K. and Kiritani, M. (2003). *Mat. Sci. Eng. A* **350**, 25–29.
- Kondo, Y. and Takayanagi, K. (2000). *Science* **289**, 606–608.
- Konno, T.J. and Sinclair, R. (1992). *Philos. Mag. B* **66**, 749–765.
- Konno, T.J. and Sinclair, R. (1995a). *Philos. Mag. B* **71**, 179–199.
- Konno, T.J. and Sinclair, R. (1995b). *Philos. Mag. B* **71**, 163–178.
- Konno, T.J. and Sinclair, R. (1995c). *Acta Met. Mat.* **43**, 471–484.
- Kooi, B.J. and De Hosson, J.T.M. (2001). *Mat. Res. Soc. Symp. Proc.* **654**, AA4.1.1–12.
- Kooi, B.J. and De Hosson, J.T.M. (2004). *J. App. Phys.* **95**, 4714–4721.
- Kooi, B.J., Groot, W.M.G. and De Hosson, J.T.M. (2004). *J. App. Phys.* **95**, 924–932.
- Krishnamurthy, M., Drucker, J.S. and Venables, J.A. (1991). *Mat. Res. Soc. Symp. Proc.* **202**, 77–82.
- Krishnan, A., Dujardin, E., Ebbesen, T.W., Yianilos, P.N. and Treacy, M.M.J. (1998). *Phys. Rev. B* **58**, 14013–14019.
- Krishnan, A., Bisher, M.E. and Treacy, M.M.J. (1999). *Mat. Res. Soc. Symp. Proc.* **541**, 475–480.
- Krishnan, A., Treacy, M.M.J., Bisher, M.E., Chandra, P. and Littlewood, P.B. (2000). *Ameri. Inst. Phys. Conf. Proc.* **535**, 191–200.
- Krishnan, A., Treacy, M.M.J., Bisher, M.E., Chandra, P. and Littlewood, P.B. (2002). *Integ. Ferroelectrics* **43**, 31–49.
- Kruml, T., Caillard, D., Dupas, C. and Martin, J.-L. (2002). *J. Phys. Cond. Matt.* **14**, 12897–12902.
- Kuninori, T., Sukedai, E. and Hashimoto, H. (1996). *Mat. Trans., JIM* **37**, 1404–1407.
- Kuzumaki, T., Sawada, H., Ichinose, H., Horike, Y. and Kizuka, T. (2001). *App. Phys. Lett.* **79**, 4580–4582.
- Kuzumaki, T., Horike, Y., Kizuka, T., Kona, T., Oshima, C. and Mitsuda, Y. (2004). *Diamond Rel. Mat.* **13**, 1907–1913.
- Larsson, M.W., Wallenberg, L.R., Persson, A.I. and Samuelson, L. (2004). *Microsc. Microanal.* **10**, 41–46.
- Latyshev, A.V., Nasimov, D.A., Savenko, V.N. and Aseev, A.L. (2000). *Thin Sol. Films* **367**, 142–148.
- Lau, J.T., Prybyla, J.A. and Theiss, S.K. (2000). *App. Phys. Lett.* **76**, 164–166.
- Lau, J.W., Beleggia, M., Schofield, M.A., Neumark, G.F. and Zhu, Y. J. (2005). *App. Phys.* **97**, 10E702/1–3.
- Lavagne, S., Levade, C. and Vandershaeve, G. (2001). *Proc. Microsc. Semicond. Mat.* **2001**, 219–224.
- Lee, H.-J., Ni, H., Wu, D.T. and Ramirez, A.G. (2005). *App. Phys. Lett.* **87**, 124102.
- Lee, J.G. and Mori, H. (2003). *J. Electron Microsc.* **52**, 57–62.
- Lee, J.G. and Mori, H. (2004a). *Philos. Mag.* **84**, 2675–2686.
- Lee, J.G. and Mori, H. (2004b). *Phys. Rev. Lett.* **93**, 235501/1–4.
- Lee, J.G., Mori, H. and Yasuda, H. (2002a). *Phys. Rev. B* **65**, 132106/1–4.
- Lee, J.G., Taguchi, E. and Mori, H. (2002b). *J. Electron Microsc.* **51** (Suppl), S195–200.
- LeGoues, F.K., Reuter, M.C., Tersoff, J., Hammar, M. and Tromp, R.M. (1994). *Phys. Rev. Lett.* **73**, 300–303.
- LeGoues, F.K., Tersoff, J., Reuter, M.C., Hammar, M. and Tromp, R. (1995). *App. Phys. Lett.* **67**, 2317–2319.

- LeGoues, F.K., Hammar, M., Reuter, M.C. and Tromp, R.M. (1996). *Surface Sci.* **349**, 249–266.
- Legros, M. and Caillard, D. (2001). *J. Microsc.* **203**, 90–98.
- Legros, M., Couret, A. and Caillard, D. (1996). *Philos. Mag.* **73**, 61–80 81–99.
- Legros, M., Minonishi, Y. and Caillard, D. (1997). *Philos. Mag. A* **76**, 995–1011 and 1013–1032.
- Legros, M., Hemker, K.J., Gouldstone, A., Suresh, S., Keller-Flaig, R.M. and Arzt, E. (2002). *Acta Mat.* **50**, 3435–3452.
- Legros, M., Kaouache, B., Gergaud, P., Thomas, O., Dehm, G., Balk, T.J. and Arzt, E. (2005). *Philos. Mag.* **85**, 3541–3552.
- Levade, C., Faress, A. and Vanderschaeve, G. (1994). *Philos. Mag. A* **69**, 855–870.
- Lim, C.K., Chapman, J.N., Rahman, M., Johnston, A.B. and O'Donnell, D.O. (2002). *J. Phys. D* **35**, 2344–2351.
- Lim, C.K., Chapman, J.N., Rahman, M., Johnston, A.B. and O'Donnell, D.O. (2004). *J. App. Phys.* **95**, 1510–1515.
- Lin, X., Murray, C. and Dravid, V.P. (1998). *Proc. Microsc. Microanal.* **1998**, 552.
- Liu, J., Takeguchi, M., Tanaka, M., Yasuda, H. and Furuya, K. (2001). *J. Electron Microsc.* **50**, 541–544.
- Liu, R.-J., Crozier, P.A., Smith, C.M., Hucul, D.A., Blackson, J. and Salaita, G. (2004). *Microsc. Microanal.* **10**, 77–85.
- Liu, X.H., Ross, F.M. and Schwarz, K.W. (2000). *Phys. Rev. Lett.* **85**, 4088–4091.
- Liu, Z., Bando, Y., Mitome, M. and Zhan, J. (2004). *Phys. Rev. Lett.* **93**, 095504/1–4.
- Liu, X.X., Chapman, J.N., McVitie, S. and Wilkinson, C.D.W. (2004). *App. Phys. Lett.* **84**, 4406–4408.
- Lo, W. and Spence, J. (1992). *Ultramicroscopy* **48**, 433.
- Louchet, F., Blandin, J.-J. and Veron, M. (2001). *Adv. Eng. Mat.* **3**, 608–612.
- Lucadamo, G. and Medlin, D.L. (2002). *Acta Mat.* **50**, 3045–3055.
- Ma, X.-G. and Komvopoulos, K. (2005). *J. Mat. Res.* **20**, 1808–1813.
- Maeda, K., Suzuki, K., Yamashita, Y. and Mera, Y. (2000). *J. Phys. Cond. Matt.* **12**, 10079–10091.
- Malaplate, J., Caillard, D. and Couret, A. (2004). *Philos. Mag.* **84**, 3671–3687.
- Marks, L.D. (1983). *Phys. Rev. Lett.* **51**, 1000.
- Marks, L.D., Bengu, E., Collazo-Davila, C., Grozea, D., Landree, E., Leslie, C. and Sinkler, W. (1998). *Surface Rev. Lett.* **5**, 1087–1106.
- Maruno, S., Fujita, S., Watanabe, H., Kusumi, Y. and Ichikawa, M. (1996). *App. Phys. Lett.* **68**, 2213–2215.
- Mathes, D.T., Hull, R., Choquette, K.D., Geib, K.M., Allerman, A.A., Guenter, J.K., Hawkins, B. and Hawthorne, R.A. (2003). *Proc. SPIE* **4994**, 67–82.
- Matsuda, T., Harada, K., Kasai, H., Kamimura, O. and Tonomura, A. (1996). *Science* **271**, 1393–1395.
- Matsuda, T., Kamimura, O., Kasai, H., Harada, K., Yoshida, T., Akashi, T., Tonomura, A., Nakayama, Y., Shimoyama, J., Kishio, K., Hanaguri, T. and Kitazawa, K. (2001). *Science* **294**, 2136–2138.
- Matsumoto, H., Sukedai, E. and Hashimoto, H. (1999). *Mat. Trans. JIM* **40**, 1436–1443.
- Matsunaga, K., Ii, S., Iwamoto, C., Yamamoto, T. and Ikuhara, Y. (2004). *Nano-technology* **15**, S376–S381.
- McKelvy, M.J., Sharma, R., Chizmeshya, A.V.G., Carpenter, R.W. and Streib, K. (2001). *Chem. Mat.* **13**, 921–926.
- McVitie, S. and Chapman, J.N. (1997). *Microsc. Microanal.* **3**, 146–153.

- Medlin, D.L., Campbell, G.H. and Carter, C.R. (1998). *Acta Mat.* **46**, 5135–5142.
- Mera, Y., Suzuki, K. and Maeda, K. (2003). *Phys. B* **340–342**, 488–491.
- Merkle, K.L. and Thompson, L.J. (2001). *Mat. Lett.* **48**, 188–193.
- Merkle, K.L., Thompson, L.J. and Phillip, F. (2002a). *Philos. Mag. Lett.* **82**, 589–597.
- Merkle, K.L., Thompson, L.J. and Phillip, F. (2002b). *Phys. Rev. Lett.* **88**, 225501/1–4.
- Messerschmidt, U. (2001). *J. Microsc.* **203**, 68–71.
- Messerschmidt, U. and Bartsch, M. (2003). *Mat. Chem. Phys.* **81**, 518–523.
- Messerschmidt, U., Baither, D., Baufeld, B. and Bartsch, M. (1997). *Mat. Sci. Eng. A* **233**, 61–74.
- Messerschmidt, U., Baither, D., Bartsch, M., Baufeld, B., Geyer, B., Guder, S., Wasilkowska, A., Czyrska-Filemonowicz, A., Yamaguchi, M., Feuerbacher, M. and Urban, K. (1998). *Microsc. Microanal.* **4**, 226–234.
- Messerschmidt, U., Bartsch, M., Feuerbacher, M., Geyer, B. and Urban, K. (1999). *Philos. Mag. A* **79**, 2123–2135.
- Minoda, H. and Yagi, K. (1996). *J. Crystal Growth* **163**, 48–53.
- Minoda, H. and Yagi, K. (1999). *Surface Sci.* **437**, L761–766.
- Minoda, H., Yagi, K., Meyer zu Heringdorf, F.-J., Meier, A., Kahler, D. and Horn von Hoegen, M. (1999). *Phys. Rev. B* **59**, 2363–2375.
- Minor, A.M., Morris, J.W. and Stach, E.A. (2001). *App. Phys. Lett.* **79**, 1625–1627.
- Minor, A.M., Lilleodden, E.T., Jin, M., Stach, E.A., Chrzan, D.C. and Morris, J.W. (2005). *Philos. Mag.* **85**, S323–S330.
- Missana, T., Afonso, C.N., Petford-Long, A.K. and Doole, R.C. (1999). *Philos. Mag. A* **79**, 2577–2590.
- Mitome, M., Takayanagi, K. and Tanishiro, Y. (1990). *Phys. Rev. B* **42**, 7238–7241.
- Mompiou, F., Caillard, D. and Feuerbacher, M. (2004). *Philos. Mag.* **84**, 2777.
- Mori, H., Yasuda, H., Koyama, H., Sumida, N. and Fujita, H. (1992). *Nucl. Inst. Methods Phys. Res. B* **63**, 291–296.
- Mori, H., Okabayashi, H. and Komatsu, M. (1997). *Thin Sol. Films* **300**, 25–29.
- Mori, H. (1998). *Mat. Trans. JIM* **39**, 959–966.
- Mori, S., Yamamoto, N., Koyama, Y. and Uesu, Y. (1997). *Phys. Rev. B* **55**, 11212–11217.
- Morkved, T.L., Lopes, W.A., Hahm, J., Sibener, S.J. and Jaeger, H.M. (1998). *Polymer* **39**, 3871–3875.
- Murakami, Y. and Shindo, D. (2001). *Philos. Mag. Lett.* **81**, 631–638.
- Murakami, Y., Shindo, D., Oikawa, K., Kainuma, R. and Ishida, K. (2002). *Acta Mat.* **50**, 2173–2184.
- Naitoh, Y., Takayanagi, K., Oshima, Y. and Hirayama, H. (2000). *J. Electron Microsc.* **49**, 211–216.
- Nath, R., Soo, C.W., Boothroyd, C.B., Yeadon, M., Chi, D.Z., Sun, H.P., Chen, Y.B., Pan, X.Q. and Foo, Y.L. (2005). *App. Phys. Lett.* **86**, 201908-1–3.
- Niihara, K., Sekino, T., Nakahira, A., Kamino, T. and Yaguchi, T. (1996). *Mat. Lett.* **27**, 121–124.
- Ning, X.G., Avalos-Borja, M. and Ye, H.Q. (1996). *J. App. Phys.* **79**, 125–128.
- Nishizawa, H., Hori, F. and Oshima, R. (2002). *J. Crystal Growth* **236**, 51–58.
- Nucci, J., Krämer, S., Arzt, E. and Volkert, C.A. (2005). *J. Mat. Res.* **20**, 1851–1859.
- Ohmura, T., Minor, A.M., Stach, E.A. and Morris, J.W., Jr. (2004). *J. Mat. Res.* **19**, 3626–3632.

- Ohnishi, H., Kondo, Y. and Takayanagi, K. (1998a). *Surface Sci.* **415**, L1061–1064.
- Ohnishi, H., Kondo, Y. and Takayanagi, K. (1998b). *Nature* **395**, 780–783.
- Okabayashi, H., Kitamura, H., Komatsu, M. and Mori, H. (1996). *App. Phys. Lett.* **68**, 1066–1068.
- Ono, K., Arakawa, K., Hojou, K., Oohasi, M., Birtcher, R.C. and Donnelly, S.E. (2002). *J. Electron Microsc.* **51** (Supplement), S245–251.
- Oshima, Y., Hirata, T., Yokoyama, T., Hirayama, H. and Takayanagi, K. (2000). *Surface Sci.* **465**, 81–89.
- Oshima, Y., Koizumi, H., Mouri, K., Hirayama, H., Takayanagi, K. and Kondo, Y. (2002). *Phys. Rev. B* **65**, 121401/1–4.
- Oshima, Y., Kondo, Y. and Takayanagi, K. (2003a). *J. Electron Microsc.* **52**, 49–55.
- Oshima, Y., Onga, A. and Takayanagi, K. (2003b). *Phys. Rev. Lett.* **91**, 205503/1–4.
- Oshima, Y., Mouri, K., Hirayama, H. and Takayanagi, K. (2003c). *Surface Sci.* **531**, 209–216.
- Pan, X.-Q., Hu, M.-S., Yao, M.-H. and Feng, D. (1985). *Phys. Stat. Sol. A* **92**, 57–68.
- Park, H.S., Murakami, Y., Shindo, D., Chernenko, V.A. and Kanomata, T. (2003). *App. Phys. Lett.* **83**, 3752–3754.
- Park, H.S., Park, Y.-G., Gao, Y., Shindo, D. and Inoue, M. (2005). *J. App. Phys.* **97**, 33908-1–4.
- Parker, M.A., Sigmon, T.W. and Sinclair, R. (1986). *Mat. Res. Soc. Sympos. Proc.* **62**, 311–322.
- Parker, M.A. and Sinclair, R. (1986). *Nature* **322**, 531–533.
- Persson, A.I., Larsson, M.W., Stenstrom, S., Ohlsson, B.J., Samuelson, L. and Wallenberg, L.R. (2004). *Nat. Mat.* **3**, 677–681.
- Petford-Long, A.K., Doole, R.C., Afonso, C.N. and Solis, J. (1995). *J. App. Phys.* **77**, 607–613.
- Pettinari, F., Couret, A., Caillard, D., Molenat, G., Clement, N. and Coujou, A. (2001). *J. Microsc.* **203**, 47–56.
- Poncharal, P., Frank, S., Wang, Z.L. and de Heer, W.A. (1999). *Eur. Phys. J. D* **9**, 77–79.
- Poncharal, P., Berger, C., Yan Yi, Wang, Z.L. and de Heer, W.A. (2002). *J. Phys. Chem. B* **106**, 12104–12118.
- Poppa, H. (1965). *J. Vac. Sci. Tech.* **2**, 42–48.
- Poppa, H. (2004). *J. Vac. Sci. Tech. A* **22**, 1931–1947.
- Portavoce, A., Kammler, M., Hull, R., Reuter, M.C., Copel, M. and Ross, F.M. (2004). *Phys. Rev. B* **70**, 195306-1–9.
- Portavoce, A., Hull, R. and Ross, F.M. (2006). In *Lateral Alignment of Epitaxial Quantum Dots* (O. Schmidt, Ed.). Springer, New York.
- Portier, X. and Petford-Long, A.K. (2000). *App. Phys. Lett.* **76**, 754–756.
- Portier, X., Petford-Long, A.K., Doole, R.C., Anthony, T.C. and Brug, J.A. (1997). *App. Phys. Lett.* **71**, 2032–2034.
- Portier, X., Tsymbal, E. Yu., Petford-Long, A.K., Anthony, T.C. and Brug, J.A. (1998). *Phys. Rev. B* **58**, R591–594.
- Portier, X., Petford-Long, A.K., Anthony, T.C. and Brug, J.A. (1999a). *App. Phys. Lett.* **75**, 1290–1292.
- Portier, X., Petford-Long, A.K., Anthony, T.C. and Brug, J.A. (1999b). *J. App. Phys.* **85**, 4120–4126.
- Prybyla, J.A., Riege, S.P., Grabowski, S.P. and Hunt, A.W. (1998). *App. Phys. Lett.* **73**, 1083–1085.
- Pyo, S.G. and Kim, N.J. (2005). *J. Mat. Res.* **20**, 1888–1901.
- Radisic, A. (2004). Ph.D. Thesis, The Johns Hopkins University.

- Radisic, A., Vereecken, P.M., Hannon, J.B., Searson, P.C. and Ross, F.M. (2006). *Nano Lett.* **6**, 238–242.
- Ren, S.B., Lu, C.J., Shen, H.M. and Wang, Y.N. (1994). *Mat. Res. Soc. Symp. Proc.* **404**, 95–100.
- Riege, S.P., Prybyla, J.A. and Hunt, A.W. (1996). *App. Phys. Lett.* **69**, 2367–2369.
- Robertson, I.M. and Teter, D. (1998). *Microsc. Res. Tech.* **42**, 260–269.
- Roddatis, V.V., Kuznetsov, V.L., Butenko, Yu, V., Su, D.S. and Schlogl, R. (2002). *Phys. Chem. Chem. Phys.* **4**, 1964–1967.
- Ross, F.M. (2000). *IBM J. Res. Dev.* **44**, 489–501.
- Ross, F.M. and Gibson, J.M. (1991). *Phys. Rev. Lett.* **68**, 1782–1785.
- Ross, F.M., Hull, R., Bahnck, D., Bean, J.C., Peticolas, L.J. and King, C.A. (1993). *App. Phys. Lett.* **62**, 1426–1428.
- Ross, F.M., Kola, R.R., Hull, R. and Bean, J.C. (1994a). *Mat. Res. Soc. Symp. Proc.* **318**, 697–702.
- Ross, F.M., Gibson, J.M. and Tweten, R.D. (1994b). *Surface Sci.* **310**, 243–266.
- Ross, F.M., Tersoff, J. and Tromp, R.M. (1998). *Phys. Rev. Lett.* **80**, 984–987.
- Ross, F.M., Bennett, P.A., Tromp, R.M., Tersoff, J. and Reuter, M. (1999a). *Micron* **30**, 21–32.
- Ross, F.M., Tromp, R.M. and Reuter, M.C. (1999b). *Science* **286**, 1931–1934.
- Ross, F.M., Kammler, M., Walsh, M.E. and Reuter, M.C. (2004). *Microsc. Microanal.* **10**, 105–111.
- Ross, F.M., Tersoff, J., Kodambaka, S. and Reuter, M.C. (2006). *Springer Proceedings in Physics* **107**, 283–286.
- Ross, F.M., Tersoff, J. and Reuter, M.C. (2005). *Phys. Rev. Lett.* **95**, 146104/1–4.
- Ru, Q., Okamoto, M., Kondo, Y. and Takayanagi, K. (1996). *Chem. Phys. Lett.* **259**, 425–431.
- Ruault, M.O., Fortuna, F., Bernas, H., Chaumont, J., Kaitasov, O. and Borodin, V.A. (2005). *J. Mat. Res.* **20**, 1758–1768.
- Ruault, M.O., Fortuna, F., Bernas, H., Ridgway, M.C. and Williams, J.S. (2002). *App. Phys. Lett.* **81**, 2617–2619.
- Saka, H., Arai, S., Tsukimoto, S. and Sasaki, K. (1999). *Mat. Sci. Forum* **294–296**, 617–620.
- Sasaki, K. and Saka, H. (1997). *Mat. Res. Soc. Symp. Proc.* **466**, 185–190.
- Sayagues, M.J. and Hutchison, J.L. (1996). *J. Sol. State Chem.* **124**, 116–122.
- Sayagues, M.J. and Hutchison, J.L. (2002). *J. Sol. State Chem.* **163**, 137–143.
- Schaper, A.K., Phillip, F. and Hou, H. (2005). *J. Mat. Res.* **20**, 1844–1850.
- Schneider, A., Hoffmann, H. and Zweck, J. (2003). *J. Magn. Magn. Mat.* **257**, 1–10.
- Schneider, M., Hoffmann, H. and Zweck, J. (2001). *App. Phys. Lett.* **79**, 3113–3115.
- Schneider, M., Hoffmann, H., Otto, S., Haug, Th. and Zweck, J. (2002). *J. App. Phys.* **92**, 1466–1472.
- Schryvers, D. and Ma, Y. (1995). *Mat. Lett.* **23**, 105–111.
- Schryvers, D., Lahjouji, D.E., Slootmaekers, B. and Potapov, P.L. (1996). *Scripta Mat.* **35**, 1235–1241.
- Schryvers, D., Yandouzi, M. and Toth, L. (1998). *Thin Sol. Films* **326**, 126–133.
- Senda, Y., Sasaki, K. and Saka, H. (2004). *Philos. Mag.* **84**, 2635–2649.
- Shah, J. (2004). *Philos. Mag.* **84**, 2749–2765.
- Shan, Z., Stach, E.A., Wiesorek, J.M.K., Knapp, J.A., Forstaedt, D.M. and Mao, S.X. (2004). *Science* **305**, 654–657.
- Sharma, R. (2001). *Microsc. Microanal.* **7**, 494–506.

- Sharma, R. (2005). *J. Mat. Res.* **20**, 1695–1707.
- Sharma, R. and Iqbal, Z. (2004). *App. Phys. Lett.* **84**, 990–992.
- Sharma, R., Crozier, P.A., Kang, Z.C. and Eyring, L. (2004). *Philos. Mag.* **84**, 2731–2747.
- Sharma, R., McKelvy, M.J., Bearat, H., Chizmeshya, A.V.G. and Carpenter, R. W. (2004b). *Philos. Mag.* **84**, 2711–2729.
- Sharma, R., Naedele, D. and Schweda, E. (2001). *Chem. Mat.* **13**, 4014–4018.
- Sharma, R., Rez, P., Treacy, M.M.J. and Stuart, J. (2005). *J. Electron Microsc.* **54**, 231–237.
- Shih, W.C. and Green, A.L. (1995). *Mat. Res. Soc. Sympo. Proc.* **356**, 417.
- Shimojo, M., Mitsuishi, K., Tanaka, M., Han, M. and Furuya, K. (2004). *J. Microsc.* **214**, 76–79.
- Sidorov, M.V., Kardynal, B. and Smith, D.J. (1998a). *Microsc. Microanal.* **4**, 317–324.
- Sidorov, M.V., McKelvy, M.J., Sharma, R. and Glaunsinger, W.S. (1998b). *J. Sol. State Chem.* **141**, 330–337.
- Sinclair, R. (1994). *Mat. Res. Soc. Bull.* **19**(6), 26–31.
- Sinclair, R., Parker, M.A. and Kim, K.B. (1987). *Ultramicroscopy* **23**, 383–395.
- Sinclair, R., Yamashita, T., Parker, M.A., Kim, K.B., Holloway, K. and Schwartzman, A.F. (1988). *Acta Cryst. A* **44**, 965–975.
- Sinclair, R., Itoh, T. and Chin, R. (2002). *Microsc. Microanal.* **8**, 288–304.
- Smeeton, T.M., Kappers, M.J., Barnard, J.S., Vickers, M.E. and Humphreys, C. J. (2003). *App. Phys. Lett.* **83**, 5419–5421.
- Smith, D.J., Petford-Long, A.K., Wallenberg, L.R. and Bovin, J.-O. (1986). *Science* **233**, 872–875.
- Smith, D.J., Gajdardziska-Josifovska, M., Lu, P., McCartney, M.R., Podbrdsky, J., Swann, P.R. and Jones, J.S. (1993). *Ultramicroscopy* **49**, 26–36.
- Snoeck, E. and Roucau, C. (1992). *Phys. Rev. B* **45**, 12720–12724.
- Snoeck, E., Normand, L., Thorel, A. and Roucau, C. (1994). *Phase Trans. A* **46**, 77–88.
- Soer, W.A., De Hosson, J.T.M., Minor, A.M., Morris, J.W., Jr. and Stach, E.A. (2004). *Acta Mat.* **52**, 5783–5790.
- Sofronis, P. and Robertson, I.M. (2002). *Philos. Mag. A* **82**, 3405–3413.
- Song, M., Mitsuishi, K., Yasuda, H. and Furuya, K. (2002). *J. Electron Microsc.* **51** (Supplement), S211–214.
- Sow, C.-H., Harada, K., Tonomura, A., Crabtree, G. and Grier, D.G. (1998). *Phys. Rev. Lett.* **80**, 2693–2696.
- Spence, J.C.H., Lo, W. and Kuwabara, M. (1990). *Ultramicroscopy* **33**, 69–82.
- Spence, J.C.H., Kolar, H.R., Hembree, H.R., Humphreys, C.J., Barnard, J., Datta, R., Koch, C., Ross, F.M. and Justo, J.F. (2006). *Philosophical Magazine*, in press.
- Stach, E.A., Hull, R., Bean, J.C., Jones, K.S. and Nejim, A. (1998a). *Microsc. Microanal.* **4**, 294–307.
- Stach, E.A., Hull, R., Tromp, R.M., Reuter, M.C., Copel, M., LeGoues, F.K. and Bean, J.C. (1998b). *J. App. Phys.* **83**, 1931–1937.
- Stach, E.A., Hull, R., Tromp, R.M., Ross, F.M., Reuter, M.C. and Bean, J.C. (2000). *Philos. Mag. A* **80**, 2159–2200.
- Stach, E.A., Freeman, T., Minor, A.M., Owen, D.K., Cumings, J., Wall, M.A., Chraska, T., Hull, R., Morris, Jr., J.W., Zettl, A. and Dahmen, U. (2001). *Microsc. Microanal.* **7**, 507–517.
- Stach, E.A., Pauzauskie, P.J., Kuykendall, T., Goldberger, J., He, R. and Yang, P. (2003). *Nano Lett.* **3**, 867.
- Storaska, G.A. and Howe, J.M. (2004). *Mat. Sci. Eng. A* **368**, 183–190.
- Storaska, G.A., Moore, K.T. and Howe, J.M. (2004). *Philos. Mag.* **84**, 2619–2634.

- Suenaga, K., Colliex, C. and Iijima, S. (2001). *App. Phys. Lett.* **78**, 70–72.
- Sugi, H., Akimoto, T., Sutoh, K., Chaen, S., Oishi, N. and Suzuki, S. (1997). *Proc. Nat. Acad. Sci. USA* **94**, 4378–4382.
- Suh, Y.J., Prikhodko, S.V. and Friedlander, A.K. (2004). *Microsc. Microanal.* **8**, 497.
- Sun, H.P., Pan, X.Q., Haeni, J.H. and Schlom, D.G. (2004). *App. Phys. Lett.* **85**, 1967–1969.
- Sun, H.P., Chen, Y.B., Pan, X.Q., Chi, D.Z., Nath, R. and Foo, Y.L. (2005a). *App. Phys. Lett.* **86**, 71904-1–3.
- Sun, K., Wang, L.M., Ewing, R.C. and Weber, W.J. (2005b). *Philos. Mag.* **85**, 597–608.
- Takayanagi, K., Tanishiro, Y., Takahashi, S. and Takahashi, M. (1985). *Surface Sci.* **164**, 367–392.
- Takeda, S. and Yamasaki, J. (1999). *Phys. Rev. Lett.* **83**, 320–323.
- Takeguchi, M., Shimojo, M. and Furuya, K. (2005). *Nanotechnology* **16**, 1321–1325.
- Tamiya, T., Shindo, D., Murakami, Y., Bando, Y. and Otsuka, K. (1998). *Mat. Trans. JIM* **39**, 714–723.
- Tan, X., Xu, Z., Shang, J.K. and Han, P. (2000). *App. Phys. Lett.* **77**, 1529–1531.
- Tan, X., Du, T. and Shang, J.K. (2002). *App. Phys. Lett.* **80**, 3946–3948.
- Tan, X. and Shang, J.K. (2004a). *J. App. Phys.* **95**, 2805–2810.
- Tan, X. and Shang, J.K. (2004b). *J. App. Phys.* **96**, 635–639.
- Tan, X.L., He, H. and Shang, J.K. (2005). *J. Mat. Res.* **20**, 1641–1653.
- Tanaka, H., Konno, T.J., Sinclair, R. and Hirashita, N. (1995). *J. App. Phys.* **78**, 4982–4987.
- Tanaka, H., Hirashita, N. and Sinclair, R. (1996). *Jap. J. Appl. Phys. Part 2 (Letters)* **35**, L479–481.
- Tanaka, H., Hirashita, N. and Sinclair, R. (1998a). *Jap. J. Appl. Phys. Part 1*, **37**, 4284–4287.
- Tanaka, N., Kimata, H., Takashima, T. and Kizuka, T. (1998b). *Surface Rev. Lett.* **5**, 723–729.
- Tanaka, M., Furuya, K. and Saito, T. (1998c). *Microsc. Microanal.* **4**, 207–217.
- Tanaka, M., Han, M., Takeguchi, M. and Furuya, K. (2004). *Philos. Mag.* **84**, 2699–2709.
- Tanaka, M., Chu, F., Shimojo, M., Takeguchi, M., Mitsuishi, K. and Furuya, K. (2005). *App. Phys. Lett.* **86**, 183104.
- Tanner, L.E., Pelton, A.R., Van Tendeloo, G., Schryvers, D. and Wall, M.E. (1990). *Scripta Met. Mat.* **24**, 1731–1736.
- Tappin, D.K., Robertson, I.M. and Birnbaum, H.K. (1995). *Phys. Rev. B* **51**, 14854–14860.
- Teodorescu, V., Nistor, L., Bender, H., Steegen, A., Lauwers, A., Maex, K. and Van Landuyt, J. (2001). *J. App. Phys.* **90**, 167–174.
- Terrones, M., Terrones, H., Banhart, F., Charlier, J.-C. and Ajayan, P.M. (2000). *Sci.* **288**, 1226–1229.
- Terrones, M., Banhart, F., Grobert, N., Charlier, J.-C., Terrones, H. and Ajayan, P.M. (2002). *Phys. Rev. Lett.* **89**, 075505/1–4.
- Teter, D.F., Robertson, I.M. and Birnbaum, H.K. (2001). *Acta Mat.* **49**, 4313–4323.
- Thilly, L., Veron, M., Ludwig, O., Lecouturier, F., Peyrade, J.P. and Askenazy, S. (2002). *Philos. Mag. A* **82**, 925–942.
- Thompson, P., Guttfleisch, O., Chapman, J.N. and Harris, I.R. (1997). *J. Phys. D* **30**, 1854–1860.
- Togawa, Y., Harada, K., Akashi, T., Kasai, H., Matsuda, T., Nori, F., Maeda, A. and Tonomura, A. (2005). *Phys. Rev. Lett.* **95**, 87002.
- Tonomura, A. (2002). *J. Electron Microsc.* **51** (supplement), S3–S11.

- Tonomura, A. (2003). *J. Electron Microscop.* **52**, 11–19.
- Tonomura, A., Kasai, H., Kamimura, O., Matsuda, T., Harada, K., Nakayama, Y., Shimoyama, J., Kishio, K., Hanaguri, T., Kitazawa, K., Sasase, M. and Okayasu, S. (2001). *Nature* **412**, 620–622.
- Tonomura, A., Kasai, H., Kamimura, O., Matsuda, T., Harada, K., Yoshida, T., Akashi, T., Shimoyama, J., Kishio, K., Hanaguri, T., Kitazawa, K., Masui, T., Tajima, S., Koshizuka, N., Gammel, P.L., Bishop, D., Sasase, M. and Okayasu, S. (2002). *Phys. Rev. Lett.* **88**, 237001/1–4.
- Toporov, A. Yu., Langford, R.M. and Petford-Long, A.K. (2000). *App. Phys. Lett.* **77**, 3063–3065.
- Troiani, H.E., Camacho-Bragado, A., Armendariz, V., Gardea Torresday, J.L. and Yacaman, M.J. (2003). *Chem. Mat.* **15**, 1029–1031.
- Twitchett, A.C., Dunin-Borkowski, R.E. and Midgley, P.A. (2002). *Phys. Rev. Lett.* **88**, 238302/1–4.
- Twitchett, A.C., Dunin-Borkowski, R.E., Broom, R.F. and Midgley, P.A. (2004). *J. Phys. Cond. Matt.* **16**, S181–192.
- Ugarte, D. (1992). *Nature* **359**, 707–709.
- Uhlig, T., Heumann, M. and Zweck, J. (2003). *Ultramicroscopy* **94**, 193–196.
- Uruta, K., Sato, Y., Suenaga, K., Gloter, A., Hashimoto, A., Ishida, M., Shimada, T., Shinohara, H. and Iijima, S. (2004). *Nano Lett.* **4**, 2451–2454.
- Uruta, K., Suenaga, K., Sugai, T., Shinohara, H. and Iijima, S. (2005). *Phys. Rev. Lett.* **94**, 155502.
- Vanderschaeve, G., Levade, C. and Caillard, D. (2000). *J. Phys. Cond. Matt.* **12**, 10093–10103.
- Vanderschaeve, G., Levade, C. and Caillard, D. (2001). *J. Microsc.* **203**, 72–83.
- Vanhellemont, J., Romano-Rodriguez, A., Fedina, L., Van Landuyt, J. and Aseev, A. (1995). *Mat. Sci. Tech.* **11**, 1194–1202.
- Venables, J. (1981). *Ultramicroscopy* **7**, 81–98.
- Verhaeghe, B., Louchet, F., Doisneau-Cottignies, B., Brechet, Y. and Massoud, J.-P. (1997). *Philos. Mag. A* **76**, 1079–1091.
- Verheijen, M.A., Donkers, J.J.T.M., Thomassen, J.F.P., van den Broek, J.J., van der Rijt, R.A.F., Dona, M.J.J. and Smit, C.M. (2004). *Rev. Sci. Inst.* **75**, 426–429.
- Verwerft, M., Van Tendeloo, G., Van Landuyt, J. and Amelinckx, S. (1988). *Ferroelectrics* **88**, 27–36.
- Vetrano, J.S., Bruemmer, S.M. and Robertson, I.M. (1995). *Mat. Res. Soc. Symp. Proc.* **404**, 177–182.
- Vetrano, J.S., Bruemmer, S.M., Pawlowski, L.M. and Robertson, I.M. (1997). *Mat. Sci. Eng. A* **238**, 101–107.
- Volkov, V.V. and Zhu, Y. (2000). *J. Magn. Magn. Mat.* **214**, 204–216.
- Volkov, V.V., Zhu, Y. and Malac, M. (2004). *Philos. Mag.* **84**, 2607–2617.
- Vook, R.W. (1994). *Mat. Chem. Phys.* **36**, 199–216.
- Vystavel, T., Palasantzas, G., Koch, S.A. and De Hosson, J.T.M. (2003a). *App. Phys. Lett.* **82**, 197–199.
- Vystavel, T., Palasantzas, G., Koch, S.A. and De Hosson, J.T.M. (2003b). *App. Phys. Lett.* **83**, 3909–3911.
- Wall, M.A. and Barbee, T.W., Jr. (1997). *Mat. Res. Soc. Symp. Proc.* **480**, 245–250.
- Wall, M.A. and Dahmen, U. (1998). *Microsc. Res. Tech.* **42**, 248–254.
- Wall, M.A., Barbee, T.W. and Weihs, T.P. (1995). *Mat. Res. Soc. Symp. Proc.* **404**, 43–48.
- Walsh, C.A. (1989). *Philos. Mag. A* **59**, 227–246.
- Wang, M.H. and Chen, L.J. (1992). *J. App. Phys.* **71**, 5918–5925.
- Wang, Y.G. and Petford-Long, A.K. (2002). *J. App. Phys.* **92**, 6699–6707.

- Wang, Z.L., Gao, R.P., Pan, Z.W. and Dai, Z.R. (2001). *Adv. Eng. Mat.* **3**, 657–661.
- Wang, Z.L., Dai, Z.R., Gao, R. and Gole, J.L. (2002a). *J. Electron Microsc.* **51** (Supplement), S79–85.
- Wang, Z.L., Gao, R.P., de Heer, W.A. and Poncharal, P. (2002b). *App. Phys. Lett.* **80**, 856–858.
- Wang, L. and Yang, J.C. (2005). *J. Mat. Res.* **20**, 1902–1909.
- Wang, M.S., Wang, J.Y., Chen, Q. and Peng, L.M. (2005). *Adv. Funct. Mat.* **15**, 1825–1831.
- Watanabe, S., Haishi, Y., Suda, T., Ohnuki, S., Takahashi, H. and Kiritani, M. (2002). *Radia. Eff. Def. Sol.* **157**, 101–108.
- Werner, M., Weber, E.R., Bartsch, M. and Messerschmidt, U. (1995). *Phys. Stat. Sol. A* **150**, 337–341.
- Williamson, M.J., Tromp, R.M., Vereecken, P.M., Hull, R. and Ross, F.M. (2003). *Nature Mat.* **2**, 532–536.
- Wise, M.E., Biskos, G., Martin, S.T., Russell, L.M. and Buseck, P.R. (2005). *Aerosol Sci. Tech. B*, 849–856.
- Wu, Y. and Yang, P. (2001). *J. Amer. Chem. Soc.* **123**, 3165.
- Xu, H.P., Li, Q., Feng, D., Shen, G.J., Guan, Q.C. and Wang, J.Y. (1993). *Ferroelectrics* **146**, 137–144.
- Xu, Z., Tan, X., Han, P. and Shang, J.K. (2000). *App. Phys. Lett.* **76**, 3732–3734.
- Xu, Z., Bai, X.D., Wang, E.G. and Wang, Z.L. (2005b). *App. Phys. Lett.* **87**, 163106.
- Xu, Z., Bai, X.D., Wang, E.G. and Wang, Z.L. (2005a). *J. Phys.—Cond. Matter.* **17**, L507–L512.
- Yamashita, J., Hirayama, H., Ohshima, Y. and Takayanagi, K. (1999). *App. Phys. Lett.* **74**, 2450–2452.
- Yang, J.C., Kolasa, A.B., Gibson, J.M. and Yeadon, M. (1998). *App. Phys. Lett.* **73**, 2841–2843.
- Yang, J.C., Evan, D. and Tropia, L. (2002). *App. Phys. Lett.* **81**, 241–243.
- Yasuda, H. and Mori, H. (1999). *J. Electron Microsc.* **48**, 581–584.
- Yasuda, H., Mori, H., Sakata, T., Naka, M. and Fujita, H. (1992). *Philos. Mag. B* **65**, 1001–1009.
- Yasuda, H., Mori, H. and Furuya, K. (2000). *Philos. Mag. Lett.* **80**, 181–186.
- Yasuda, H., Mitsuishi, K. and Mori, H. (2001). *Phys. Rev. B* **64**, 094101/1–6.
- Yasuda, H., Mori, H. and Lee, J.G. (2004). *Phys. Rev. B* **70**, 214105/1–6.
- Yeadon, M., Yang, J.C., Averback, R.S., Bullard, J.W., Olynick, D.L. and Gibson, J.M. (1997). *App. Phys. Lett.* **71**, 1631–1633.
- Yi, G., Nicholson, W.A.P., Lim, C.K., Chapman, J.N., McVitie, S. and Wilkinson, C.D.W. (2004). *Ultramicroscopy* **99**, 65–72.
- Yokota, T., Howe, J.M., Jesser, W.A. and Murayama, M. (2004). *J. App. Phys.* **95**, 5756–5761.
- Yonenaga, I., Brown, P.D. and Humphreys, C.J. (1998). *Mat. Sci. Eng. A* **253**, 148–150.
- Yonenaga, I., Werner, M., Bartsch, M., Messerschmidt, U. and Weber, E.R. (1999). *Phys. Stat. Sol. A* **171**, 35–40.
- Yoo, J.H., Murakami, Y., Shindo, D. and Ohsuna, T. (2004a). *Philos. Mag.* **84**, 2597–2606.
- Yoo, J.H., Murakami, Y., Shindo, D., Atou, T. and Kikuchi, M. (2004b). *Phys. Rev. Lett.* **93**, 047204/1–4.
- Yoshida, K., Yamasaki, J. and Tanaka, N. (2004). *App. Phys. Lett.* **84**, 2542–2544.
- Yu, A.C.C., Lo, C.C.H., Petford-Long, A.K., Jiles, D.C. and Miyazaki, T. (2002a). *J. App. Phys.* **91**, 780–784.

- Yu, A.C.C., Petford-Long, A.K., O'Grady, K. and Miyazaki, T. (2002b). *J. App. Phys.* **91**, 5234–5239.
- Zerrouk, T.E.A., Hamichi, M., Pilkington, J.D.H. and Venables, J.A. (1994). *Phys. Rev. B* **50**, 8946–8949.
- Zghal, S., Coujou, A. and Couret, A. (2001). *Philos. Mag. A* **81**, 345.
- Zhang, L.H., Johnson, E. and Dahmen, U. (2004). *Mat. Res. Soc. Symp. Proc.* **821**, 181–186.
- Zhang, M., Olson, E.A., Twesten, R.D., Wen, J.G., Allen, L.H., Robertson, I.M. and Petrov, I. (2005). *J. Mat. Res.* **20**, 1802–1807.
- Zhou, G. and Yang, J.C. (2002). *Phys. Rev. Lett.* **89**, 106101/1–4.
- Zhou, G. and Yang, J.C. (2003). *Surface Sci.* **531**, 359–367.
- Zhou, G., Yang, J.C., Xu, F., Barnard, J.A. and Zhang, Z. (2002). *Mat. Res. Soc. Symp. Proc.* **737**, F6.3.
- Zhu, Y. and De Graef, M., Eds. (2001). *Magnetic Imaging and Its Applications to Materials*. (Academic Press, San Diego).
- Zielinski, W., Swiatnicki, W., Barstch, M. and Messerschmidt, U. (2003). *Mat. Chem. Phys.* **81**, 476–479.
- Zimmermann, C.G., Yeadon, M., Nordlund, K., Gibson, J.M., Averback, R.S., Herr, U. and Samwer, K. (1999). *Phys. Rev. Lett.* **83**, 1163–1166.